ACTA MATERIALIA TRANSYLVANICA

Material Sciences Publications

Volume 8, Issue 2

ERDÉLYI MÚZEUM-EGYESÜLET
Kolozsvár
2025

A folyóirat megjelenését támogatta a Communitas Alapítvány, a Magyar Tudományos Akadémia, a Bethlen Gábor Alapkezelő Zrt. és az EME Műszaki Tudományok Szakosztálya / The publication of this magazine was supported by the Communitas Foundation, by the Hungarian Academy of Sciences, by the Bethlen Gábor Fund and by the EME – Department of Engineering Sciences.

Kiadó / Publisher: Erdélyi Múzeum-Egyesület
Felelős kiadó / Responsible publisher: Biró Annamária
Olvasószerkesztő / Proofreader: Szenkovics Enikő (magyar), David Speight (English)
Borítóterv / Cover: Könczey Elemér
Nyomdai munkálatok / Printed at: F&F International Kft., Gyergyószentmiklós

ISSN 2601-1883, ISSN-L 2601-1883
DOI: 10.33923/amt-2025-02
A folyóirat honlapja: https://www.eme.ro/publication-hu/acta-mat/mat-main.htm
The journal website: https://www.eme.ro/publication/acta-mat/mat-main.htm

Az *Acta Materialia Transylvanica. Anyagtudományi Közlemények* az Erdélyi Múzeum-Egyesület (EME) Műszaki Tudományok Szakosztályának folyóirata, amely az anyagtudományok területéről közöl tudományos közleményeket: szakcikkeket, összefoglalókat (szemléket), tanulmányokat. A folyóirat célja összképet adni kiemelten a Kárpát-medencei kutatási irányokról, tudományos eredményeiről, s ezt széles körben terjeszteni is. A folyóirat az EME felvállalt céljaihoz híven a magyar szaknyelv ápolását is támogatja, így a nyomtatott folyóirat magyar nyelven jelenik meg, mely az Erdélyi digitális adattárban elérhető (https://eda.eme.ro/handle/10598/30356). A széles körű nemzetközi terjesztés érdekében a folyóirat teljes angol nyelvű változatát is közzétesszük.

Acta Materiala Transylvanica – Material Sciences Publications – is a journal of the Technical Sciences Department of the Transylvanian Museum Society, publishing scientific papers, issues, reviews and studies in the field of material sciences. Its mission is to provide and disseminate a comprehensive picture focusing on research trends and scientific results in the Carpathian basin. In accordance with the general mission of the Transylvanian Museum Society it aims to support specialized literature in Hungarian. The printed version of the journal is published in Hungarian and is available in the Transylvanian Digital Database (https://eda.eme.ro/handle/ 10598/30356). However, we would like to spread it internationally, therefore the full content of the journal will also be available in English.

Tartalom / Content

Acta Materialia Transylvanica 8/2. (2025) 51–54.
DOI: Hungarian: https://doi.org/10.33923/amt-2025-02-01
English: https://doi.org/10.33924/amt-2025-02-01

Investigation of the Chemical Applicability of Used Cooking Oils

Rebeka BEJCZI,[1] Roland NAGY[2]

[1] *Pannon University, Faculty of Engineering, Bio-, Environmental and Chemical Engineering Research and Development Center, Department of MOL, Veszprém, Hungary, bejczi.rebeka@mk.uni-pannon.hu*

[2] *Pannon University, Faculty of Engineering, Bio-, Environmental and Chemical Engineering Research and Development Center, Department of MOL, Veszprém, Hungary, nagy.roland.dr@mk.uni-pannon.hu*

Abstract

Cooking oils play a crucial role in the food industry; however, during the cooking process, they undergo significant physical and chemical transformations that affect their subsequent usability and environmental impact. Our results show that oxidized rapeseed oil exhibits similar properties to industrial raw rapeseed oil, suggesting that used cooking oils at a certain oxidation state could potentially be suitable for surfactant synthesis. Since surfactants are widely used across various industries, this recycling approach offers a sustainable alternative to synthetic raw materials.

Keywords: *used cooking oil, oxidation, rapeseed oil, sustainability.*

1. Introduction

Used cooking oils (UCOs) play a significant role in the food industry; however, during the frying process, they undergo chemical and physical transformations that affect their subsequent usability and environmental impact [1].

Fresh cooking oils are typically derived from vegetable or animal fats, with triglycerides as their main components. Commonly used vegetable oils include palm, sunflower, rapeseed, and soybean oils, while among animal-derived fats, lard is the most frequently mentioned. The oxidative stability and fatty acid composition of cooking oils are key factors in their selection, as they influence the chemical reactions occurring under heat exposure [2, 3]. High temperatures lead to the formation of free fatty acids, aldehydes, ketones, and polymers, which degrade oil quality, increase viscosity, and pose health risks [4, 5]. Improperly managed waste oil can contribute to environmental pollution, highlighting the importance of sustainable recycling strategies [6, 7, 8].

The recycling of UCOs offers environmental and economic benefits, supporting a sustainable, circular economy. One of the most common methods is biodiesel production via transesterification, which reduces carbon dioxide emissions and dependence on fossil fuels. Life cycle assessments confirm that UCO-based biodiesel is more environmentally friendly, and triglycerides can also serve as raw materials for surfactants and construction additives. Surfactants derived from UCOs present a sustainable alternative to synthetic materials, reducing waste generation and the demand for new raw materials [9, 10, 11].

Our research was aimed at modeling the physical and chemical changes occurring during the frying process of rapeseed oil, with particular focus on oxidative stability, total acid number, saponification number, iodine-bromine number, and kinematic viscosity. Additionally, efforts were made to expand the range of raw materials suitable for surfactant synthesis by determining whether oxidized rapeseed oil from frying could potentially be applied for synthesis purposes.

2. Materials

For the experiments, cooking oil, rapeseed oil was utilized as the raw material. Its properties are summarized in Table 1. As a reference, the properties of crude, unrefined rapeseed oil typically used in industrial surfactant synthesis were also examined.

Table 1. *Properties of used materials*

Properties	RO-cook	RO-crude
Physical state (20 °C)	liquid	liquid
Density, d_{420} (kg/m³)	0.882	0.91
Boiling point (°C)	347	341
Flash point (°C)	225	214
Pour point (°C)	-9	-8
Molecular weight (g/mol)	900	900
Dynamic viscosity (40 °C mPas)	32.69	30.14

The rapeseed oils used in the experiments were supplied byBunge Zrt.

3. Methods

Edible rapeseed oil was subjected to oxidation to simulate the frying processes and the associated chemical changes occurring during various applications. Following the aging procedures, the physical and chemical properties of the oils were analyzed in detail to identify potential changes and assess their impact on future applicability.

3.1. Oxidative stability

The resistance of oils to air (oxygen) is characterized by their oxidative stability, which was determined according to the IP 157 [12] standard. The oxidation parameters are summarized in Table 2.

Table 2. *Oxidation parameters*

Parameter	RO-cook (ox-1)	RO-cook (ox-2)
Temperature, °C	170	170
Time, h	8	16
Air, dm^3/h	20	20
Volume of oil, cm^3	20	20

3.2. Total acid number

The total acid number (TAN) is a measure of the amount of weak organic and strong inorganic acids in the oil. It was determined following the ASTM D974 [13] standard.

3.3. Saponification number

The saponification number expresses the amount of potassium hydroxide (mg KOH/g) required to completely saponify 1 g of a given substance. This was determined according to the ISO 3657 [14] standard.

3.4. Iodine-bromine number

The iodine-bromine number provides information on the degree of saturation and unsaturation of the oils, which was examined according to the MSZ EN 14111:2004 [15] standard.

3.5. Kinematic viscosity

Kinematic viscosity (KV) was determined at 40 °C following the ASTM D445-06 [16] standard.

4. Results

The experimental results are summarized in tables.

Fig. 1 illustrates that the total acid number of the oxidized samples increased compared to the edible rapeseed oil, indicating that the frying process led to an increase in free fatty acid content.

Fig. 2 presents the saponification number of the oxidized samples, which showed an increase. Notably, the saponification number of the sample oxidized for 16 hours equaled that of crude rapeseed oil.

As a result of oxidation, the iodine-bromine number of cooking rapeseed oil decreased, with a similar value observed for crude rapeseed oil (Fig. 3).

Table 3. *Kinematic viscosity of the samples*

Samplke	KV at 40 °C (mm^2/s)
RO-crude	41.0
RO-cook	43
RO-cook (ox-1)	57.3
RO-cook (ox-2)	123.3

The kinematic viscosity increased due to oxidation (Table 3), which can be attributed to polymerization reactions and contamination.

Our results indicate that significant differences can be observed between the properties of the examined raw materials and those of industrial crude rapeseed oil, with both lower and higher values. As a result, the property range of potential raw materials has been successfully expanded, representing an important step in evaluating alternative vegetable oils and used oils for surfactant synthesis.

5. Conclusions

Our findings confirm that the aging of rapeseed oil induces significant physical and chemical changes that may influence its subsequent applications. Oxidation led to an increase in both the total acid number and the saponification number, while the decrease in the iodine-bromine number indicates the degradation of unsaturated fatty acids. The rise in kinematic viscosity reflects modifications in the molecular structure, which can

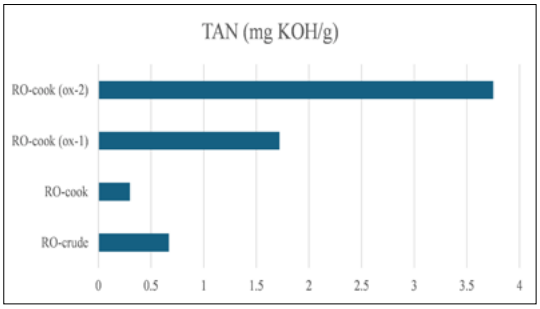

Fig. 1. *Total acid number of the samples.*

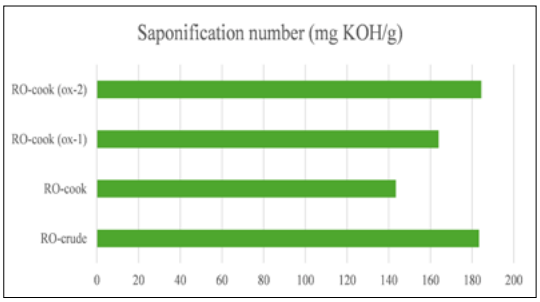

Fig. 2. *Saponification number of the samples.*

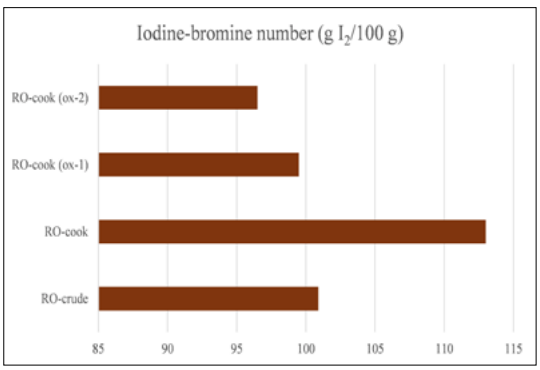

Fig. 3. *Iodine-bromine number of the samples*

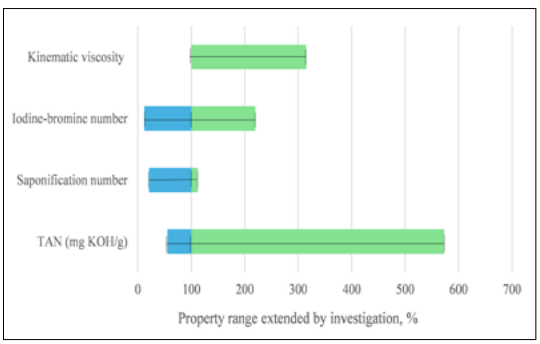

Fig. 4. *Summary of the results*

affect industrial applicability.

It was established that, based on the similar properties of industrial crude rapeseed oil and the oxidized samples, used cooking oils may also be suitable for surfactant synthesis. This broadens the range of applicable raw materials and contributes to promoting sustainable raw material utilization while reducing the environmental burden associated with waste cooking oil disposal. Our results support the optimization of used cooking oil recycling and the expansion of raw material sources; however, further studies are needed to determine the optimal processing conditions.

Acknowledgements

The university researcher scholarship program code 2024-2.1.1-EKÖP of the ministry of culture and innovation was prepared with the support of the national research, development and innovation financial scheme.

References

[1] Awogbemi O., Onuh E. I., Inambao F. L.: *Comparative study of properties and fatty acid composition of some neat vegetable oils and waste cooking oils.* International Journal of Low-Carbon Technologies, 14/3. (2019) 417–425. https://doi.org/10.1093/ijlct/ctz038

[2] Ifijen I., Nkwor A.: *Selected under-exploited plant oils in Nigeria: A correlative study of their properties*. Tanzania Journal of Science, 46/3. (2020) 817–827. https://doi.org/10.4314/tjs.v46i3.21

[3] Hillairet F., Allemandou V., Golab K.: *Analysis of the current development of household UCO collection systems in the EU*. GREENEA, Coivert, France, 2016.

[4] Dinovitser A., Valchev D. G., Abbott, D.: *Terahertz time-domain spectroscopy of edible oils*. Royal Society Open Science, 4/6. (2017) 170275. https://doi.org/10.1098/rsos.170275

[5] Riera J. B., Codony R.: *Recycled cooking oils: Assessment of risks for public health*. 2000.

[6] Mannu A., Ferro M., Pietro M. E. D., Mele A.: *Innovative applications of waste cooking oil as raw material.* Science Progress, 102/2. (2019) 153–160. https://doi.org/10.1177/0036850419854252

[7] Mendecka B., Lombardi L., Kozioł J.: *Probabilistic multi-criteria analysis for evaluation of biodiesel production technologies from used cooking oil.* Renewable Energy, 147. (2020) 2542–2553. https://doi.org/10.1016/j.renene.2017.05.037

[8] Orjuela A., Clark J.: *Green chemicals from used cooking oils: Trends, challenges, and opportunities.* Current Opinion in Green and Sustainable Chemistry, 26. (2020) 100369 [9]reb21 https://doi.org/10.1016/j.cogsc.2020.100369

[9] Gupta M.: *Practical guide to vegetable oil processing*. Elsevier, 2017.
[10] Mannu A., Garroni S., Ibanez Porras J., Mele A.: *Available technologies and materials for waste cooking oil recycling*. Processes, 8/3. (2020) 366. https://doi.org/10.3390/pr8030366
[11] Permadani R. L., Ibadurrohman M., Slamet: *Utilization of waste cooking oil as raw material for synthesis of Methyl Ester Sulfonates (MES) surfactant*. In: IOP Conference Series: Earth and Environmental Science, 105/1. (2018) 012036. https://doi.org/10.1088/1755-1315/105/1/012036
[12] IP 157: Determination of the oxidation stability of inhibited mineral oils, 2025.
[13] ASTM D974: Standard Test Method for Acid and Base Number by Color-Indicator Titration, 2023.
[14] ISO 3657: Animal and vegetable fats and oils – Determination of saponification value, 2020.
[15] MSZ EN 14111:2004: Zsír- és olajszármazékok. Zsírsav-metil-észterek (FAME). A jódszám-meghatározása, 2012.
[16] ASTM D445-06: Standard Test Method for Kinematic Viscosity of Transparent and Opaque Liquids (and Calculation of Dynamic Viscosity), 2012.

Acta Materialia Transylvanica 8/2. (2025) 55–59.
DOI: Hungarian: https://doi.org/10.33923/amt-2025-02-02
English: https://doi.org/10.33924/amt-2025-02-02

ACTA MATERIALIA TRANSYLVANICA

Effect of Laser Welding Parameters on the Microstructure of Lath-martensitic Thin Steel Plates

Enikő Réka FÁBIÁN

Óbuda University, Bánki Donát Faculty of Mechanical and Safety Engineering, Institute of Materials and Manufacturing Sciences, Department of Material Technology. Budapest, Hungary, fabian.reka@bgk.uni-obuda.hu

Abstract

In this study lath martensitic microstructure in S235JR and Mn-B alloyed steel sheets were produced. The Mn-B steel used as A and B pilar at autocars Laser welded blanks are an innovative way for automakers to reduce the weight of their vehicles while improving safety at the same time. We created welded joints with different parameters. Welding with 4100mm/min speed the weld metal hardness is similar to the late martensitic base material, and only a narrow heat affected zone is softened. Welding with lower speeds resulted softening of the weld metal and a double heat-affected zone: hard next to the weld metal and soft outside it.

Keywords*: lath martensite, laser welding, hardness.*

1. Introduction

The characteristics of the martensitic microstructure of steels depend on the carbon content of the steel. According to Krauss [1], during hardening, if the carbon content is below 0.6%, lath martensite is formed in the microstructure. Between 0.6% and 1%, we can speak of a mixed microstructure, which becomes increasingly plate-like rather than lath-like as the carbon content increases. With a carbon content above 1%, plate martensite is obtained. Literature data show that lath martensite appears below a carbon content of 0.6%, but below 0.3% C, this structure appears purely as a result of rapid cooling from the austenitic state [2, 3]. The lath martensite has a characteristic multilevel microstructure. The lath martensite is formed in parallel of parquet- or lath-like crystallites called laths.

Lath martensite consists of parallel laths, which are crystallites. Lath martensite characteristicaly has a multi-level microstructure. The transforming austenite contains several bundles. Each bundle consists of blocks bounded by large-angle grain boundaries, which in turn are formed by lamellae [4]. Numerous articles have been published in recent years on the formation and crystallographic analysis of lath martensite microstructures [5, 6]. As the C content increases, the structure of the blocks and bundles becomes finer [7, 8]. Depending on the carbon and alloying elements content researchers have created lath martensite by rapid cooling from high temperatures [7, 8, 9, 10].

The lower the carbon content of the steel, the higher the austenitizing temperature and the faster the cooling rate must be in order to create a pure martensitic structure [9, 10]. According to literature data [11] commercial hot-rolled high strength steel plates microalloyed with boron (C = 0.25%, Mn = 1.20%, B=0,006%), after austenitization at 950 °C, can form nearly 100% martensite by cooling at a rate of 100 °C/s, and nearly 71% martensite and 29% ferrite at a cooling rate of 50 °C/s. In another series of experiments, Morito et al [12] have produced lath martensitic microstructure at high-nickel and cobalt alloyed maraging steel and at two boron-microalloyed steels with very low carbon content. All three steels were cooled in brine from an austenitizing temperature of 1200 °C.

In the automotive industry, boron- and manganese-alloyed, press-hardened martensitic steels are used to form A and B pillars [13]. Martensite with a lath structure can support significant deformation [14]. The automotive industry aims to intro-

duce laser welding joints in high-strength steels in order to save material [15]. There is no data in the literature on what happens to the martensitic structure formed by press hardening during laser welding.

2. Experimental materials, experimental background

For the experiments, we used S235JR and PHS®1500 press-hardened steel (branded Usibor®1500 by Acelor Mital) commonly used in the automotive industry. According to the manufacturer's data sheet, the chemical composition of the PHS®1500 steel is: C=0.22%, Mn=1.3%, B=0.0035%, Si=0.25% [16].

Before heat treatment, the coating layer on the surface of the PHS 1500 steel sheet was removed. The samples were then austenitized in a laboratory furnace at a temperature of 1100 °C and then quenched in ice water. The microstructure of the samples after quenching is shown in Fig. 1. The average hardness of the unalloyed steel sheet with lower carbon content was 293HV1, while the hardness of the Mn-B alloyed sample was 450 HV1 after heat treatment.

After fitting the heat-treated samples together, we welded them using a Trump TLF 5000 turbo CO2 device. The technological data set for the test is shown in Table 1. The welding parameters described here were determined based on empirical data. Due to the reduction in welding speed, the focus spot position had to be adjusted in order to achieve a properly penetrated weld.

Table 1. *Welding data*

Nr.	Power (W)	Method	Speed (mm/min)	Focus position (mm)
I	5000	CW	4100	0
II	5000	CW	2500	+5
III	5000	CW	1300	+7.5
IV	5000	CW	1050	+10

Metallographic polishes were prepared from the samples. Cutting was performed on a metallographic cutting machine with water cooling. The cross-section samples were prepared using traditional metallographic methods and then examined using a Keyence VHX-2000E light microscope. After the light microscopic examination, ultrasonic hardness measurements were performed on the samples. The hardness measurements were performed using a Krautkramer Branson Microdur II device. The load force was 1 kg in all cases. We measured the change in hardness on the samples near the crown surface so that in each case the measurement range was: base material - heat-affected zone - weld metal - heat-affected zone - base metal.

3. Test results

In the case of Mn-B alloy steel, the welds were formed across the entire cross-section of the plate under the parameters used. In the case of Mn-B alloy steel, the laser technology parameters shown in Table 1 resulted in good through welds. No significant porosity or cracks were observed (Fig. 2), despite the fact that the base material is highly resistant and a high-hardness microstructure formed either in the weld or in the heat-affected

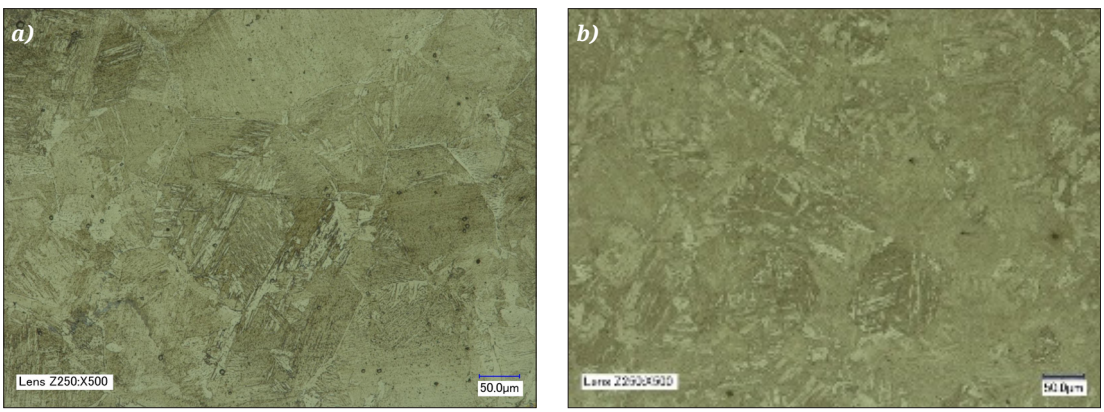

Fig. 1. *Microstructure of heat-treated steels: a) S235, b) Mn-B alloyed steel.*

zone, as can be seen in Fig. 3 which shows the hardness measurement results.

According to the hardness measurement results, when welding was effectuated at a speed of 4100 mm/min, the hardness of the weld metal, which is barely more than 1 mm wide, is equal to the hardness of the lath martensitic base material. Hardness decreased to 310–330 HV1 in the very narrow heat-affected. When welding at a speed of 2500 mm/min, the hardness decreased to 310 HV1 in the center line of the weld metal and in the narrow heat-affected zone, while the weld metal is characterized by a hardness above 400 HV1, despite the fact that the grain boundaries of the weld metal are ferritic (Fig. 4). In the central 0.8 mm zone of the weld metal of sample III, the hardness varied between 250 and 290 HV1, followed by a 0.7 mm high-hardness (470-500 HV1) heat-affected zone and a narrow 310 HV1 heat-treated zone.

Welding at 1050 mm/minute resulted in the lowest hardness (240-270 HV1) weld metal, which was 1.8 mm wide, with a 0.5 mm heat-affected zone with a hardness above 400HV1, outside of which the hardness fell below 300HV1 in a narrow range.

Although in the case of boron micro-alloyed steel the hardnesses reached 500 HV1 in some places, we did not find any cracks in any of the samples. A possible explanation for this favorable property in terms of crack formation is the cubic lattice structure [17]. due to low carbon content.

Literature data show that in boron-micro-alloyed steels, the boron segregation can cause grain boundary cracks [18]. If the cooling rate is high, boron segregation does not appear

Welding of martensitic low-carbon unalloyed steel plate samples according to the data in Table 1, shows that even at a welding speed of 4100 mm/min, a narrow continuous, full-penetrated weld was formed, as can be seen in the images in Fig. 5 When the highest welding speed was used, the hardness of the weld metal was the same as that of the martensitic base material, followed by a narrow (~0.3 mm wide) softened heat-affected zone, as shown in Fig. 6.

At a welding speed of 2500 mm/min the weld metal achieved a hardness of 240–250 HV, in the range of 0.2–0.3 mm, it reaches the characteristic hardness of martensitic base material, followed by slight softening in the narrow heat-affected zone.

At a welding speed of 1300 mm/min, the characteristic hardness of the weld metal and heat-affected zone was around 200 HV1, with one or two outliers.

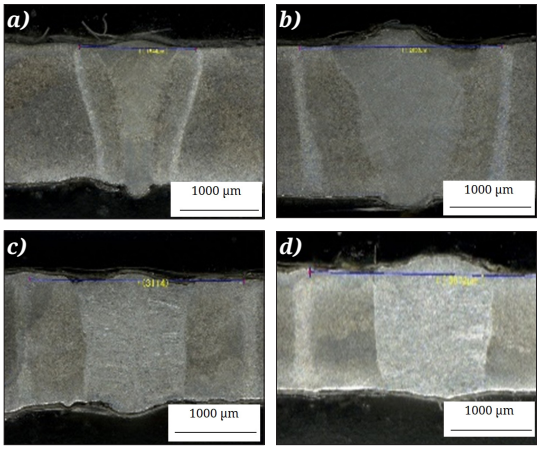

Fig. 2. *Macrographs of welds on Mn-B alloy steel samples.*
a) v = 4100 mm/min, b) v = 2500 mm/min, c) v = 1300 mm/min, d) v = 1050 mm/min

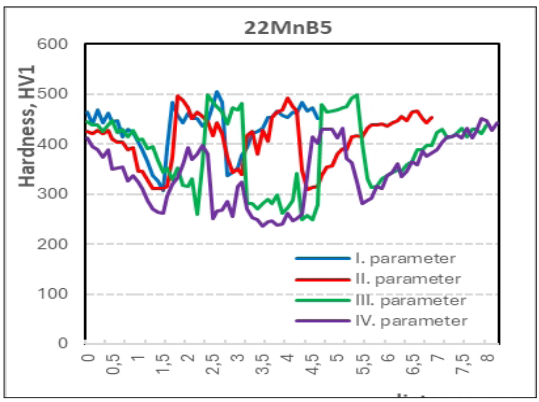

Fig. 3. *The effect of welding speed on hardness changes in the weld-metal and its surroundings in the case of Mn-B alloyed steel.*

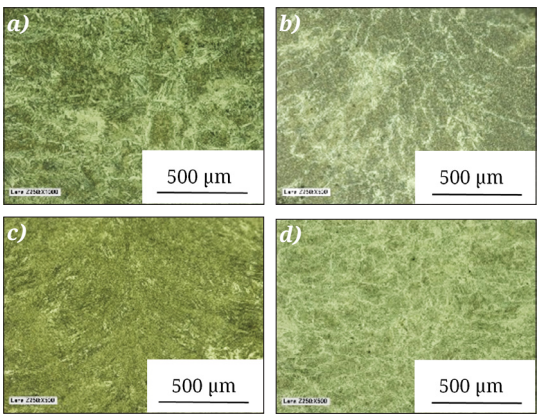

Fig. 4. *The microstructure of weld-metal in the case.*
a) v = 4100 mm/min,
b) v = 2500 mm/min, c) v = 1300 mm/min,
d) v = 1050 mm/min

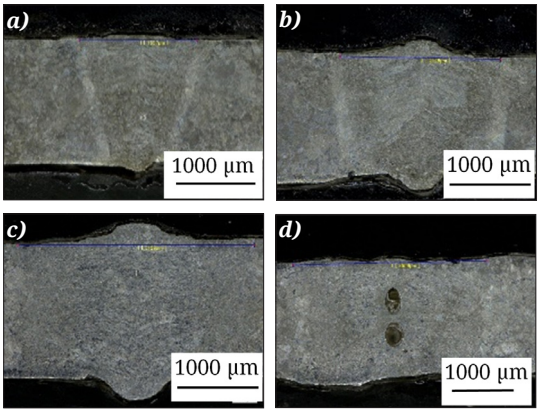

Fig. 5. *Macrographs of welds on S235JR steel samples a) v = 4100 mm/min, b) v = 2500 mm/min, c) v = 1300 mm/min, d) v = 1050 mm/min*

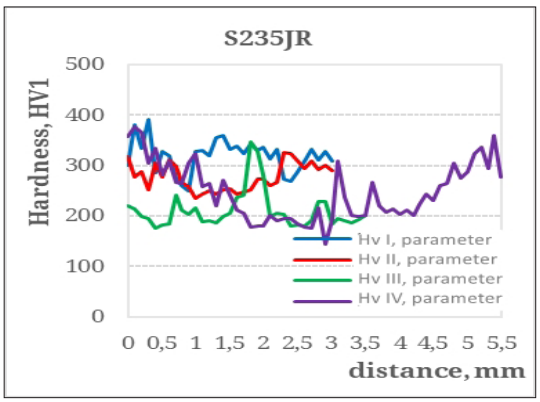

Fig. 6. *The effect of welding speed on hardness changes in the weld-metal and its sur-roundings in the case of S235JR steel.*

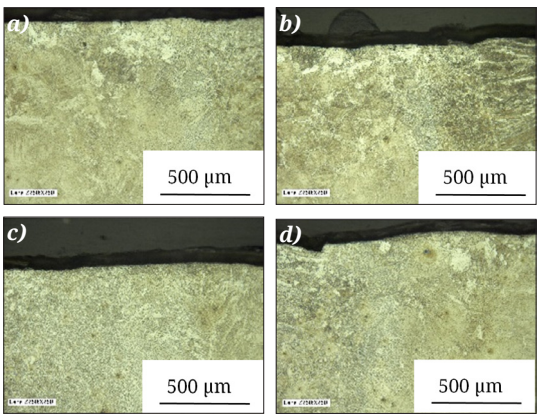

Fig. 7. *Heat affected zones after laser welding of martensitic S235JR sheet at different welding speed a) v = 4100 mm/min, b) v = 2500 mm/min, c) v = 1300 mm/min, d) v = 1050 mm/min.*

When we used a welding speed of 1050 mm/min, we found soft weld-metal, with a hardness below 200 HV1 over a width of more than 2 mm, gradually increasing towards the base material. Using this welding speed, large porosities were observed, as can be seen on **Fig. 5** d). The formation of porosity can be attributed to the excessively low welding speed. There are data in the literature indicating that in laser welding, if the welding speed is not high enough, a plasma channel begins to form at the start of welding and then deepens. Subsequently, due to the flow conditions of the melt, the plasma channel collapses, the gas inclusion remains in the material, and then the plasma channel begins to form again **[19]**.

The hardnesses that develops in the heat-affected zone of the welds can be explained by changes in the microstructure, which are presented in **Fig. 7**.

4. Conclusions

In the present experiments, laser welding of two low-carbon steel grades was investigated, which were previously martensitically hardened

During laser welding of low-carbon lath martensitic steels, no cracks formed in the weld or its heat-affected zone, even in Mn-B-alloyed steel, where the hardness approached 500 HV1 in some places when high welding speeds were used.

It was found that a welding speed of 4100 mm/min resulted in complete weld penetration for the sheet thicknesses used in the automotive industry, with the hardness of the weld metal approaching that of heat-treated martensite, with a narrow softening heat-affected zone in both steel grades tested. In the case of Mn- and B-alloyed materials, the weld metal softened at a welding speed of 1300 mm/min, while in the case of S235JR material, even a welding speed of 2500 mm/min caused softening.

A welding speed of 1050 mm/min is too low, and large porosities relative to the weld were also formed in the S235JR steel plate.

References

[1] Krauss G.: *Principles of Heat Treatment of Steel.* ASM international, USA, Materials Park, Ohio, 1980. 52.

[2] Stormvinter A., Peter Hedström P., Borgenstam A.: *Investigation of Lath and Plate Martensite in a Carbon Steel.* Solid State Phenomena, 172–174. (2011) 61–66. ISSN 1012-0394. https://doi.org/10.4028/www.scientific.net/SSP.172-174.61

[3] Galindo-Nava E. I., Rivera-Díaz-del-Castillo P. E. J.: *Understanding the factors controlling the hardness in martensitic steels.* Scripta Materialia, 110.

(2016) 96–100. ISSN 1359-6462. https://doi.org/10.1016/j.scriptamat.2015.08.010.

[4] Sandvik B. P. J., Wayman C. M.: *Crystallography and substructure of lath martensite formed in carbon steels.* Metallography, 16/2. (1983) 199–227. https://doi.org/10.1016/0026-0800(83)90005-8

[5] Kelly P. M.: *Crystallography of lath martensite in steels. Materials Transactions*. JIM (Japan), 33/3. (1992) 235–242. https://doi.org/10.2320/matertrans1989.33.235

[6] Ball J. M., Carstensen C.: *Nonclassical austenite-martensite interfaces*. Le Journal de Physique, IV. 7(C5), (1997) 35–40. https://doi.org/10.1051/jp4:1997505

[7] Morito S., Tanaka H., Konishi R., Furuhara T. & Maki T.: *The morphology and crystallography of lath martensite in Fe-C alloys.* Acta Materialia, 51. (2003) 1789–1799. https://doi.org/10.1016/S1359-6454(02)00577-3

[8] Morito S., Adachi Y., Ohba T.: *Morphology and Crystallography of Sub-Blocks*. Materials Transactions, 50/8. (2009) 1919–1923.

[9] Fábián E. R., Kótai Á.: *A léces martenzit viselkedése hőkezelés hatására.* Acta Materialia Transylvanica, 1/1. (2018). 26–30. https://doi.org/10.2478/amt-2018-0007

[10] Szabó P. J.: *Intenzív alakítási és hőkezelési folyamatok mikroszerkezetre gyakorolt hatásának értelmezése visszaszórt elektrondiffrakcióval.* BME 2012, MTA doktori mű.

[11] Lopez Granados N. M., Salinas Rodriguez: *A ˙EBSD Investigation on Effect of Cooling Rate on Microstructure and Transformation Textures of High Strength Hot-rolled Steel Plates*. Journal of Iron Steel Research International, 23/3. (2016) 261–269. https://link.springer.com/article/10.1016/S1006-706X(16)30043-7

[12] Morito S., Huang X., Furuhara T., Maki T., Hansen N.: *The morphology and crystallography of lath martensite in alloy steels.* Acta Materialia, 54. (2006) 5323–5331. https://doi.org/10.1016/j.actamat.2006.07.009

[13] Tisza M.: *Hot Forming of Boron Alloyed Manganese Steels*. Materials Science Forum, 885. (2017) 25–30. https://doi.org/10.4028/www.scientific.net/msf.885.25

[14] Huang J., Li L., Luo Z., Huang M., Peng Z., Gao J., Ke H., Liang Z.: *Improving the ductility of ultra-high strength lath martensite through heterogeneous carbon distribution*. Journal of Materials Research and Technology, 27/November–December (2023) 8209–8215.

[15] Autóipari alkalmazások. Újdonságok az autóipar területén. https://automo-tive.arcelor-mittal.com/tailored_blanks_home/LWB_home/LWB_hotstamping (letöltve: 2025. december 18.)

[16] Press Hardening Steel Grades, World Auto Steel. https://ahssinsights.org/metallurgy/steel-grades/phs-grades/ (letöltve: 2025. december 12.)

[17] Babu S. R., Nyyssönen T., Matias Jaskari M., Järvenpää A., Davis T. P., Pallaspur S., Kömi J., Porter D.: *Observations on the Relationship between Crystal Orientation and the Level of Auto-Tempering in an As-Quenched Martensitic Steel.* Metals 9/12. (2019) 1255. https://doi.org/10.3390/met9121255

[18] Bai J., Jin S., Liang Ch., Li X., You Z., Zhao Y., Liu L., Sha G.: *Microstructural origins for quench cracking of a boron steel: Boron distribution.* Materials Characterization, 190. (2022) 112022. ISSN 1044-5803. https://doi.org/10.1016/j.matchar.2022.112022

[19] Runqi Lina Hui, Wangb Fenggui, Lua Joshua, Solomonb Blair E. Carlsonb: *Numerical study of keyhole dynamics and keyhole-induced porosity formation in remote laser welding of Al alloys.* International Journal of Heat and Mass Transfer, 108. Part A, May (2017) 244–256.

Acta Materialia Transylvanica 8/2. (2025) 60–65.
DOI: Hungarian: https://doi.org/10.33923/amt-2025-02-03
English: https://doi.org/10.33924/amt-2025-02-03

The Influence of Infill Patterns on Tooth Root Rigidity by Additive Gear Manufacturing

Károly-István GÁL,[1] Attila-Levente GERGELY,[2] Márton MÁTÉ[3]

[1] *Sapientia University Târgu-Mureș, Dep. of Mechanical Engineering, Romania, gal.karoly@phd.uni-obuda.hu, gal.karoly@ms.sapientia.ro*

[2] *Sapientia University Târgu-Mureș, Dep. of Mechanical Engineering, Romania, agergely@ms.sapientia.ro*

[3] *Sapientia University Târgu-Mureș, Dep. of Mechanical Engineering, Romania, mmate@ms.sapientia.ro*

Abstract

In this study, we present an analysis of the infill patterns of 3D-printed gears with the aim of optimizing their load- capacity. During the investigation, we developed custom infill patterns, taking into account the influence of the direction of forces which occur under service. These patterns were compared with the Gyroid infill, which is the most commonly recommended in the literature. The examined gears were cylindrical involute gears, and the mass of the part was used as a reference parameter during the printing process.
A unique infill pattern was designed and combined with the Gyroid infill, then compared to the conventional Gyroid infill structure. The load-bearing capacity of different infill structures was determined by applying a simple static load test. Three gears were printed for each infill pattern, and three individual static load-bearing tests were performed on each gear.
Since plastic gears were used in this study, the central bore of the gears was modified. This modification was necessary because, if a simple keyway solution had been applied, the gears could have rotated on the shaft due to the applied torque. To prevent this, the central bore was replaced with a hexagonal design.

Keywords: *gear, infill pattern, load-bearing capacity, static load test, involute.*

1. Introduction

Nowadays, the processing and recycling of plastics are gaining increasing attention, especially from the perspective of sustainable manufacturing. One of the most widespread plastic processing methods is injection molding, which is readily used in the automotive industry, packaging industry, and in the production of electronic devices. The advantage of injection molding is rapid and economical mass production; however, it has a significant disadvantage, namely the high upfront cost of the tool. In contrast, additive manufacturing technologies – especially FDM (Fused Deposition Modelling) – have gained increasing popularity in recent years, as they minimize waste through layer-by-layer material construction and provide opportunities for the rapid production of components with unique and complex geometry.

With the development of FDM technology, an increasingly wide range of materials has become available, including carbon fiber and glass fiber reinforced polymers, which improve mechanical properties and wear resistance. In the present research, we used the FFF (Fused Filament Fabrication) additive technology. Since most gears used in household appliances are made of plastic, along with cost-effectiveness, reduced service life must be taken into account, mainly due to operation at high rotation speeds and wear resulting from material properties [9]. Replacing these gears is often cumbersome, as product catalogs in many cases do not contain standard dimensions, making individual replacement difficult.

In the case of FFF technology printed gears, the appropriate infill pattern and optimal printing parameters are crucial for mechanical performance. During our research, we compared the effect of different infill patterns on the load-bearing capacity of gears.

2. Design of the General Tooth Profile and 3D Model

At the beginning of the research, we determined that we would apply the most widespread tooth profile, the involute profile, since we intended to investigate involute cylindrical gears [4].

To create the 3D model, the first step is to develop the tooth profile and the corresponding root curve. Both the profile and the root curve are created in the Mathcad environment. The following parameters were used to development the tooth profile [4, 5]:

- modul: $m = 5$ mm,
- specific tooth addendum height: $h_0 = 1$,
- specific backlash: $c_0 = 0.25$,
- number of teeth: $z_1 = 17$,
- tooth height: $a = (h_0 + c_0)m = 6.25$ mm,
- gear width: $b = 20$ mm.

Arc segments of equal length were used to construct the gear tooth profile to achieve a more precise geometry. The root curve was not determined using the standard formula $\rho_{0f} = 0.38$ m [6] but rather based on literature [7] striving for a more robust root design. With this approach, our aim was to optimize the load distribution and increase the service life of the gear. However, in the present research, we will not delve into a detailed analysis of this.

The root and tooth profile are illustrated in Fig. 1.

The 3D model was developed in the Autodesk Inventor environment, using the profile points exported from Mathcad. To create the model, we applied specific Autodesk Inventor commands such as Extrude, Circular Pattern, Mirror, etc. [8]. The geometry created this way ensured precise tooth profile reconstruction, which is essential for further simulations and manufacturing processes. The model can be seen in Fig. 2.

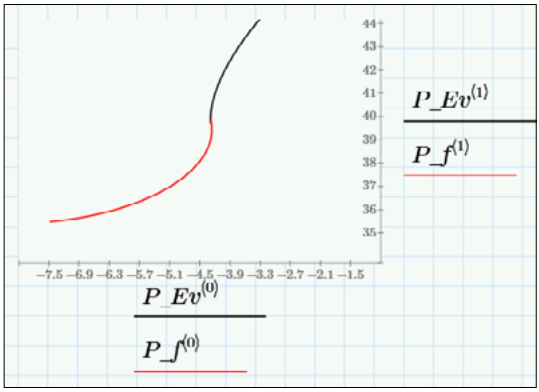

Fig. 1. *Involute profile with specialized root curve.*

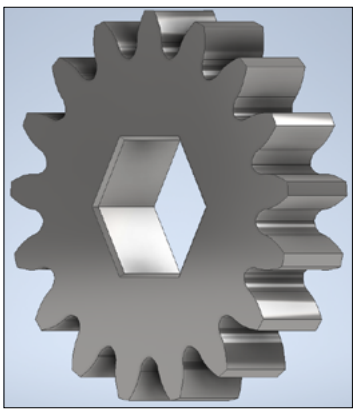

Fig. 2. *The Inventor model of the applied involute cylindrical gear.*

3. Development of specialized patterns

3.1. Levoid infill pattern

All patterns were created in the Autodesk Inventor environment, and in each case the model was developed by modifying the existing gear model. During the design of the patterns, special attention was paid to the precise setting of geometric parameters to ensure they meet the desired mechanical properties. The wall thickness was set to 0.8 [mm] in all cases, as this thickness provides the appropriate balance between mechanical strength and material usage, while minimizing the disadvantages arising from excessive material consumption.

The supports, were designed by taking into account the symmetry line of the tooth. Additionaly, we designed 0.8 [mm] wide supports along the line connecting the intersection point of the root curve radii and the gear axis. These supports ensure that the gear structure does not deform during printing, and the component maintains its shape even under maximum load.

The Levoid infill (resembling leaf venation (Fig. 3) was created by designing additional support elements at a 75° angle to the tooth's axis of symmetry. The width of these supports was 0.4 mm in all cases to provide sufficient stability while minimizing material usage. The distance between the supports was determined to be 1 mm, as this distance ensures that the printed pattern is strong enough but does not excessively strain the material. The arrangement and dimensioning of the support elements are crucial in ensuring the strength and long service life of the printed components.

Since we were working with plastic gears, we modified the central bore of the gears. This was necessary because in the case of a simple keyway fixing, the gears could have rotated on the shaft due to the applied torque. To prevent this, we designed the central bore with a hexagonal shape, thereby ensuring more secure torque transmission (**Fig. 4**).

3.2. Hybrid Levoid infill

In this case, we combined the Levoid and conventional Gyroid infills to optimize the mechanical performance and material usage of the gears. The infill of the teeth was Levoid, as this pattern is presumed to be suitable for ensuring long-term load-bearing capacity and achieving the necessary stability. However, the core of the gear was designed with 30% Gyroid infill (**Fig. 5**), as the Gyroid structure is ideal for weight reduction and maintaining structural integrity while providing the desired mechanical properties.

We apply the Gyroid infill within a circle of 71.264 [mm] diameter to maintain the external wall thickness at 0.8 [mm] in all cases. This approach ensures that the outer layer of the gear is strong enough to withstand the forces occurring during operation, while the internal structure remains lighter. The Gyroid infill is a complex geometric pattern, and its development using analytical methods is a very complicated task. Therefore we used the slicing software, which automatically generated the appropriate fill pattern for 3D printing..

We illustrate the sliced hybrid Levoid model in **Fig. 6**. This combined infill structure enables the gear to potentially achieve optimal mechanical properties in both regions: the load-bearing capacity and wear resistance of the teeth could presumably be improved thanks to the Leaf infill, while the central part of the gear would remain lighter and more flexible, yet retain the required strength due to the Gyroid infill.

3.3. Conventional Gyroid infill

We created a version with entirely Gyroid infill for comparison purposes. The aim was to examine the effect of infill methods on structural strength, weight savings, and manufacturing processes.

Additionally, in this case we applied a 30% Gyroid infill within a circle of 71.264 [mm] diameter, ensuring the preservation of the 0.8 [mm] external wall.

For the internal structure of the teeth, we applied a denser, 56% Gyroid infill. The purpose of this

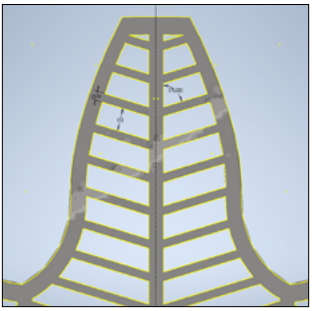

Fig. 3. *Levoid infill pattern.*

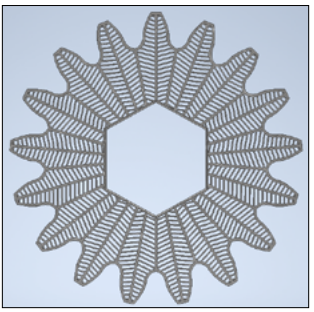

Fig. 4. *100% Levoid infill.*

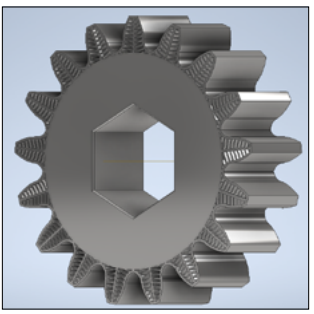

Fig. 5. *Hybrid Levoid infill.*

was to ensure that the mass of the subsequently created gears matched, regardless of which infill structure we used. This method allowed gears with different geometries to have similar dynamic and static properties.

The complete Gyroid infill model is illustrated in **Fig.7**. The exact formation of the infill was created by the slicer program, which automatically generated the Gyroid structure taking into account the given density parameters and geometric constraints. This approach not only simplified the design process but also ensured uniform material distribution during manufacturing and optimization of mechanical performance.

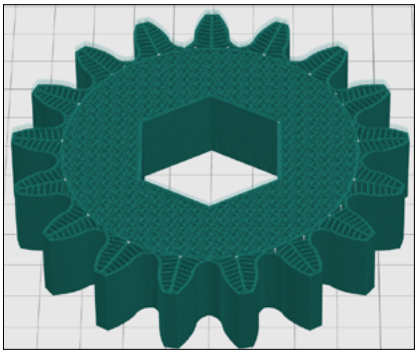

Fig. 6. *Hybrid Levoid infill: sliced model.*

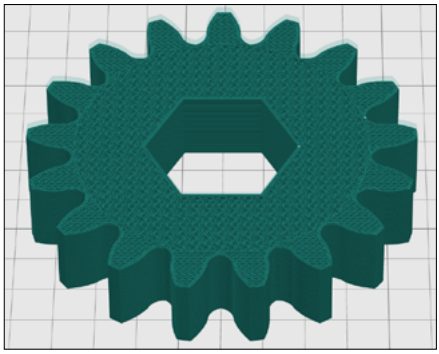

Fig. 7. *Conventional Gyroid sliced model.*

4. Manufacturing of gears using additive technology

For printing the gears, we used a bed slinger, Sovol SV07 type 3D printer operating with Klipper firmware. This printer allows for higher speed and more precise printing, which is crucial for ensuring the accurate geometry of the gears.

The used filament was AzureFilm black, matte coloured HS (High Speed) PLA. This material was specifically optimized for high-speed printing, with low shrinkage and excellent inter-layer adhesion. The matte surface is not only aesthetically advantageous but also helps reduce the visibility of the printing layers.

During the printing process, we did not use the printer's own slicing program (Sovol Cura), but rather OrcaSlicer software, which offers more advanced setting options and provides more precise control. The printing speed was set to 150 mm/s, which provided fast and efficient extrusion in accordance with the characteristics of HS PLA without compromising the adhesion between layers [9].

The settings were specifically adjusted to study the effect of the infill pattern on load-bearing capacity. For this purpose:

- We limited the number of walls to 2, minimizing the perimeter layer thickness.
- We did not apply top and bottom solid layers, so the infill structure remained directly visible and analyzable.
- The bed temperature was set to 60°C to ensure proper adhesion of the first layer and reduce the risk of deformation (warping) [9].
- The nozzle temperature was 210°C, which is optimal for proper melting and uniform extrusion of HS PLA [9];
- When designing the gears, we used mass as a reference, thereby ensuring balance and comparability between different constructions.

With these settings, the printing was fast and efficient, while ensuring the mechanical integrity and dimensional accuracy of the gears. The applied parameters enabled more accurate examination of the effects of the infill pattern, which contributed to the optimization of design and manufacturing processes.

For each printed gear, we aimed to have the mass of the gears as close as possible. The lightest gear weighed 56.395 grams, while the heaviest was 57.450 grams. This means that the difference between the masses, or the range of dispersion, was 1.055 grams. This difference can be attributed to minor variations in the printing process, such as unevenness in extrusion, temperature fluctuations, and adhesion characteristics of individual layers.

The mass constraint allowed us to ensure that the comparison of individual samples was not influenced by weight difference, allowing us to exclusively examine the effects of the infill pattern. Based on the results, it can be concluded that the printing process is acceptable from the experiment's perspective, as the mass differences remained minimal.

Regarding the printing time, the results show that there is only a minimal difference between printing times, indicating that the printing processes run reliably and uniformly. The standard deviation of the printing time for the three models is only 8 minutes.

5. Static loading tests and results

We prepared three specimens with each of the three proposed infills to generate sufficient measurement data. The manufacturing of each sam-

ple occurred under identical parameters, thus ensuring comparability and consistency of the printing process. We performed 3 measurements on each specimen, on 3 different teeth.

The static tests were conducted on a conventional TOS-250 type lathe, which provided adequate stability and precision for the experiments. A 250 mm long, 32 mm hexagonal bar was placed in the chuck of the lathe, serving as the central bore of each gear.

A 10 mm diameter cylinder was placed in the tool holder of the lathe, which was adjusted to fit into the gear tooth space. This setup enabled direct loading of the teeth and precise measurement of deformations.

A Sealey 1/2" SQ Drive Digital Torque Adapter with an accuracy of ±2% was mounted on the free end of the hexagonal bar. A ratchet wrench was connected to the torque meter, with which we gradually increased the load while monitoring the deformation of the gears and the failure torque. During the test quasi-steady state condition was maintained.

The purpose of the measurement was to obtain accurate data on the load-bearing capacity and mechanical behaviour of gears with different infill structures. The data thus obtained provide assistance in optimizing gear geometries and evaluating the practical applicability of 3D printed gears.

The measured values were summarized in the following tables.

1. Table. *Levoid infill*

	1. pcs (Nm)	2. pcs (Nm)	3. pcs (Nm)
1.	28.6	33.5	26.2
2.	24.1	23.7	30.4
3.	24.6	40.7	35.6

2. Table. *Hybrid Levoid infill*

	1. pcs (Nm)	2. pcs (Nm)	3. pcs (Nm)
1.	24.3	49	46.9
2.	26	48.6	47.1
3.	35	55.7	48.3

3. Table. *Conventional Gyroid infill*

	1. pcs (Nm)	2. pcs (Nm)	3. pcs (Nm)
1.	37.7	49.5	58.2
2.	53.8	56.4	–
3.	61	57.2	–

6. Conclusions

Our investigations confirmed that the geometry of the chosen pattern does not randomly determine the load-bearing capacity of the gears, but rather stems from the kinematics of the machine elements' operation. This is a particularly important aspect during design, as the mechanical properties and service life of gears can be optimized by selecting the appropriate infill structure.

During the destructive tests, we observed that every failure occurred at a critical displacement below the tooth root, which correlated with the alternation of the infill pattern. This indicates that the transitional zones of the material structure may be weaker, therefore increased attention should be paid to the homogeneity of the infill pattern during design.

In the case of conventional Gyroid infill, significant spikes can be observed in the measured values. This can be attributed to the fact that the slicer program randomly forms the infill, thus the arrangement of the infill may differ for each tooth. Consequently, the load-bearing capacity of gears made with such infill is not constant and is unstable, which makes this infill pattern unreliable in industrial applications.

For the Hybrid Levoid infill, the measured data suggest that the structure's load-bearing capacity is more stable than that of the simple Levoid infill, and approaches the level of conventional Gyroid infill. The measurement results show a smaller distribution, which suggests that the hybrid structure helps in more uniform distribution of the load. This indicates that hybridization can optimize the mechanical behaviour of gears, reducing stress peaks at critical loading points.

The measurement results show that the load-bearing capacity of conventional Gyroid infill is better than that of the Levoid infill pattern we developed. From the measured data, it can also be observed that the simple Levoid infill has a weaker load-bearing capacity, which is also evident from the lower average torque values.

Our results highlight that in gear design, not only the tooth profile and material selection but also the internal infill pattern play a key role in achieving optimal mechanical performance.

References

[1] Dawood L. L., AlAmeen E. S.: *Influence of Infill Patterns and Densities on the Fatigue Performance and Fracture Behavior of 3D-Printed Carbon Fiber-Reinforced PLA Composites*. AIMS Materials Science, 11/5. (2024) 833–857.

https://doi.org/10.3934/matersci.2024041

[2] Calabrese L., Marabello G., Chairi M., Di Bella G.: *Optimization of Deposition Temperature and Gyroid Infill to Improve Flexural Performance of PLA and PLA–Flax Fiber Composite Sandwich Structures*. Journal of Manufacturing and Materials Processing, 9/2. (2025) 31. https://doi.org/10.3390/jmmp9020031

[3] Lin D., Zhang X., Li J.: *Optimizing 3D Printing Parameters: Evaluating Infill Type and Layer Height Effects on Tensile Fracture Force*. Journal of emerging investigators, 2021. https://doi.org/10.59720/20-083

[4] Máté M.: *Hengeres fogaskerekek gyártószerszámai*. Műszaki Tudományos Füzetek 12. Erdélyi Múzeum-Egyesület, Kolozsvár, 2016. https://doi.org/10.36242/mtf-12

[5] Hollanda D.: *Așchiere și scule*. Reprografia I.I.S.Tg.Mureș, 1994. 234-240.

[6] Pálfi K., Prezenszky T., Csibi V., Antal B., Gyenge Cs., Balogh F.: *Fogazott alkatrészek tervezése, szerszámai és gyártása*. Gloria Kiadó, Kolozsvár, 1999.

[7] Hodgyai N., Tolvaly-Roșca F., Máté M.: *The Conditions of Undercut by Shaping Using a Rounded Profile Gear Shaper Cutter*. Műszaki Tudományos Közlemények, 14. (2021) 30–36. https://doi.org/10.33894/mtk-2021.14.05

[8] Tolvaly-Roșca F.: *A számítógépes tervezés alapjai: AutoLisp és Autodesk Inventor alapismeretek*, Műszaki Tudományos Füzetek 7. Erdélyi Múzeum-Egyesület, Kolozsvár, 2009. https://doi.org/10.36242/mtf-07

[9] Cano-Vicent A., Tambuwala M. M., Hassan Sk. S., Barh D., Aljabali Alaa A.A., Birkett M., Ajunan A., Serrano-Aroca Á.: F*used Deposition Modelling: Current Status, Methodology, Applications and Future Prospects*. Elsevier, Additive Manufacturing, 47. (2021) 102378. https://doi.org/10.1016/j.addma.2021.102378

Acta Materialia Transylvanica 8/2. (2025) 66–69.
DOI: Hungarian: https://doi.org/10.33923/amt-2025-02-04
English: https://doi.org/10.33924/amt-2025-02-04

Effect of Cryogenic Treatment on the Wear and Corrosion Resistance of the ELMAX tool Steel

Gábor KŐRÖSI,[1] László TÓTH[2]

[1] *Obuda University Bánki Donát Faculty of Mechanical and Safety Engineering. Budapest, Hungary, korosigabor.atg@gmail.com*

[2] *Obuda University Bánki Donát Faculty of Mechanical and Safety Engineering, Institute of Mechanical Engineering and Technology, Department of Materials Technology. Budapest, Hungary, toth.laszlo@bgk.uni-obuda.hu*

Abstract

In our research, we investigated how the wear and corrosion resistance properties of ELMAX tool steel change during cryogenic treatment. The tool steel was heat treated in two different ways: con-ventionally, and using cryogenic treatment. From the two differently heat treated workpieces, 3 spe-cimens each were subjected to wear and corrosion tests. Based on the obtained results, it can be sta-ted that both the wear resistance and corrosion resistance improved as a result of the cryogenic tre-atment. These properties can clearly determine the usability of the material in many applications.

Keywords: *heat treatment, cryogenic treatment, wear, corrosion.*

1. Introduction

Tool steels are fundamental pillars of modern industry, as they play a crucial role in the manufacturing of machines, tools, and equipment due to their high hardness, strength, and wear resistance.

These optimal mechanical properties are determined by the material's chemical composition and the carefully selected heat-treatment procedures, which transform the internal structure of the steel to meet specific requirements.

The heat treatment of tool steels is a complex process aimed at modifying the microstructure in such a way that the steel attains the desired properties. One of the most commonly applied procedures is the combination of quenching and tempering [1]. During quenching, the steel is heated to a high temperature (austenitic state), followed by rapid cooling, producing a hard but brittle martensitic structure. This is then followed - often in multiple steps - by tempering operations, which fine-tune the microstructure, optimizing hardness, toughness, and corrosion resistance according to the intended industrial application.

To further optimize conventional procedures, recent research has shifted toward the use of deep cryogenic treatment between quenching and the first tempering step. This operation specifically targets the refinement of the martensitic structure by minimizing the amount of retained austenite. As a result of deep cryogenic treatment, the strength and wear resistance of the steel improve.

Tempering after cryogenic treatment promotes carbide precipitation and increases martensite stability, enabling further enhancement of hardness and wear properties. Deep cryogenic treatment presents both new possibilities and new challenges in maximizing the often contradictory requirements of tool steels (e.g., toughness vs. wear resistance).

The goal of our investigation is to present and compare in detail the effects of two different heat-treatment procedures on the properties of a specific tool steel, ELMAX. The comparison focuses on the following two processes:

- Conventional procedure: Quenching followed by three tempering cycles;
- Cryogenic procedure: Quenching, cryogenic treatment, then three tempering cycles.

By comparing the results, the study illustrates the differences between the characteristics achievable by the two technologies.

Armed with these comparative results, it becomes possible to improve the efficiency of industrial production by providing guidance for selecting the appropriate heat treatment technology.

2. Material grade

The tool steel examined in this study is Uddeholm ELMAX SuperClean, distributed in Hungary by voestalpine High Performance Metals Hungary Kft [2].

Table. 1. *Chemical composition of ELMAX* [2]

Element	Content (weight %)
C (carbon)	1.7
Si (silicon)	0.8
Mn (manganese)	0.3
Cr (chromium)	18.0
Mo (molybdenum)	1.0
V (vanadium)	3.0

ELMAX is a powder-metallurgy tool steel developed by the Swedish company Uddeholm in the early 2000s.

Its purpose was to combine the advantages of traditional high-wear-resistance tool steels with the corrosion resistance of stainless steels.

Thanks to powder-metallurgy technology, it features a homogeneous microstructure and excellent properties, including high wear resistance, good machinability, and dimensional stability. It was originally developed for injection molding and extrusion tools, but today it is widely used, for example, in the production of premium kitchen knives, as well as tactical and survival knives [3].

3. Conducted Tests and Heat Treatments

To evaluate the properties, hardness measurements, wear and corrosion tests were carried out.

The specimen preparation was performed in the laboratory of Polyax Ltd. Hardness was measured using an Ernst AT130 D hardness tester.

Wear testing was conducted on polished specimens using the abrasion apparatus available in our university's materials testing laboratory (Fig. 1). Three tests were performed per specimen, each lasting 5 minutes.

The abrasive ball was made of Al_2O_3 with a diameter of 20 mm. The rotational speed of the ball drive was 570 rpm. The applied load was 72 g, which included the pivot rod and additional load. No lubricant was used during the test.

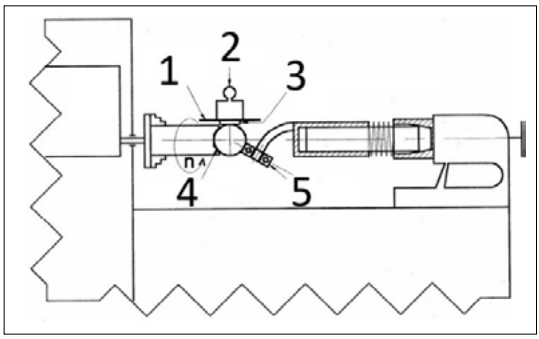

Fig. 1. Schematic of the abrasion apparatus [4]
1: Rigid plate mounted on a pivot rod, 2: Load, 3: Specimen, 4: Abrasive ball, 5: Ball bearing

Wear marks on the polished surfaces were examined using an Olympus BX53M microscope.

For corrosion testing, ASTM G31-21 [5] and its supplementary standard ASTM G1-03(2017)e1 [6]. were used as guidelines. During the tests, three specimens each were immersed in a 6% $FeCl_3$ solution for 72 hours. Corrosion resistance was evaluated based on the mass loss rate.

The specimen dimensions were identical for all tests, on the order of tenths of a millimeter: 16.0 × 10.0 × 2.5 mm.

3.1. Heat Treatments

The heat treatments were carried out at the heat treatment facility of Titán 94 Ltd (Fig. 2). Quenching, cryogenic treatment, and the first tempering were performed in a Schmetz IU72/IF 2RV vacuum furnace, while the subsequent two tempering cycles were conducted in a nitrogen gas protected tempering furnace.

The heat treatment cycle diagram is shown in Fig 3. For the conventionally treated specimens, all parameters were identical except for the cryogenic treatment.

Notable parameters include the austenitizing temperature of 1080 °C, cryogenic treatment at −150 °C, and tempering temperatures of 200-, 210-, and 180 °C, respectively.

4. Results

4.1. Hardness

The workpiece from which the specimens were machined was received in a softened state.

The average hardness values are summarized in Table 2:

Table 2. *Averaged hardness values*

	Softened	After Heat Treatment
Conventionally treated	257 HB	58 HRC
Cryogenically treated	257 HB	59 HRC

The results confirm the expected increase in hardness.

4.2. Wear Resistance

The formula used to determine the wear coefficient is:

$$K = \frac{V_v}{S \times N} \left(\frac{mm^3}{Nm}\right) \quad (1)$$

where:
- K: wear coefficient,
- V_v: lvolume loss,
- S: wear path length,
- N: applied load.

The evaluation methods and formulas applied are described in more detail in the literature [4].

The wear coefficient values determined from the abrasion tests are summarized in Table 3.

Table 3. *Averaged wear coefficients*

Average Wear Coefficient	
Conventional	10.066×10^{-6} mm^3/Nm
Cryogenically treated	4.853×10^{-6} mm^3/Nm

The obtained results also support the assertion that significant differences in wear properties can be observed even among steels with very similar hardness [7].

4.3. Corrosion Resistance

The mass loss rate (*mlr*) was determined using the following equation:

$$mlr = \frac{\Delta m}{A \times t} \left(\frac{g}{m^2 h}\right) \quad (2)$$

where:
- Δm is the mass loss caused by corrosion,
- A is the surface area of the specimen exposed to the ferric chloride solution,
- t is the exposure time in the corrosive medium

The calculated values are summarized in Table 4.

Table 4. *Averaged corrosion mass loss rates*

Corrosion Mass Loss Rate, g/(m^{2}h)	
Conventional	0.577
Cryogenically treated	0.372

These results highlight the wide range of properties achievable through different heat treatment procedures.

Acknowledgements

We would like to express our gratitude to Titán 94 Ltd. for providing access to their heat treatment equipment, to Polyax Ltd. for the use of their laboratory and instruments, and to Obuda University, Bánki Donát Faculty of Mechanical and Safety Engineering, for their support.

References

[1] Tóth L.: *Szerszámacélok tulajdonságainak változása a hőkezelés hatására.* Acta Materialia Transylvanica, 6/2. (2023) 114–120. https://doi.org/10.33923/amt-2023-02-09

[2] Uddeholm ELMAX SuperClean porkohászati szerszámacél adatlapja.

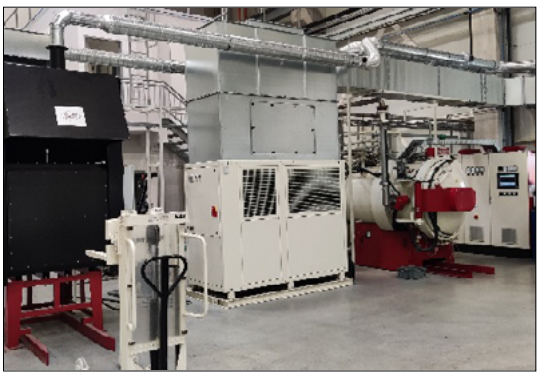

Fig. 2. *Heat treatment facility of Titán 94 Ltd.*

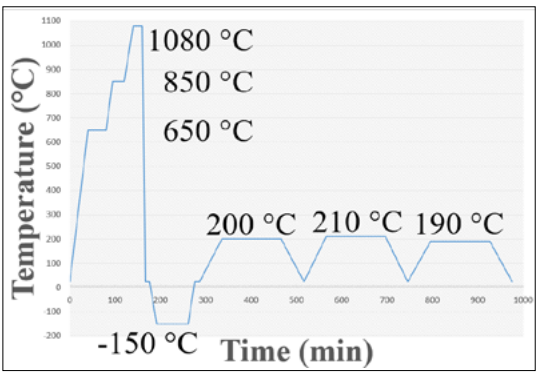

Fig. 3. *Heat treatment diagram of the cryogenically treated specimens.*

https://www.uddeholm.com/app/uploads/sites/216/productdb/api/tech_uddeholm-elmax_en.pdf (letöltve: 2025. május 7.).

[3] Különböző acélok összehasonlítása Tóth László késkészítő szemszögéből https://vadaszkes.eu/az-acelokrol/ (letöltve: 2025. május 7.).

[4] Kovács T., Dévényi L.: *Kopásvizsgálati eljárás fejlesztése.* Anyagok Világa, V/1. (2004) http://anyagokvilaga.hu/tartalom/2004/dec/05_KT_DL.pdf (accessed on: mai 7. 2025).

[5] ASTM G31-21: Standard Guide for Laboratory Immersion Corrosion Testing of Metals, 2021. https://store.astm.org/g0031-21.html (accessed on: april. 10., 2025.).

[6] ASTM G1-03(2017)e1: Standard Practice for Preparing, Cleaning, and Evaluating Corrosion Test Specimens, 2017. https://store.astm.org/g0001-03r17e01.html (accessed on: 2025. apr. 10.).

[7] Bourithis L., Papadimitriou G. D., Sideris J.: *Comarison of wear properties of tool steels AISI D2 and O1 with the same hardness.* Tribology International, 39/6. (2006) 479–489. https://www.sciencedirect.com/science/article/abs/pii/S0301679X05000873

[8] Tóth L., Haraszti F., Kovács T.: *Heat Treatment Effect for Stainless Steel Corrosion Resistance.* European Journal of Materials Science and Engineering, 3/2. (2018) 38–42. https://www.researchgate.net/publication/329625016_HEAT_TREATMENT_EFFECT%20_FOR_STAINLESS_STEEL_CORROSION_RESISTANCE

Acta Materialia Transylvanica 8/2. (2025) 70–73.
DOI: Hungarian: https://doi.org/10.33923/amt-2025-02-05
English: https://doi.org/10.33924/amt-2025-02-05

Explosive Surface hardening of the Austenitic Steel

Tünde Anna KOVÁCS

Óbuda University, Bánki Donát Faculty of MEchanical and Safety Engineerig, Budapest, Hungary, kovacs.tunde@bgk.uni-obuda.hu

Abstract

The research focuses on the presentation and analysis of explosive welding and hardening processes. In practice, the direct method is used for explosive hardening, in which the explosive is placed on the surface of the metal to be hardened. The indirect method is not yet common in practice. In the indirect process, similar to explosive cladding, there is a gap between the explosive and the surface of the metal to be hardened. We conducted experiments on two different steel grades (X120Mn12, X5CrNi1810) using the same quantity and quality of explosive. Following direct and indirect hardening, the hardness measurement results showed that the hardness achievable with direct hardening (238 HV for X120Mn12, 263 HV for X5CrNi1810) was lower than that achieved by indirect hardening (472 HV for X120Mn12, 322 HV for X5CrNi1810) using a 1.5 mm gap distance.

Keywords: *explosive welding, plastic deformation, dislocation, cohesive bonding.*

1. Introduction

Explosive forming and welding technologies began to be developed and applied after World War I. The physical basis of the technology is the plastic deformation effect, which is aided by the heat generated by friction caused by deformation in the crystal structure of the metal [1]. The high-pressure gas shock wave generated from the explosion can join the metal surfaces at high speed during explosive welding. The forming speed in this case differs significantly from the forming speed used in cold metal forming. The deformation caused by the explosion is a high-speed dynamic effect that causes deformation and phase transformation in the face centered cubic crystal structure steels [1]. Typically, this process is used for austenitic Hadfield steel hardening, as this type of steel is prone to work hardening through phase transformation. The austenitic microstructure steel phase transformation can also be observed as a result of cold working, Strain-Induced Martensitic Transformation (SIMT). In practice this hardening process is not used in the case of the austenitic stainless steels.

The shock wave established by the explosion causes an increase in hardness of metals, but the parameters of this phenomenon have not yet been fully described in scientific terms. The analysis of the effect of deformation rate on the γ-α' transformation in austenitic steel has long been a subject of interest to researchers. Early studies simply noted that as the explosion pulse duration (Δt) increased, the amount of martensite also increased and the hardness of the steel increased (Fig. 1) [2].

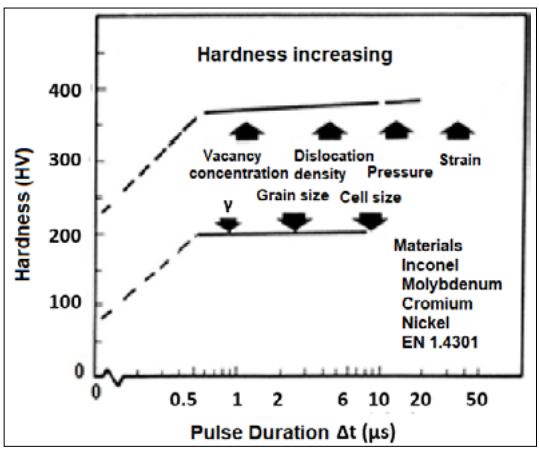

Fig. 1. *Hardening as a function on the explosion impulse time.* [2]

The traditional hardening mechanism of Hadfield steel mainly involves dislocation, twinning, and dynamic deformation ageing [3]. Although explosion-hardened Hadfield steel frogs are widely used on railways around the world, the deformation mechanism that occurs during the explosion hardening of this steel is not yet fulyly understood [4]. The explosive hardening of Hadfield steel railroad frogs is a widely used technology worldwide that allows for increasing the surface and subsurface hardness of crossings [2, 4, 5]. Fig. 2 shows a typical application of a casted Hadfield steel at the tip of a railroad frog

References in the literature indicate that, as a result of plastic deformation caused by high-speed forming, Hadfield steel undergoes Strain-Induced transformation triggered by deformation, and γ austenite transforms into α ferrite or ε martensite. It has been shown that the transformation from γ austenite to ε martensite depends on the deformation rate [6]. Explosive hardening technology can also increase the hardness and wear resistance of ausustenitic stainless steel [7, 8]. Austenitic stainless steel has high formability, low hardness, and very good corrosion resistance. Heat treatment cannot be used to increase its hardness. Of course, there are stainless steels that can be hardened exceptionally well, but their chemical composition differs from that of the widely used austenitic stainless steels [9, 10].

2. Explosive machining technologies

2.1. Explosive cladding process

The purpose of explosive bonding technology is to join metals together using high-speed deformation caused by an explosion. Due to the cohesive bond that forms, this process is considered to be welding [10]. Metals do not typically melt because there is no heating during the process; the heat is generated only by the deformation and the explosion, this process belongs to the group of cold welding processes. The material science basis of the process is the deformation that occurs as a result of high-speed forming, during which the atoms of the materials being joined form bonds with each other without mixing. This process is typically used in practice for joining large surfaces, such as flat plates. This process can be used to weld together a number of different metals that cannot be welded together using fusion welding (e.g., steel and titanium) [11, 12]. In the case of the explosive welding process specification, there is the need to take account of the selection of the explosive. When selecting explosives, the critical limit value for the explosive's detonation velocity must be taken into account. The speed of sound in the material must be lower than the collision speed of the cover plate and the base plate [13, 14]. The amount of the selected explosive can be determined based on the thickness and density of the cover plate. In the case of the large plates explosive welding, the base plate and the cladding plate are placed parallel to each other, leaving a gap between them calculated from the thickness of the cover plate. The parallel setup is shown in Fig. 3.

According to empirical recommendations, the gap distance should be between 0.5 and 1.6 times the thickness of the cladding plate, which is an empirical value. The gap distance is the distance that the cover plate travels before collission with the base plate. If this distance is too large, the plates may be damaged during impact and a significant increasing in the hardness may be observed. If the distance is too small, the surfaces of the plates will not bond properly [7].

The cross-section of the explosively welded joint in the direction of the explosion is the wave line following the shock wave of the explosion. The

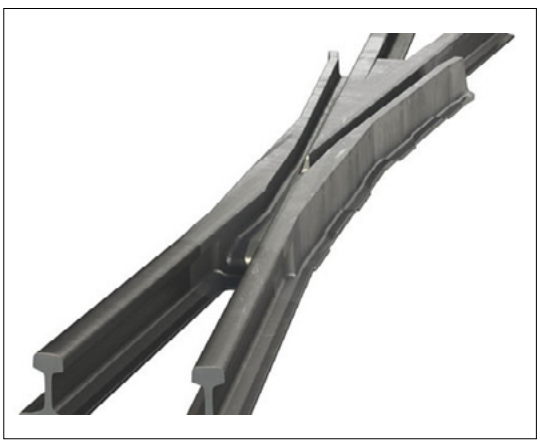

Fig. 2. *Austenitic manganese steel railway frog.*

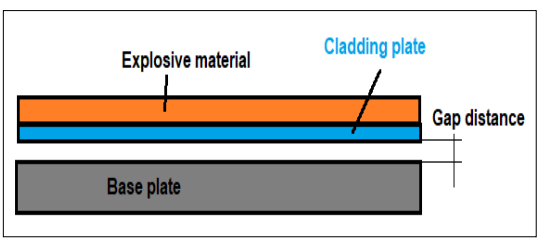

Fig. 3. *Paralell setup of the explosive welding.*

hardness on both sides of the joint increases compared to the hardness of the base metal. This can be considered the heat and deformation zone of the weld, which is a very narrow range (1-2 mm). The degree of hardening depends on the parameters of explosive cladding and the hardening coefficient of the materials used, i.e. their material characteristics.

2.2. Explosive hardening process

Explosive hardening technology is similar to explosive cladding technology in that it uses shock waves from high-pressure gas generated by explosions to increase the hardness of metal surfaces caused by plastic deformation. Different metals exhibit varying work hardening depending on their material properties. Hardness also depends on the used hardening technology. In the traditional setup, the explosive is placed directly on the metal surface for the explosive hardening process(direct hardening), while in the new setup it needs to left a gap between the metal surface and the explosive according to the explosive cladding setup (indirect hardening).

For the indirect hardening process, we used 319 g of Permont 10T explosive powder. The indirect hardening setup, which is identical to the explosive welding setup (**Fig. 3**), had a gap distance of 1.5 mm. Direct hardening was performed using the same explosive material and quantity. After hardening, Vickers hardness was measured on the surface of the steel test specimens using a load of 1.2 kgf. The results are shown in **Table 1**.

Table 1. *Results of the direct and indirect hardening*

Material	Hardness HV		
	Base metal	Direct	Indirect
X120Mn12	110	238	472
X5CrNi18-10	215	263	322

The results clearly show that indirect hardening caused greater hardening in both steel grades than direct hardening.

3. Conclusions

The results obtained from literature research and explosive hardening are in harmony. Based on the experimental results, it can be concluded that the indirect explosive hardening process results in greater hardnening than the direct process with the same explosive quality and quantity for the same steel grades.

References

[1] Zhang M., Lv B., Zhang F., Feng X.: *Explosion Deformation and Hardening Behaviours of Hadfield Steel Crossing*. ISIJ International, 52/11. (2012) 2093–2095. https://doi.org/10.2355/isijinternational.52.2093

[2] Meyers M. A., Murr L. E.: *Shock Waves and High-Strain-Rate Phenomena in Metals*. International Conference on Metallurgical Effects of High-Strain-Rate Deformation and Fabrication, Albuquerque, N.M., 1980. 91–111.

[3] Davis J. R.: *Surface Hardening of Steels*. ASM International, (2002) 1–16.

[4] Havlícek Petr, Busóvá Katerina: *Experience with explosive hardening of railway frogs from Hadfield steel*. Metal, Brno, Czech Republic, 2012.

[5] Völgyi B., Kovács-Coskun T., Sikari-Nágl I.: *Hadfield acél keménységváltozása robbantásos alakítás hatására*. In: FMTÜ XVIII. Nemzetközi Tudományos Konferencia, Kolozsvár, Erdélyi Múzeum-Egyesület, (2013) 449–452. https://doi.org/10.36243/fmtu-2013.99

[6] Lee Sang Hun, Choi Jeom Yong, Nam Won Jong: *Hardening Behavior of a 304 Stainless Steel Containing Deformation-Induced Martensite during Static Strain Aging*. Materials Transactions, 50/4. (2009) 926–929. https://doi.org/10.2320/matertrans.MRP2008416

[7] Staudhammer K. P., Frantz C. E., Hecker S. S., Murr L. E.: *Effects of Strain Rate on Deformation-Induced Martensite in 304 Stainless Steel*. In: Meyers M. A., Murr L. E. (eds.): *Shock Waves and High Strain Rate Phenomena in Metals*. Plenum, New York, 1981. 91–112.

[8] Haraszti F., Kovács T.: *Plastic deformation effect of the corrosion resistance in case of austenitic stainless steel*. IOP Conference Series: Materials Science and Engineering, 175. 2017. https://doi.org/10.1088/1757-899X/175/1/012048

[9] Kovács T., Kuzsella L.: *High Energy Rate Forming Induced Phase Transition in Austenitic Steel*. Journal of Physics-Conference Series 790. (2017) 012039.

[10] Findik F.: *Recent developments in explosive welding*. Material&Design, 32/3. 1081–1093.

[11] Holtzman A. H., Cowan G. R.: *Bonding of metal with explosives*. Welding Research Council Bulletin, New York, 1965. 1–21. https://doi.org/10.1016/j.matdes.2010.10.017

[12] Pocalyko A.: *Metallic Coatings (Explosively Clad)*. Encyclopedia of Chemical Technology, Vol. 15. Third edition, 275–296.

[13] Kugyela L., Daruka N., Kovács T. A.: *Explosive Welding of Metals for Electronic Applications in The Impact of the Energy Dependency on Critical Infrastructure Protection*. Advanced Sciences and Technologies for Security Applications, 2024. https://doi.org/10.1007/978-3-031-78544-3_35

[14] Lukács L., Szalay A., Zádor I.: *Explosive forming and aerospace.* Aeronautical Science Bullettins, XXIV/2. (2012) 431–446.

Acta Materialia Transylvanica 8/2. (2025) 74–80.
DOI: Hungarian: https://doi.org/10.33923/amt-2025-02-06
English: https://doi.org/10.33924/amt-2025-02-06

Consequences of the Asymmetric Cutting of S355 Steel Grade when Using Acetylene and Hydrogen Combustible Gases

János KUTI,[1] Péter PATÓ,[2] Enikő Réka FÁBIÁN,[3] Andrea SZABÓ[4]

[1] *Óbuda University, Doctoral School on Materials Sciences and Technologies, Budapest, Hungary, kuti.janos@bgk.uni-obuda.hu*

[2] *Óbuda University, Bánki Donát Faculty of Mechanical and Safety Engineering, Institute for Natural Sciences and Basic Subjects. Budapest, Hungary, pato.peter@bgk.uni-obuda.hu*

[3] *Óbuda University, Bánki Donát Faculty of Mechanical and Safety Engineering, Institute of Materials and Manufacturing Sciences, Department of Material Technology. Budapest, Hungary, fabian.reka@bgk.uni-obuda.hu*

[4] *University of Dunaújváros., Technical Institute, Dunaújváros, Magyarország, szaboandrea@uniduna.hu*

Abstract

In this research, flame cutting experiments were performed on 35 mm thick S355JR steel plates using acetylene and hydrogen. During our tests, we cut the pieces so that we ended up with one much larger piece and one smaller piece. Changes in the microstructure and hardness were studied, according to the size of the pieces and the cutting position, using the two different fuel gases. The heat flow of the smaller piece was measured using thermocouples.

Keywords: *flame cutting, non-alloy structural steels..*

1. Introduction

The S355JR is a non-alloy, structural steel grade defined in the EN 10025-2:2020 standard. The S355 grade belongs to the group of structural steels; as indicated by its designation (“S”), while the number denotes the minimum yield strength. Accordingly, its minimum yield strength is 355 MPa up to a plate thickness of 16 mm. As the thickness increases, the yield strength decreases progressively; in the case of the 35 mm thick plate used for the experiments in this study, the minimum yield strength is 335 MPa.

The suffix “JR” specifies the steel’s toughness determined by the Charpy impact test at a defined temperature at which the material exhibits a minimum impact energy of 27 J. In this case, the specified test temperature is +20 °C. From a chemical composition perspective, S355 JR is a non-alloy, low-carbon steel. Its carbon equivalent is approximately 0.45 [1, 2].

During flame cutting, the fuel gas mixed with oxygen is burned in a high-pressure oxygen jet, heating the material to its ignition temperature (preheating), while simultaneously blowing away the resulting molten combustion products with the oxygen jet. The conditions for the applicability of flame cutting are that: the material must be combustible in oxygen; the ignition temperature of the material must be lower than its melting point; the melting point of the oxide formed from the material is also lower than its melting point, so that the combustion products can be brought to a molten state and easily removed from the cutting gap; the combustion heat (heat of oxidation) of the material should be high and its thermal conductivity low so that the cutting gap forms quickly and remains narrow.. In industrial practice, these flame cutting requirements are only applied to unalloyed and low-alloy structural steels and cast steel. Although the ignition point of unalloyed steels remains below the melting point of the material up to a carbon content of nearly 2%, they can typically be cut very efficiently with a flame up to a carbon content of 0.25% [3, 4].

Low-carbon (C < 0.25%), unalloyed, and mildly alloyed structural steels are used in large quantities for the manufacture of welded structures, and this trend is expected to grow significantly in the

coming years [5]. The most commonly used combustible gas for flame cutting is acetylene (C_2H_2), but hydrogen is also playing an increasingly important role due to environmental considerations [6, 7, 8].

2. Flame Cutting of Test Specimens

The flame cutting of the test specimens used in our research was carried out in the demonstration laboratory of Messer Hungarogas Ltd. For the investigations, we used S355JR steel with a 35 mm plate thickness, cut into 200 × 300 mm specimens. Two test plates were cut: one using acetylene as the fuel gas, and the other using hydrogen. During cutting, maintaining a uniform cutting speed was essential from several perspectives; this was ensured by a flame-cutting torch mounted on a mechanical cutting carriage (Fig. 1).

The dimensions of the plates used as test specimens are shown in Fig. 2. The hardness test specimens are numbered from 1 to 4; these numbers are used throughout the remainder of the paper to identify the individual samples. The cutting kerfs were initiated between samples 1 and 2 - smallest and largest part of cut pieces (sections with widths of 20 mm and 180 mm). The specimens taken from the plate cut with acetylene as the fuel gas are designated with the letter “A” preceding the number (test specimens A1, A2, A3, and A4), whereas those taken from the plate cut using hydrogen are identified with the prefix “H” (samples H1, H2, H3, and H4). (Fig. 3). All test specimens were extracted from the plates using waterjet cutting to avoid additional microstructural alterations. Hardness measurements were performed perpendicular to the flame-cut surface, as a function of the distance from the cut edge, following appropriate surface preparation.

Another important aspect during cutting is maintaining the appropriate gas flow rates, which were verified prior to the process using a flow meter Table 1 summarizes the key parameter values recorded during the cutting operation.

Table 1. *Set parameters at the flame-cutting process*

Parameter	Acetylene cutting	Hydrogen cutting
Cutting speed (mm/min)	520	520
Fuel gas flow rate (L/min)	1.6	1.2
Cutting oxygen flow rate (L/min)	5.1	5.1

Fig. 1. *Flame-cutting equipment used for preparing the test specimens.*

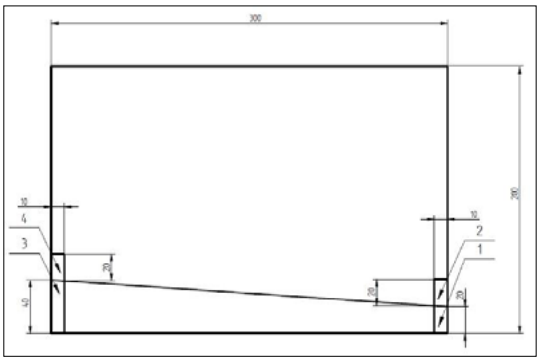

Fig. 2. *Layout of the test plate showing the cut edge and the positions of the test specimens.*

Fig. 3. *Photograph of the test specimen after cutting.*

3. Thermocouple measurements

Before cutting, thermocouples were inserted into the plates to enable continuous monitoring of the temperature during the process. The thermocouples were positioned along the side of the plate, near the cutting line, as illustrated in Fig. 4. As can be seen on Figure 4, the thermocouples are numbered from 1 to 8. The thermocouples

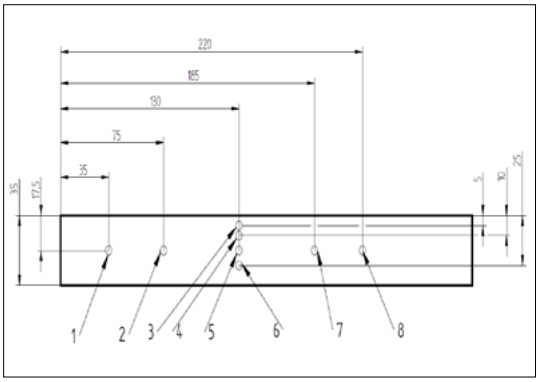

Fig. 4. *Position of the thermocouples along the side of the plate.*

numbered 1, 2, 5, 7, 8 were positioned in middle of plate thickness at 35 mm, 75 mm, 130 mm, 185 mm and 220 mm from the end of cut kerf. The thermocouples 3, 4, 5 and 6 were positioned at 170 mm from the beginning of cut kerf, at a different distance from the face of plate (5 mm, 10 mm, 17,5 mm and 25 mm). For easier identification when presenting the measurement results, the thermocouple numbers are prefixed with the letters “A” or “H”, corresponding to acetylene and hydrogen fuel gas usage, respectively (i.e., A1–A8 and H1–H8).

For the measurements, TC Direkt brand, Type K, stainless-steel sheathed thermocouples were used, with a diameter of 1 mm and a length of 300 mm. The thermocouples were placed in drilled holes at a depth of 18 mm inside the plate material, positioned so that their tips were in contact with the end of each borehole. The holes were drilled to a diameter of 3.5 mm down to 16 mm, followed by an additional 2 mm of drilling with a 1.1 mm diameter. This ensured stable positioning of the thermocouples within the bores.

For recording the data supplied by the thermocouples, a DATAQ DI-710-EH multi-channel Ethernet-based data acquisition unit for analog signals was used. The device operated with the manufacturer’s free software, WinDaq, which enabled exporting the results in tabular format.

4. Hardness measurement. Microscopy

In order to determine how fuel gas affects the microstructure of the cutting environment and how the size of the cut pieces affects the microstructure, the hardness on polished samples was measured and the microstructure after etching with nitric acid was examined.

The hardness measurements were carried out in the materials testing laboratory of the University of Dunaújváros. A Buehler Wilson UH4750 hardness tester was used to determine the hardness values. Establishing the accuracy and reliability of the hardness tester used for the measurements is essential to ensure that no false measurement results are obtained. For this purpose, a trial measurement was performed on a reference block with a certified hardness value of 388.6 HV10, allowing the accuracy of the measuring device to be verified. After completing the instrument setup, the trial measurement was performed.

The microstructure was examined using a Zeiss Axio Observer Z1M optical microscope.

5. Results

5.1. Results of the thermocouple measurements

The temperature of the plate and its changes (cooling) during cutting were evaluated based on the data recorded by the thermocouples. The results are illustrated in **Fig. 5** and **6.** shown separately for the measurements obtained during cutting with acetylene and hydrogen. **Fig. 5** shows the values recorded during cutting with acetylene, while **Fig. 6** shows the values measured when hydrogen was used as fuel gas.

The measurement results show that from the start of cutting to 80 mm, the maximum temperature did not reach 200°C for either cutting gas. The maximum temperatures recorded by the thermocouples barely exceeded 300°C for both cutting gases. The two types of cutting gas did not cause any difference at the measurement points.

Based on these results, it is evident that the two plates reached nearly identical temperatures at the measurement points when using the two different fuel gases, and their temperature changes over time were also similar. The reasons for the differences observed in the resulting microstructural changes are discussed in the following subsections.

5.2. Results of the Hardness Measurements

The hardness measurements were performed using the Vickers method with a test load of 98.81 N. Each test specimen was measured at 10 positions, depending on the distance from the cut edge. The hardness measurements were taken at distances of 1, 2, 3, 4, 5, 7, 9, and 15 mm from the cut edge (**Table 2.** and **3.**).

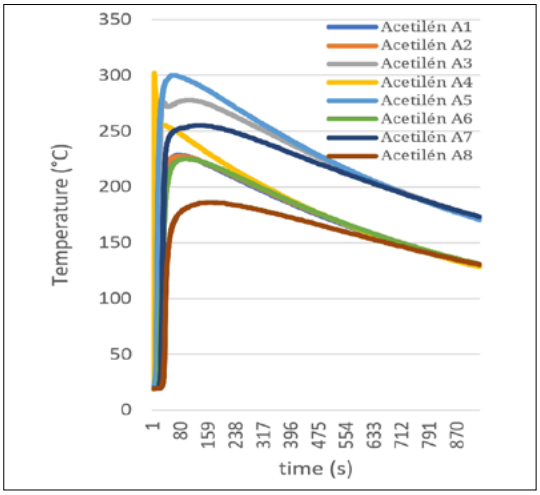

Fig. 5. *Cooling curves for acetylene cutting.*

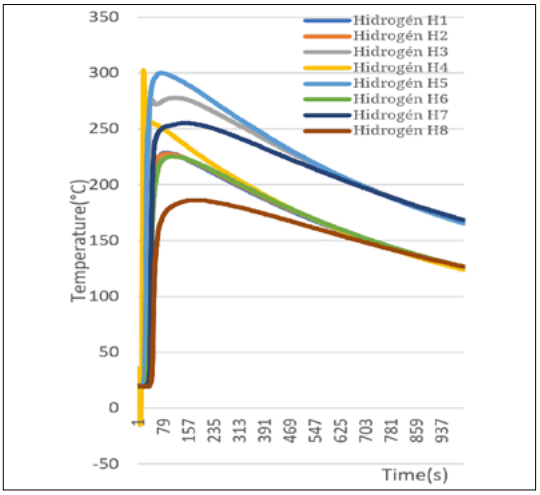

Fig. 6. *Cooling curves for hydrogen cutting*

Table 2. *Hardness values measured on the test specimens cut using acetylene as the fuel gas, as a function of distance from the cut edge*

Distance from flame cut edge (mm)	Hardness (HV10)			
	A1	A2	A3	A4
1	327.3	258.1	170.2	463.5
2	153.1	243.4	151.3	292.0
3	163.2	198.0	144.7	188.0
4	166.2	186.8	145.5	166.2
5	165.2	181.1	145.5	173.4
7	162.3	161.3	142.3	170.2
9	162.3	160.4	123.8	167.2
15	153.1	156.7	138.4	166.2

Table 3. *A hidrogén éghető gáz felhasználásával vágott próbatesteken mért keménységértékek a távolság függvényében*

Distance from flame cut edge (mm)	Hardness (HV10)			
	H1	H2	H3	H4
1	192.9	158.5	163.2	314.0
2	172.3	148.8	151.3	179.8
3	143.1	134.7	151.3	173.4
4	146.3	133.3	143.1	177.7
5	143.9	136.2	139.9	158.5
7	163.2	133.3	139.9	154.9
9	163.2	137.7	143.1	158.5
15	149.6	136.9	143.1	158.5

To compare the fuel gases used for cutting, it is necessary to evaluate the hardness values of selected test specimens against each other. This allows the differences in microstructural changes resulting from the use of different gases to be determined. The following figures present these comparisons separately. The hardness values measured on test specimens of identical positions—but cut using different fuel gases—were compared as a function of the distance from the cut edge.

From Fig. 7–10, it can be observed that at the beginning of the cut, contrary to our expectations, the specimens with smaller mass and volume (samples numbered 1) exhibited higher hardness values. Initially, we assumed that the specimens with larger mass and volume would extract more heat, and therefore specimens 2 and 4 would develop higher hardness.

Specimen 4 shows higher hardness values near the cut edge—both for acetylene and hydrogen cutting—compared to specimen 3. This is due to the larger material mass located behind specimen 4, which extracts more heat from the cutting process. As a result, greater heat removal occurred there, leading to lower heating of those specimens.

For specimen 1, assuming that heat was transferred symmetrically into the two adjacent pieces, the smaller specimen received the same amount of heat input despite its lower mass. Consequently, it remained at elevated temperatures for a longer period. This allowed more extensive austenite formation and resulted in larger grain

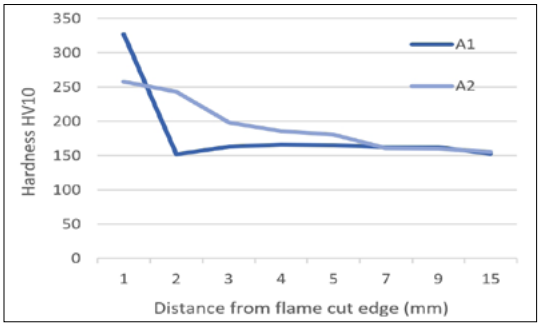

Fig. 7. *Comparison of hardness values measured on test specimens A1 and A2.*

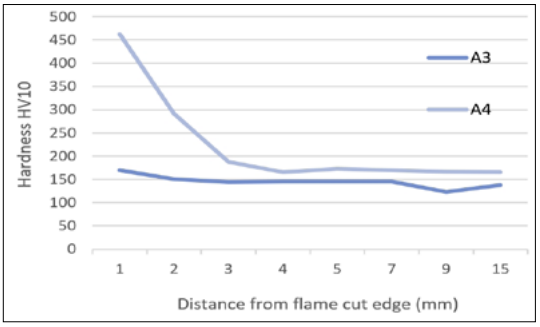

Fig. 8. *Comparison of hardness values measured on test specimens A3 and A4.*

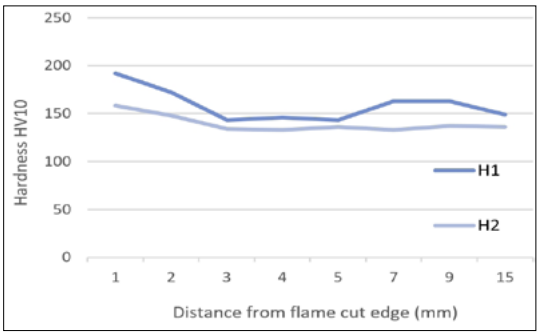

Fig. 9. *Comparison of hardness values measured on test specimens H1 and H2.*

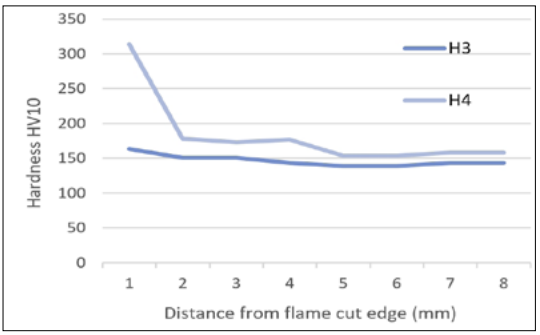

Fig. 10. *Comparison of hardness values measured on test specimens H3 and H4.*

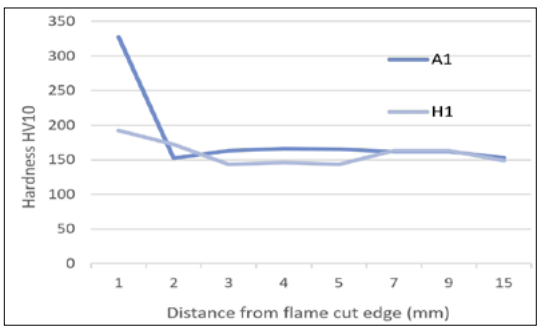

Fig. 11. *Comparison of hardness values measured on test specimens A1 and H1.*

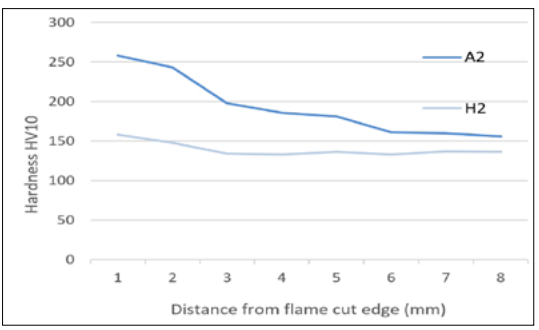

Fig. 12. *Comparison of hardness values measured on test specimens A2 and H2.*

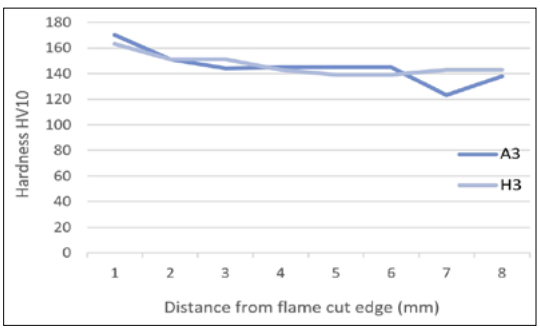

Fig. 13. *Comparison of hardness values measured on test specimens A3 and H3.*

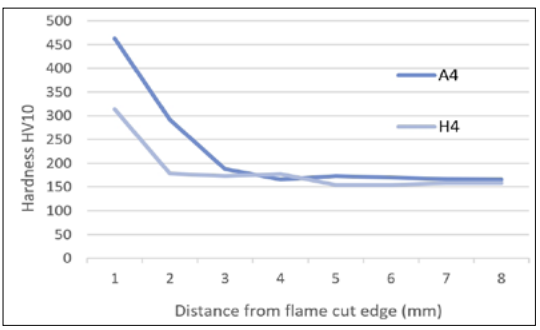

Fig. 14. *Comparison of hardness values measured on test specimens A4 and H4.*

sizes. Both effects promote the formation of martensite [9, 10].

From Fig. 11. and 12, it can be observed that at the beginning of the cut, the hardness values are significantly higher when acetylene is used compared to hydrogen. In Fig. 13 and 14, at the end of the cut, it can be seen that for the smaller specimen, both hydrogen and acetylene preheated the material prior to cutting. Due to the accumulated thermal energy, the resulting hardness values are nearly identical. For the larger specimen, however, the higher flame temperature of acetylene becomes more pronounced.

Based on hardness measurements, it can be concluded that in both acetylene and hydrogen cutting, the hardness of the 35 mm plate is practically the same as that of the base material when measured 6 mm from the cutting surface, but using hydrogen as fuel gas the heat affected zone is under 3 mm. This measurement is consistent with the results observed in high energy density cutting [11].

5.3. Metallographically studies results

Fig. 15 shows the basic microstructure of the plate material. The ferrite and pearlite bands formed as a result of rolling are clearly visible. Due to the rapid heating and cooling that occurs during cutting, the bands behave differently if they do not have time to homogenize.

Fig. 16. shows the microstructure of the A4 test specimen. The transitional microstructure of this test specimen can be seen on the base metal side, at the beginning of the heat-affected zone. It is noticeable that the base metal pearlite has been transformed. The originally pearlitic bands have been transformed into bainite and martensite.

Fig. 17. shows the microstructure of test specimen H1 near the cutting edge. Homogenization occurred only in the immediate vicinity of the cutting edge, but the microstructure in the heat-affected zone is neither ferritic nor pearlitic.

A higher resolution had to be used to determine the microstructure formed in the heat-affected zone.

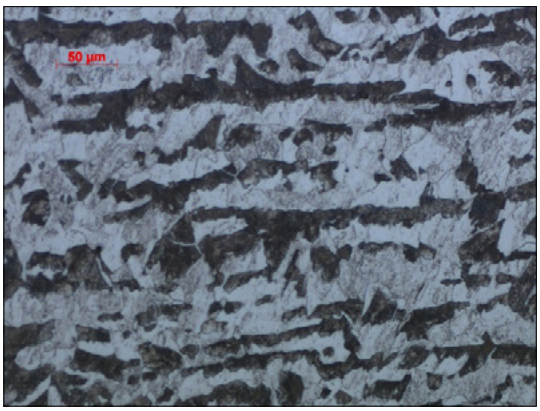

Fig. 15. *Base microstructure of the plate.*

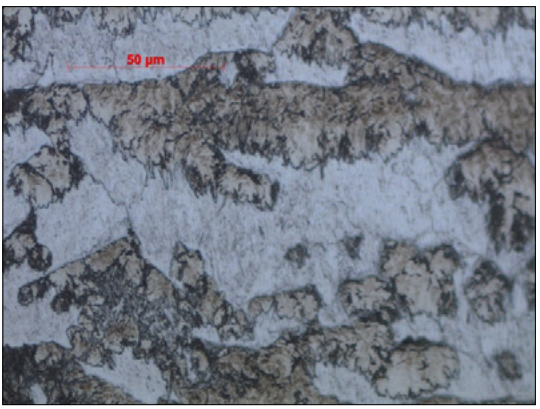

Fig. 16. *Heat-affected zone of specimen A4.*

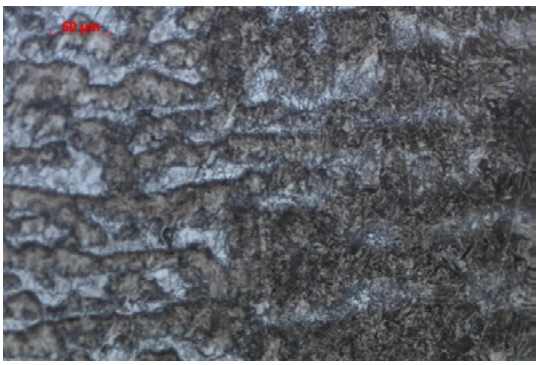

Fig. 17. *Transitional microstructure of specimen H1 adjacent to the cut zone.*

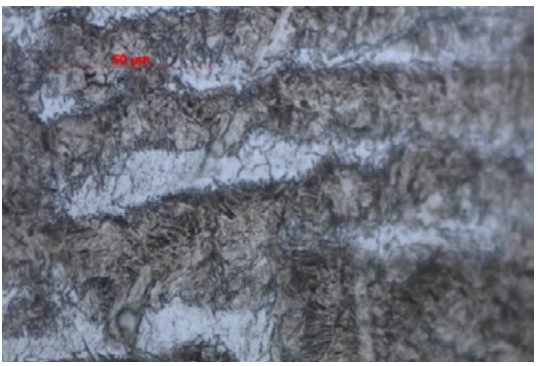

Fig. 18. *Heat-affected zone and microstructural boundary at the cut edge of specimen H1.*

Fig. 18. shows the heat-affected zone of sample H1. The original pearlite rows were transformed into martensite and bainite, and some carbide particles also appeared in the ferrite rows, but they remained essentially ferrite.

6. Conclusions

In this study, flame cutting with hydrogen and acetylene as fuel gases was compared using S355JR steel. At the beginning of the cut, contrary to our expectations, the specimens with smaller mass and volume (samples numbered 1) exhibited higher hardness values

However, according to the thermocouple measurements in the present experiments, this trend did not occur. Instead, the higher flame power and flame temperature of acetylene had a dominant influence on the resulting microstructural transformations.

References

[1] Meadinfo – Material properties of S355 steel. https://meadinfo.org/2015/08/s355-steel-properties.html

[2] Gáti J.: *Hegesztési zsebkönyv,*. Cokom Mérnökiroda Kft., Miskolc, 2003. 42–45.

[3] Bitay E.: *Hegesztési alapismeretek.* Erdélyi Múzeum-Egyesület, Kolozsvár, 2021. 87–89.

[4] Gáti J.: *Hegesztési Zsebkönyv I. Hegesztési eljárások.* Cokom Mérnökiroda Kft., Budapest, 2023. 151–158.

[5] Market Research Report, 2025. https://www.fortunebusinessinsights. com/industry-reports/welding-market-101657 (letöltve: 2025. december 16.)

[6] Hamzah A.: *Development of welding technology in the future: analysis of trends and impacts on industry and the environment.* Collaborate Eng. Daily Book Series 1. (2023) 100–106.

[7] Mehrifar Y., Zamanian Z., Pirami H.: *Respiratory exposure to toxic gases and metal fumes produced by welding processes and pulmonary function tests.* International Journal of Occupational Medicine and Environmental Health, 10/1. (2019) 40–49. https://doi.org/10.15171/ijoem.2019.1540.

[8] Suban M., Tusek J., Uran M.: *Use of hydrogen in welding engineering in former times and today.* Journal of Materials Processing Technology, 119/1–3. (2001) 193–198. https://doi.org/10.1016/s0924-0136(01)00956-6.

[9] Tisza Miklós: *Anyagvizsgálat*. Miskolci Egyetemi Kiadó, Miskolc, 2010.

[10] Callister William D., Rethwisch David G.: *Materials Science and Engineering.* John Wiley & Sons, Hoboken, New Jersey, USA, 2018.

[11] Diekhoff P., Sun J., Nitschke-Pagel T. et al.: *A comparative study of the thermal and mechanical cutting influence on the cut-edge hardness of structural steels S355 and S1100.* International Journal of Advanced Manufacturing Technology, 130. (2024) 5951–5964. https://doi.org/10.1007/s00170-023-12937-2

Acta Materialia Transylvanica 8/2. (2025) 81–87.
DOI: Hungarian: https://doi.org/10.33923/amt-2025-02-07
English: https://doi.org/10.33924/amt-2025-02-07

Investigation of the Handheld Laser Welding Parameters

Balázs Ákos NAGY,[1] Kíra KOVÁCS,[2] Tünde Anna KOVÁCS[3]

[1] *Óbuda University, Bánki Donát Faculty of MEchanical and Safety Engineerig, Budapest, Hungary, nagy.balazs@bgk.uni-obuda.hu*

[2] *Óbuda University, Bánki Donát Faculty of MEchanical and Safety Engineerig, Budapest, Hungary, kira.kovacs3@gmail.com*

[3] *Óbuda University, Bánki Donát Faculty of MEchanical and Safety Engineerig, Budapest, Hungary, kovacs.tunde@bgk.uni-obuda.hu*

Abstract

High-performance handheld laser welding technologies have undergone significant advancements in recent years, particularly with the emergence of compact, cooled, and precise beam-shaping equipment. Handheld lasers (HL) possess all the advantages of their industrially applied, machine- or robotic-arm-guided counterparts. The key distinction lies in numerical beam control, which, alongside the parameters critical for successful welding, receives particular attention. This was due to the material- and penetration-depth-dependent program code table of the user-friendly Lightweld 1500 XT fiber laser welding equipment. During the experiments, S355 structural steel and DC01 cold-rolled steel sheets were welded in a T-joint configuration with varying sheet thicknesses, using identical material pairings. The used filler material was a Böhler EMK 8 Ø1 mm solid wire electrode, and the shielding gas was nitrogen with a 4.6. purity. We found that even with the settings recommended by the welding machine manufacturer, there were welding deviations, which suggests that the quality of manual welding also depends on the skill of the welder.

Keywords: *handheld laser welding, conduction laser welding, welding speed, filler material, nitride precipitations.*

1. Introduction

Fig. 1 shows the weld shapes typically created during laser welding.

Laser technologies are indispensable in our daily lives, particularly in industrial applications. This is especially true in welding technologies due to their precision, high power density, and relatively low thermal load on the base material **[1, 2, 3]**. Until recently, robust equipment has typically been used, referring to the excitation circuit and isolated workspaces. Thanks to advancements in fiber technology, excitation circuits can now be designed to match the size of industrial wire electrode (code: 13) or tungsten electrode (code: 14) shielded arc welding machines **[4]**. This has led to the development of handheld laser sources, which gained significant attention in the late 2000s (according to General Electronics Co.'s patent) **[4, 5]**. These first-generation laser sources did not yet possess the compact dimensions mentioned earlier, but current fourth-generation models, with advancements in cooling systems, have achieved this **[4, 6]**.

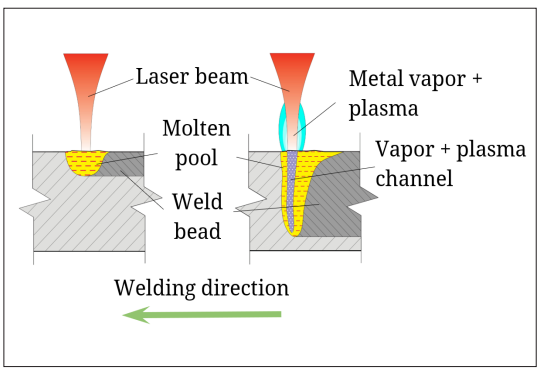

Fig. 1. *Difference between heat conduction (left) and deep-penetration (right) laser welding.*

The standard Welding and Allied Processes (MSZ ISO 4063: 2023) assigns identification codes to various processes, distinguishing between manual and automated variants of technologies operating on the same principles. Handheld laser welding lacks a specific designation but can be defined under code 521, which indicates high-energy-density (5), laser-based (2), and specifically solid-state (1) systems [7]. Key characteristics of this process include the use of Nd: YAG crystal ($Y_3Al_5O_{12}$/YAG: yttrium-aluminum-garnet doped with Nd^{3+} ions) as the typical laser medium, with an emission wavelength of 1064 nm (Near Infrared - NIR) [1, 2, 8]. Additionally, it operates in continuous wave (CW) mode, and due to variations in welding speed, it is limited to conduction welding during manual beam guidance.

At the end of the article, we evaluate the performance of the default programs of the IPG LightWeld 1500 XT laser equipment, courtesy of Intertechnika Ltd.

2. Parameters of Laser welding

To achieve a high-quality weld, it is essential to define and control the input parameters [3].]. The process begins with determining the weld geometry and the required material thickness, as these dictate the other adjustable parameters [9]. Parameters that can be controlled include the power setting on the equipment (potentially including beam oscillation), the gas flow rate on the shielding gas regulator, and the relative positioning of the workpieces using auxiliary tools (clamps, fixtures, welding table-template systems) or tack welding [3, 9]. Challenges with this process include maintaining a constant welding speed and ensuring the correct focus position and distance [6].

2.1. Laser Power

The laser output power (W, kW) determines the energy delivered to the base material, which influences the penetration depth [2].

Estimating the power requirement is common practice, as it depends on multiple factors. A simplified approach is based on energy density [10]:

$$I = \frac{P}{A} = \frac{4 \cdot P}{{d_{spot}}^2 \cdot \pi} \quad (1)$$

where:
I: energy density (W/cm^2),
P: laser power (W),
A: irradiated area (cm^2),
d_{spot}: spot diameter (cm).

The approach is applicable since we know the energy density range for conduction welding (10^4-10^6 W/cm^2); however, it must be noted that the formula neglects several factors. The following formula approximates based on the absorbed energy (Q_a; J) [1]:

$$\begin{aligned} Q_a &= Q_1 + Q_2 + Q_3 + Q_4 + Q_l = \\ &= m_a \cdot c_p \cdot \Delta T_m + m_a \cdot L_m + \\ &\quad + m_a \cdot c_p \cdot \Delta T_V + m_a \cdot L_V + Q_l \end{aligned} \quad (2)$$

where:
Q_1: energy required to heat the base material to its melting point,
Q_2: energy for melting, which requires latent heat,
Q_3: energy required to vaporize the molten material,
Q_4: energy demand for vaporization as a function of the latent heat of vaporization,
Q_l: energy lost through conduction, convection, evaporation, reflection, and radiation,
m_a: mass of the melted material (kg),
c_p : specific heat capacity (J/kg·K),
ΔT_m: temperature difference required for melting the base material (K),
L_m: latent heat of melting (J/kg),
ΔT_V: temperature difference required for the molten material to reach its boiling point (K),
L_V: latent heat of vaporization (J/kg).

Taking into account the volume (V) and density (ρ), the following formula is obtained **[1]**:

$$Q_a = \rho \cdot V \cdot \left(c_p \cdot \Delta T_m + L_m + c_p \cdot \Delta T_V + \cdot L_V\right) \quad (3)$$

With this, the absorbed energy has been determined. To obtain the power, it must be divided by the time required to melt the base material. If tack welding is not performed, the time can be determined using the formula:

$$t = \frac{\Delta x}{v} \quad (4)$$

where Δx is the melted length (mm), and v is the welding speed (mm/s). Accordingly, the power calculation is:

$$P = \frac{Q_a \cdot v}{\Delta x} \quad (5)$$

During manual beam guidance, the welding speed is difficult to determine and maintain at a constant value. Therefore, the approach based on the melting energy requirement is:

$$P = \rho \cdot \dot{V} \cdot \left(c_p \cdot \Delta T_m + L_m + c_p \cdot \Delta T_V + \cdot L_V\right) \quad (6)$$

where:

$\dot{V}$: the volume of molten material per unit time (m^3/s).

2.2. Welding Speed

Welding speed (feed rate) is one of the most critical process parameters during welding, as it directly affects the penetration depth, weld geometry, and the extent of the heat-affected zone (HAZ) [3, 9]. Increasing the speed reduces the specific heat input, resulting in a smaller molten pool and shallower penetration, while a lower speed leads to deeper penetration and a wider weld profile [3, 9].

The relationships discussed in the previous section were based on the Rosenthal equation, which can be rearranged to express the welding speed. Another approach is illustrated in Fig. 2, which outlines the interaction between three parameters: power (P), relative speed (v_r) and beam spot diameter (d_f) [11].

The ratios formed between these parameters yield physically meaningful and interpretable quantities. These ratios include power density (p; W/mm^2), specific heat input (q; W/mm), and the „residence time of a surface material point in the focus spot" (t_h; s) [11]. Power density indicates how concentrated the laser power is per unit area. Therefore, the denominator must be adjusted with a focus geometry factor (Y; –): for a square spot, Y = 1, while for a circular cross-section (more common), Y = π/4 (1). The specific heat input (line energy) reflects the heat energy delivered per 1 mm of length. This allows us to predict the outcome: at low P/vr, shallower penetration is observed, followed by faster cooling, resulting in a martensitic microstructure (in carbon steels), which increases the risk of cracking [10]. It is advisable to maintain this ratio at a higher value to achieve a proper weld. The interaction time is related to this: the longer energy is delivered to a given material point, the higher its temperature rises, reducing the cooling rate and resulting in a martensite-free microstructure.

From the above calculations, further deductions can be made: the surface energy density („planimetric energy input," e; J/mm^2), volumetric energy density („volumetric energy input," e'; J/mm^3), and unit efficiency (e*; J/mm2 ·√s) can be determined. Surface energy density represents the energy delivered per unit area, while volumetric energy density projects this onto a unit volume. The unit efficiency (bottom part of (Fig. 2), is derived from weighting the formulas for power density and surface energy density, describing the efficiency of energy transfer to the workpiece for a given input power [11].

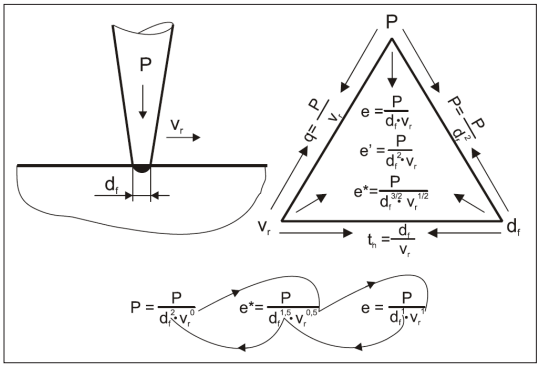

Fig. 2. *Parameter Relationships of High Energy Density Technologies* [11].

2.2.1. Welding Speed with Filler Material

During welding without filler material, the energy of the applied heat source is used to melt the base material. When a filler material is used, additional power is required to melt it [12]:

$$P_{extra} = \dot{m} \cdot \Delta T \cdot c + \dot{m} \cdot L_f \quad (7)$$

where:

$\dot{m}$: wire mass flow rate (g/s),

ΔT: temperature difference between the wire and its melting point (K),

c : specific heat capacity of the filler material (J/(g·K)),

L_f : specific latent heat of melting for steel (J/g)

From this formula, one unknown remains: the wire mass flow rate, which can be calculated as follows [13]:

$$\dot{m} = \rho \cdot A_{huzal} \cdot v_w \quad (8)$$

where:

ρ : density [g/cm^3],

A_{huzal} : wire cross-sectional area [mm^2],

v_w : wire feed speed [mm/s],

Based on this, the additional power requirement can be determined from the energy balance [1], thus the modified welding speed is:

$$v_{új} = v_{alap} \cdot \frac{P_{alap}}{P_{alap} + P_{extra}} \quad (9)$$

2.3. Heat Input

The heat input can also be expressed using the Rosenthal equation and the approach by Bagyinszki and Bitay. The heat input plays a

crucial role in covered arc welding, and the EN 1011-1 standard provides an example for its estimation. A similar formula is applied for laser processing [10]:

$$Q = \frac{\eta \cdot P}{v} \tag{10}$$

where:

η: efficiency (-), which depends on the laser source and the light-matter interaction.

It is worth considering this parameter, as it informs us about the outcome of the processing: high heat input results in slower cooling, leading to a microstructure that does not contain martensite, thereby reducing crack sensitivity. However, if the heat input is excessively high (resulting in very slow cooling), grain coarsening may occur [13]. The ISO 9606-1:2012 standard, according to the International Institute of Welding (IIW), also provides a carbon equivalent calculation to predict crack susceptibility, which determines whether preheating of the workpiece is necessary for a proper weld (CE < 0.4: preheating is not required; above this value, preheating becomes increasingly justified) [3, 9].

2.4. Penetration Depth

The penetration depth in laser welding is typically estimated using the Rosenthal equation. This equation assumes that the weld width is twice the penetration depth, the heat source is point-like, moves at a constant speed across the workpiece, and heat transfer is primarily described by conduction [1]. The equation has both two-dimensional and three-dimensional variants. The 2D model is applicable to cladding welds where penetration depth is negligible [1, 10]. Since we aim to express the penetration depth, the 3D model must be used, which assumes the heat source has a spatial extent and a Gaussian energy distribution:

$$T - T_0 = \frac{q}{2 \cdot \pi \cdot k \cdot h} exp\left(\frac{v_x \cdot \xi}{2 \cdot \kappa}\right) \times K_0\left(\frac{v_x \cdot r}{2 \cdot \kappa}\right) \tag{11}$$

where:

k: thermal conductivity coefficient (W/(m·K)),

h: penetration depth (m),

v_x: heat source velocity in the x-direction (m/s),

ξ: effective distance from the source position in the Lagrange coordinate system (m),

κ: thermal diffusivity coefficient (m^2/s),

K_0: zeroth order of the modified Bessel function (-).

It is worth noting that this equation must be modified when working with materials other than carbon steels or when using a non-continuous laser source [14].

2.5. Shielding Gas Flow

Laser welding falls under the category of fusion welding [3, 9]. Consequently, the molten pool must be protected from the environment (oxidation, contaminants), which is achieved using a shielding gas (or gas mixtures). This medium is directed at the molten pool with a specific flow rate. The gas flow rate (l/min) affects the appearance and, consequently, the mechanical properties of the weld. To ensure a high-quality weld, laminar flow must be maintained, although in some cases, transitional flow conditions may be necessary [10, 14]. This can be demonstrated using the Reynolds number.

$$Re = \frac{\rho \cdot v \cdot d_{spot}}{\mu} \tag{12}$$

where:

Re : Reynolds number (−),

ρ : density of medium (kg/m^3),

v : flow velocity of medium (m/s).

The Reynolds number describes the nature of a medium's (gaseous or liquid) flow, which can be laminar (ordered; Re < 2320), transitional (2320 < Re < 4000), or turbulent (Re > 4000) [15]. In the context of shielding gas flow, this is critical because turbulence can cause gas porosity or uneven protection in the welding zone [3, 9]. During conduction laser welding, laminar flow must be ensured, whereas transitional flow conditions are common in keyhole laser welding [14]. This is due to the specific characteristics of the technology: to allow energy to penetrate deeper layers, the keyhole (as shown on the right side of Fig. 1) must remain open, and the amount of generated plasma and metal vapor must be controlled, as they act as optical media and influence energy transfer [2, 16].

During welding, the desired gas pressure can be set using the shielding gas regulator. However, for professionals, this is not sufficient, as Welding Procedure Specifications (WPS) are typically based on volumetric flow rate:

$$Q = A_{spot} \cdot v = A_{spot} \cdot \frac{Re \cdot \mu}{\rho \cdot d_{spot}} \tag{13}$$

If a flow meter is not incorporated after the regulator, the pressure drop (ΔP) must first be determined using the Bernoulli equation (neglecting changes in elevation) [15]:

$$\Delta P = P_1 - P_2 = \frac{1}{2} \cdot \rho \cdot (v_2^2 - v_1^2) \quad (14)$$

where:

P_1 : pressure (Pa),

P_2 : nozzle exit pressure (Pa),

v_1 : medium velocity at the regulator outlet (m/s),

v_2 : medium velocity at the nozzle exit (m/s).

Based on this, the pressure value to be set on the regulator is the sum of the pressure drop and the nozzle exit pressure. It is important to note that the formula is modified if the nozzle length is not negligibly long [9].

It can be concluded that determining the parameters for laser welding for a specific task is a complex activity. To assist professionals, the calculations discussed earlier also form the basis for simulations [11, 14]. If access to such simulations is not available, it is advisable to conduct a series of experiments with the parameters mentioned in the studies, which can then be optimized for the specific task at hand.

3. Experiment

The key to successful handheld laser welding lies in the careful selection of appropriate technological parameters, which were analyzed in the previous section. The purpose of this chapter is to present the practical experimental investigation conducted at Intertechnika's Csepel workshop using an IPG Photonics LightWeld 1500 XC handheld laser welding device (Fig. 3). This device employs factory-preset welding programs (Fig. 4), ímeaning that precise values of certain input parameters (e.g., power, beam profile) are not accessible. Nevertheless, the focus of our investigation was to determine the extent to which these factory settings ensure high-quality welds.

The equipment used is one of the most advanced handheld laser sources available today [17]. Table. 1 outlines the specifications of the laser source.

Table 1. *IPG Photonics LightWeld 1500 XC machine specifications* [8]

Parameter	Value
Laser power (HPP-pulse mode)	150–2500 W
Laser power (CW-continuous wave mode)	150–1500 W
Operating modes	CW, Track, Modulation, HPP, Stitch, Clean, ADV. Stich
Laser source wavelength	1070 nm
Oscillation frequency	0–300 Hz
Oscillation amplitude	0–15 mm
Input voltage	200–240 V
Current consumption at full load	24 A
Rated power	4600 VA

The system is user-friendly, allowing the selection of a program from a table provided with the machine based on the base material, laser mode, and penetration depth (Fig. 4). Experiments were conducted in continuous wave (CW) mode, both with and without filler material (rows CW and M in the table). For welding with filler material, an IPG LightWELD WF-100 wire feeder device was used.

3.2. Experimental Materials

To investigate different penetration depths, we incrementally increased the sheet thickness from 1 mm to 5 mm in 1 mm steps. Not all sizes were available for a single material type in our environment, so we conducted experiments on DC01 (1 mm and 2 mm) and S355J2 (3 mm and above) carbon steels. In all cases, we produced single-sid-

Fig. 3. *IPG Photonics LightWeld 1500 XC handheld laser source and IPG LightWELD WF-100 wire feeder equipment.*

METAL	SHIELDING GAS	MODE	WELD DEPTH			
			0.040" (1.0mm)	0.080" (2.0mm)	0.120" (3.0mm)	0.160" (4.0mm)
STAINLESS STEEL	NITROGEN	CW	A1	A2	A3	A4
		M	C1	C2	C3	-
		W	A6	A7	A8	A9
MILD STEEL	NITROGEN	CW	E1	E2	E3	E4
		M	F1	F2	F3	-
		W	E6	E7	E8	-
GALVANIZED STEEL	NITROGEN	CW	-	-	-	-
		M	J1	J2	J3	-
		W	-	-	-	-
ALUMINUM 3XXX	ARGON	CW	-	-	-	-
		M	H1	H2	H3	H4
		W	-	-	-	-
ALUMINUM 5XXX	ARGON	CW	-	-	-	-
		M	L1	L2	L3	L4
		W	L6	L7	L8	L9

Fig. 4. *Laser source program table* [8]

ed fillet welds in a T-joint configuration, secured by pre-tacking the sheet ends. We were also interested in the filler material program mode (W: Wire welding), for which we used Böhler EMK 8 Ø1 mm solid wire electrode. As indicated in **Table 2** we consistently used nitrogen with a purity of 4.6 as the shielding gas at an operating pressure of 0.2 MPa.

Table 2. *Composition of the base materials used in the experiment*

Material	C%	Si%	Mn%	P%	S%	Cu%
S355J2	0.2	0.55	1.6	0.025	0.035	0.55
DC01	0.12	-	0.6	0.045	0.045	-
EMK 8	0.11	1	1.8	-	-	-

3.3. Investigation

We aimed to qualify the produced welds, so we conducted penetrant testing and subsequently prepared metallographic specimens for optical examination and hardness testing.

The liquid penetrant testing was performed at the Óbuda University, Bánki Donát Faculty of Mechanical and Safety Engineering. The testing was carried out in accordance with the ISO 3452-1:2021 standard. (**Fig. 5**)

The metallographic examination was conducted at the Budapest facility of Bay Zoltán Applied Research Nonprofit Ltd. The cross-sections to be examined were prepared in accordance with MSZ EN ISO 15614-1:2023. Thinner workpieces were cut using sheet metal shears, while for sheets 4 mm and thicker, an angle grinder was used. This method allowed us to cut a larger area to account for potential heat treatment effects, after which an abrasive cutting machine was employed with water cooling to achieve a size suitable for embedding. Sample preparation was carried out according to MSZ EN ISO 1463:2021. As our focus was solely on examining the weld shapes and potential defects, we polished the samples up to a 1 µm diamond suspension (for macro imaging). To reveal the microstructure, a 5% Nital etchant was used. (**Fig. 6.**)

The hardness testing was conducted within the university premises using the Vickers method with a 200 g load, as the heat-affected zones (HAZ) were expectedly narrow due to the characteristics of the technology. The results showed no anomalies; hardness values increased progressively from the base material toward the weld.

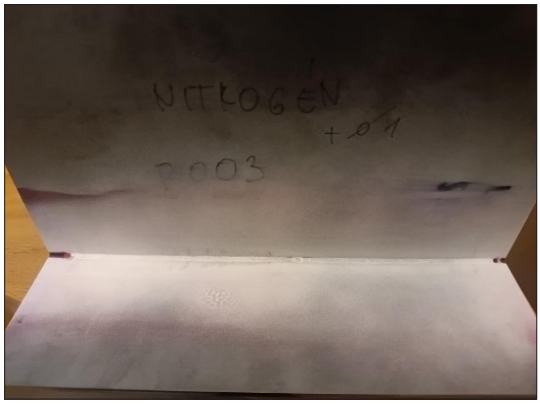

Fig. 5. *Result of penetration testing on a sample welded with filler material using the E8 program on 3 mm thick S355J2 sheet.*

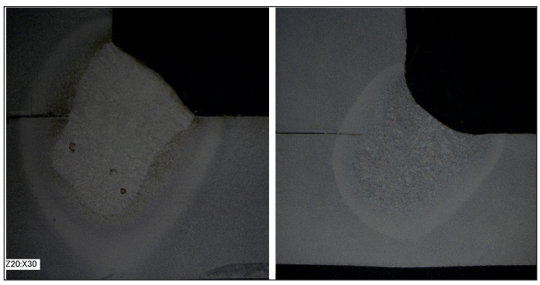

Fig. 6. *Samples made of S355J2 using the E4 program: 5 mm filler material weld (left) and 4 mm base material weld (right).*

3.4. Results

During visual inspection and penetrant testing, no surface-breaking material defects were observed. Microscopic images revealed spherical, porous welds (classified as defect code 2011 according to MSZ EN ISO 6250-1:2008) when using the parameter table recommended by the manufacturer. The most likely cause is uneven beam guidance and uncertainty in maintaining the position of the welding gun.

4. Conclusion

The key to high-quality welding lies in a thorough understanding of the applied technology. In many cases, it is acceptable to rely on seemingly trivial, empirical formulas and guidelines. However, for greater certainty, it is advisable to develop and simulate optimized technological parameters.

One of the sensitive parameters in laser welding is the welding speed, particularly due to the uncertainty associated with manual beam guidance.

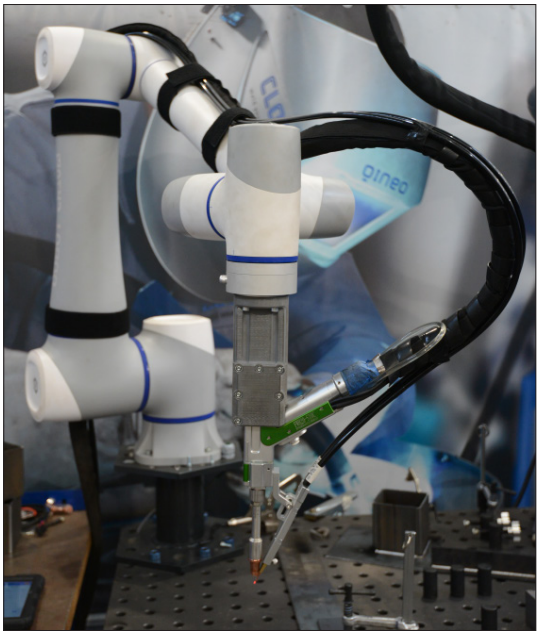

Fig. 7. *FWH20-S10A laser welding gun mounted on CR10A Dobot* **[4]**

Although it involves additional costs (potentially several million forints), creating a Welding Procedure Specification (WPS) for series or mass production is worthwhile, and integrating the laser source with a collaborative robot is recommended **[4]**.

The parameter table shown in **Fig. 4** specifies the shielding gas for welding (nitrogen). Although no evidence was found in the metallographic specimens, it is worth experimenting with other commonly used industrial shielding gases, as nitrogen can form nitrides with alloying elements in the base materials (in our case, potential Mn_4N and Si_3N_4 precipitations could have occurred).

Acknowledgment

The authors would like to express their gratitude to Intertechnika Ltd. for their support in conducting the experimental welds and providing equipment data, and to Bay Zoltán Applied Research Nonprofit Ltd. for their assistance in metallographic sample preparation and microscopic imaging.

References

[1] E. Kannatey-Asibu Jr.: *Principles of Laser Materials Processing Developments and Applications*. 2nd edition, Wiley, Hoboken, NJ, 2023.

[2] Buza G.: *Lézersugaras Technológiák I.* Edutus Főiskola, Budapest, 2012.

[3] Gáti J. (szerk.): *Hegesztési Zsebkönyv I.* Cokom Mérnökiroda Kft., Budapest, 2023.

[4] Gáti J., Kovács T., Nagy B.: *Gépesített kézi lézeres hegesztés gyakorlati tapasztalatai.* Hegesztéstechnika, XXXIV/ 4. (2024) 43–47.

[5] General Electric Company. Industrial hand held laser tool and laser system (US4564736A), Amerikai Szabadalmi Hivatal 1986. https://patents.google.com/patent/US4564736A/en

[6] Halász G.: *Kézi lézeres berendezések biztonságos használata.* Hegesztéstechnika XXXV/1. (2024) 41–47.

[7] MSZ EN ISO 4063:2023: Hegesztés, forrasztás és termikus vágás. A hegesztési eljárások megnevezése és azonosító számuk.

[8] LightWELD® Sorozatú Kézi Lézerhegesztő Rendszer Eredeti Használati Útmutató Fordítása, dokumentumszám: DOCCHUGMPSHU0018, Rev:2 (2023. november 29.)

[9] Bagyinszki G., Bitay E.: *Hegesztéstechnika I.: Eljárások és Gépesítés*. Erdélyi Múzeum-Egyesület, Kolozsvár, 2010. https://doi.org/10.36242/mtf-08

[10] Volpp J.: *High-Power Laser Material Processing for Engineers*. Taylor & Francis Group, LLC, 2025.

[11] Bitay E.: *Lézeres felületkezelés és modellezés*. Erdélyi Múzeum-Egyesület, Kolozsvár, 2007. https://doi.org/10.36242/mtf-04

[12] Salminen Antti Sakari: *Effect of welding parameters on the efficiency and energy distribution during laser welding with filler wire*. ICALEO 2001, Laser Institute of America, 2001. 409–418. https://doi.org/10.2351/1.5059891

[13] Messler, R. W.: *Principles of Welding: Processes, Physics, Chemistry, and Metallurgy*. Wiley, 2004. 167–168.

[14] Hekmatjou H., Zeng Z., Shen J., Oliveira J. P. Naffakh-Moosavy H.: *A comparative study of analytical Rosenthal, finite element, and experimental approaches in laser welding of AA5456 alloy*. Metals, 10/4. (2020) 436. https://doi.org/10.3390/met10040436

[15] Lajos T.: *Az áramlástan alapjai*. 5. kiadás, Akadémiai Kiadó, 2024. https://mersz.hu/lajos-az-aramlastan-alapjai/

[16] Buza G., Erős A., Fazekas É.: *A hegesztési munkagáz összetételének hatása a plazmaképződésre a lézersugaras hegesztés során*. Bányászati és kohászati lapok. Kohászat, 148/6. (2015).

[17] https://spark-co.com/en/2024/05/24/ipg-lightweld-what-you-need-to-know/?utm_source=-chatgpt.com (letöltve: 2025. április 16.)

Acta Materialia Transylvanica 8/2. (2025) 88–95.
DOI: Hungarian: https://doi.org/10.33923/amt-2025-02-08
English: https://doi.org/10.33924/amt-2025-02-08

Accuracy Examination of Hole Machining Methods

Viktor Gergely RÁCZI,[1] Balázs MIKÓ[2]

[1] *Óbuda University, Doctoral School on Materials Sciences and Technologies, Budapest, Hungary, raczi.viktor@bgk.uni-obuda.hu*

[2] *Óbuda University, Bánki Donát Faculty of Mechanical and Safety Engineering, Institute of Mechanical Engineering and Technology, Budapest, Hungary, miko.balazs@bgk.uni-obuda.hu*

Abstract

The geometric accuracy and surface quality of hole machining processes are fundamentally important for the operational reliability of manufactured components, as supported by the literature review. The aim of this research was to compare the geometric and surface characteristics of circular pockets produced by three different machining methods: turning, boring, and milling. During the investigations, coordinate measuring machine (CMM) and surface roughness measurement methods were applied, and the results were evaluated using the Taguchi method, signal-to-noise (S/N) ratio analysis, and weighted scoring assessment. Based on the results, boring proved to be the most favorable method in terms of geometric accuracy, while milling yielded better surface roughness values. The findings of this research can support the selection of appropriate pre-production machining technologies and contribute to the optimization of manufacturing processes.

Keywords: *geometric tolerance, hole machining, Taguchi experiment design.*

1. Introduction

The attainable geometric accuracy of cylindrical surfaces plays a decisive role in the operational reliability of manufactured components, particularly in applications where bearing fits, interference fits, or sealing functions are required. The aim of modern manufacturing technologies is not only to ensure dimensional accuracy, but also to minimize form deviations (such as cylindricity and roundness errors). For this reason, the comparison of different machining processes and the optimization of their technological parameters are indispensable.

To evaluate the geometric and dimensional accuracy of machined parts, various quantitative indicators can be applied, the definition and interpretation of which are described in detail by ISO standards. The ΔD (diameter deviation) represents the difference between the measured mean diameter and the nominal size, and is interpreted according to ISO 14405-1:2016 concerning dimensional tolerances. In addition to dimensional tolerances, geometric tolerances provide a more detailed description of the deviation of the manufactured feature. The RONt (total roundness deviation) expresses the departure from roundness and is defined according to ISO 12180-1 and ISO 12180-2 (**Fig. 1**/a).). This value represents the difference between the largest and smallest radii of the measured contour within a given cross-section. Similarly, CYLt (total cylindricity deviation) describes the overall departure from cylindricity, as defined in ISO 12181-1 and ISO 12181-2 (**Fig. 1**/b). This characteristic is interpreted as the radial distance between the smallest and largest concentric cylinders that completely enclose the measured surface. All three indicators are generally expressed in micrometers (μm) and are typically determined during form and dimensional inspections performed with coordinate measuring machines (CMM). In the present study *ΔD*, *RONt* and *CYLt* parameters were applied for the geometric characterization of the bore features.

Turning is one of the most widespread methods for producing cylindrical surfaces; however, in certain cases it cannot be applied (e.g., for assembled or non-axisymmetric components). In such situations, alternative machining processes (e.g., milling or boring) come to the fore.

During milling operations, in addition to cutting

parameters, other conditions also influence the accuracy of the machined surface, such as cooling and lubrication conditions [1]. Based on experimental results, the most promising outcome was obtained with a cutting speed of 65.46 m/min, a table feed rate of 0.3 m/min, and an emulsion flow rate of 1.16 l/h, where the *CYLt* value was 19.20 µm and *CYLv* was 8.52 µm [1].

Measurements have shown that the type and amount of lubricant significantly affect the *CYLt*, *CYLp*, and *CYLv* values. According to research findings, the lowest *CYLt* value (13.31 µm) was achieved with a cutting speed of 188.5 m/min, a feed of 0.05 mm/rev, and an emulsion flow rate of 546 cm^3/min [2, 3].

The analysis of various form errors has also received increasing attention in tangential turning. Due to its specific kinematic characteristics, this method is highly suitable for machining high-precision cylindrical surfaces; however, form deviations – particularly *CYLv* and *RONt* – are strongly dependent on cutting speed and depth of cut [4].

In the comparison of hard machining processes (hard turning of hardened steels and grinding), *RONt, CYLt, CYLtt* and *Ra* indicate that hard turning can be a competitive alternative to conventional grinding, particularly when machining is performed in a single setup on the same machine [5].

Honing, as a finishing operation, also contributes to the production of bores with excellent form accuracy. In the work of Nagypál and Sztankovics [6], it was demonstrated that the structure of the abrasive tool and the feed rate influence *CYLt, CYLtt* and *RONt* – the use of smaller grain sizes and denser structures resulted in improved cylindricity.

Special attention should also be given to processes based on mechanical surface modification (non-cutting). Ferencsik and Varga investigated the effects of diamond tool burnishing on microhardness and cylindricity in several studies [7, 8], and demonstrated that, with appropriate burnishing parameters, form accuracy can be significantly improved.

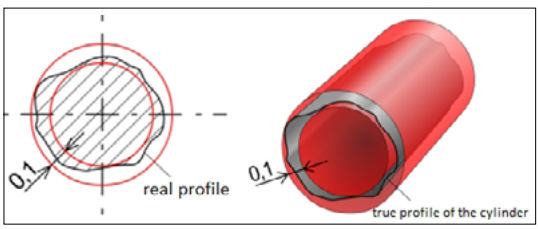

Fig. 1. *Determination of geometric deviations in circularity (a) and cylindricity (b).*

The combined findings of these studies indicate that various cutting and forming processes affect the development of geometric form accuracy, and that the careful selection of technological parameters is always required to achieve the desired outcome.

The aim of the present study is to investigate to what extent the geometric accuracy of bored cavities – particularly in terms of cylindricity, roundness, and surface roughness parameters – approaches that of workpieces produced by turning. The results may help to determine whether, in future experiments, boring alone is sufficient for the pre-machining stage.

2. Materials and methods

During the machining experiments, circular pockets were produced using three different machining technologies. In all three cases, cemented carbide tools supplied by Walter Hungária Ltd. were employed. For the circular pockets produced by turning, an A20S-SDQCL11 boring bar equipped with a DCMT11T304-MP4-WPP20G insert was applied (**Table 1**/No. 1). For the workpieces machined by boring, a B4030G.T28.33-41.Z tool and a TCMT06T104-FP4 insert were used (**Table 1**/No. 2), while for the circular pockets produced by milling, an H4021017-20 end mill was employed (**Table 1**/No.3).

The machining experiments were carried out on a MAZAK SQT 10 MS CNC turning center and a Mazak Nexus 410A-II CNC milling machine. Tool condition assessment and verification of their geometric dimensions (actual tool diameter determination for boring and milling tools) were performed using an Elbo Controlli Hathor laser tool presetter.

The machining tests were conducted on C45 (1.0503) quenched and tempered carbon steel with the following chemical composition: C: 0.43-0.5%; Si: <0.4%; Mn: 0.5-0.8%; Ni: <0.4%; P: <0.045%; Cr: <0.4%; Mo: <0.1%. Due to its excellent mechanical properties, this material is widely applied as a base material for mechanical and structural components. The workpieces used in the experiments, with a geometry of Ø80 x 70 mm, exhibited a hardness of HV30 185 ± 7.3 (σ: 3.65).

The preforms of the workpieces used in the experiments were produced on the MAZAK SQT 10 MS CNC turning center in two setups. During the

tests, a circular pocket of Ø34 mm was finished to a depth of 32 mm (Fig. 2). The depth of cut (a) (in the case of milling, width of cut (ae)) was 0.5 mm. To ensure comparability of the experimental results, the material removal rate (V' [mm³/min]) was kept identical for all three machining processes. The machining experiments were performed under flood cooling conditions using a 6% solution of MOL Emolin 420.

The machining experiments were designed according to the Taguchi experimental design method (L9). During the investigation, for each machining process the cutting speed (v_c) and the feed per tooth (f_z) were varied at three levels. The applied technological parameter values are presented in Table 2.

2.1. Coordinate measurement investigations

Following the machining experiments, the geometric errors of the circular pockets (*RONt, CYLt*) and their dimensional deviations from the theoretical geometry (ΔD) were determined using a Mitutoyo CRYSTA-Apex V544 CMM. The investigated geometric deviations were evaluated at eleven depth levels (h: 2; 4.5; 7; 9.5; 12; 14.5; 17; 19.5; 22; 24.5; 27 mm), with 24 measurement points per level (total: 264 points).

The surface roughness parameters (*Ra, Rz*) were measured using a Mahr MarSurf GD 120 profilometer. During the investigation, each machined surface was measured in three angular positions (0°, 120°, 240°) and at three depths (0, 9, 18 mm), resulting in a total of nine measurements, applying an evaluation length of $l_t = 4.8 + 2 \cdot 0.8$ mm according to MSZ EN ISO:21920:2022.

The measurement results were evaluated using the dedicated software of the measuring devices and further analyzed with MINITAB 22 software.

For the determination of the results, the Least Squares Cylinder Fit method was applied, which minimizes the sum of squared distances between the measured points and the theoretical diameter, perpendicular to the axis of the fitted circle or cylinder center. The obtained results were also represented graphically.

3. Presentation of the measured values

The results of the deviation from the theoretical diameter (ΔD) are presented in Fig. 3, where the distribution of 264 measurement results is shown. Based on the data, it can be established that the different machining processes can be clearly distinguished. For turning and boring technologies, it was observed that the machining process had only a minor influence on the deviation from the theoretical geometry, while in the case of milling this effect was significant. Turning produced the smallest ΔD deviation (on average −0.02 mm), whereas boring resulted in circular pockets with an average oversize of +0.09 mm. Based on the

Table 1. *Tools used in the experiments*

No.	Tool	Insert
1	A20S-SDQCL11	DCMT11T304-MP4-WPP20G
2	B4030G. T28. 33-41.Z	TCMT06T104-FP4
3	H4021017-20	

Table 2. *Technological parameters used in the experiments*

Turning			Boring			Milling		
No.	v_c (m/min)	f_z (mm)	No.	v_c (m/min)	f_z (mm)	No.	v_c (m/min)	f_z (mm)
1	180	0.05	4	180	0.1	7	180	0.15
2	200	0.1	5	200	0.15	8	200	0.05
3	220	0.15	6	220	0.05	9	220	0.1

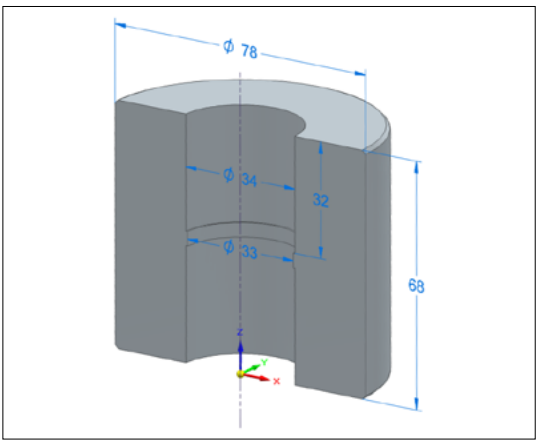

Fig. 2. *Workpiece used in the experiment.*

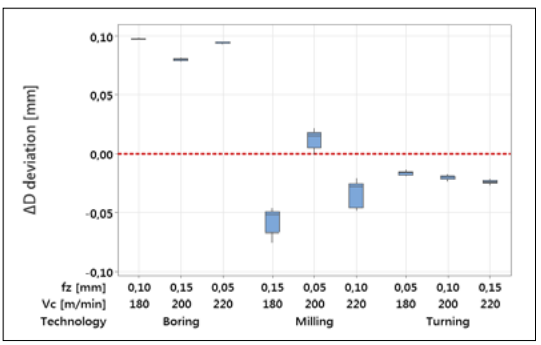

Fig. 3. *Deviation from theoretical size.*

force measurement results and the experiments conducted in Necurom 651 artificial wood, it was concluded that the geometric deviation of the diameter was caused by tool deflection.

Using the measured points, the roundness deviation (*RONt*) corresponding to each depth level was determined (Fig. 4). Based on the data, it can be established that turning and boring result in nearly identical roundness deviations, while in milling not only is the scatter of the data considerably larger, but the investigated geometric deviation is also 2.8 times higher compared to the average value obtained for turning. The results once again confirm that, in the case of milling, the technological parameters exert a significant influence on the magnitude of roundness deviation.

The results of the cylindricity (*CYLt*) analysis of the circular pockets are presented in Fig. 5, where the outcomes of 36 measurements (9·4) are shown. Based on the results, it can be concluded that the smallest cylindricity deviation was obtained for the circular pockets produced by turning. In the case of boring, the cylindricity value deviated on average by 10% compared to the turned pockets, while for the workpieces produced by milling the average deviation was 2.9 times higher. The data also clearly indicate that, in milling, the technological parameters exert a stronger influence on the cylindricity values.

3.1. Surface roughness investigations

The results of the average surface roughness (*Ra*) are summarized in Fig. 6. The lowest Ra values were obtained with milling. In comparison, turning resulted in an average *Ra* that was 2.6 times higher, while boring produced an average *Ra* that was 2.8 times higher. For milling, the technological parameters had no significant effect on the average surface roughness, whereas in turning and boring the Ra values were strongly influenced by the cutting parameters. Furthermore, it was established that surface homogeneity is considerably more advantageous when using single-edge tools compared to multi-edge tools.

In the surface roughness investigations, the other parameter examined was the mean peak-to-valley height (*Rz*), the results of which are presented in Fig. 7. The lowest *Rz* values were obtained for the circular pockets produced by milling, while boring resulted in values that were on average 1.8 times higher, and turning produced Rz values that were on average 2.1 times higher. Based on the scatter of the results, it can be stated that the homogeneity of the workpieces produced

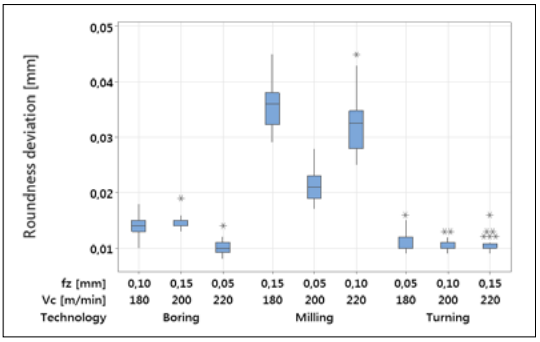

Fig. 4. *Development of roundness deviation during the examination.*

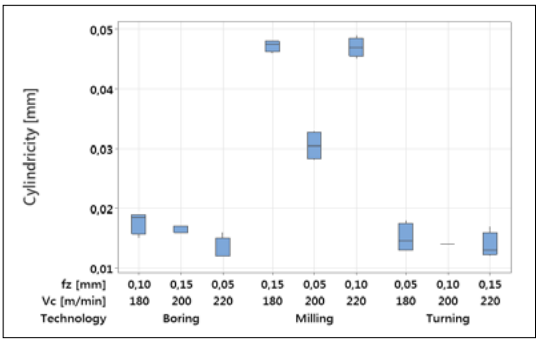

Fig. 5. *Development of cylindricity during the examination.*

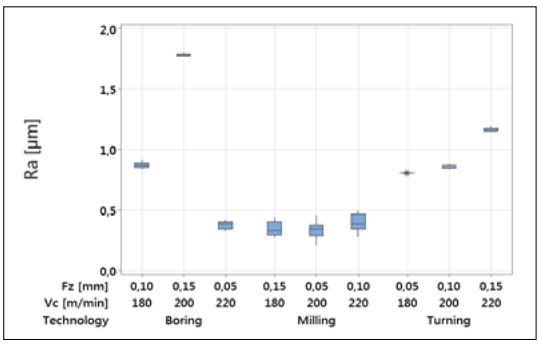

Fig. 6. *Average surface roughness development during the test.*

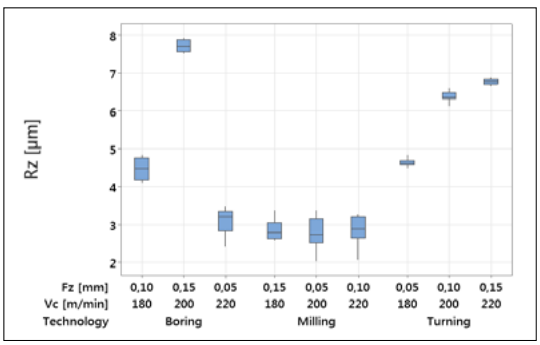

Fig. 7. *Development of mean peak-to-valley height during the examination.*

by turning is much more favorable than with the other processes. In the case of boring, the lack of sufficient cooling intensity likely caused the scatter of the Rz results, since the continuous chip could not be effectively removed from the pocket.

4. Analysis of the measured values and findings

For the evaluation of the experimental results, the Taguchi method was applied, which enables the simultaneous investigation of the effects of multiple factors with a relatively small number of experiments. During the analysis of the data, evaluation was performed exclusively on the basis of the Signal-to-Noise Ratio (S/N). The calculation of the S/N ratio makes it possible to consider not only the average results, but also the scatter and stability of the measurement data. This provides a more reliable picture of the consistency and predictability of a given technological setup performs. The method is widely used in Design of Experiments (DOE), manufacturing technology, and quality assurance, especially in situations where the aim is to improve process robustness [9, 10].

In assessing the effects of the factors, the magnitude of the delta value (Δ) was taken into account, which represents the difference between the S/N ratios obtained at the best and worst levels of a given factor (Eq. 1). The magnitude of the delta value is proportional to the effect of the factor on the outcome, and thus the order of importance of the factors can be established based on these values [9].

$$\Delta = S/N_{max} - S/N_{min} \quad (1)$$

For the “Nominal is Best” case read:

$$S/N = -10 \cdot log_{10}(s^2) \quad (2)$$

where:

s: the standard deviation of the y values.

For the “Smaller is Better” case, the equation is:

$$S/N = -10 \cdot log_{10}\left(\frac{1}{n}\sum_{i=1}^{n} y_i^2\right) \quad (3)$$

where:

y_i: i-th measured value,

n: number of measurements.

4.1. Coordinate measurement investigations

Fig. 8 shows the main effects plot of the signal-to-noise ratios calculated from the deviation of the theoretical diameter. According to the “Nominal is Best” type signal-to-noise ratio (Eq. 2), a higher value indicates better process stability. The greatest effect on diameter accuracy was exerted by the machining method (Δ = 21.87), while feed (Δ = 1.75) and cutting speed (Δ = 1.05) had smaller influences. Although boring produced larger deviations (Fig. 3), this method nevertheless ensured the most stable and repeatable results, which can be corrected to achieve higher accuracy. Milling exhibited a 35% lower signal-to-noise ratio, and thus its accuracy proved to be suboptimal. The best result was obtained at a cutting speed of 180 m/min and a feed of 0.05 mm.

For the evaluation of roundness deviations, the “Smaller is Better” type signal-to-noise ratio was applied, since the aim was to minimize form errors (Eq. 3). Based on Fig. 9, the greatest effect was exerted by the machining method (Δ = 8.67), while feed (Δ = 2.36) and cutting speed (Δ = 1.47) had smaller influences on the result. Turning ensured the best stability, while boring showed a 4% less favorable signal-to-noise ratio, and milling exhibited a 22% less favorable value. The best results were obtained at a cutting speed of 200 m/min and a feed of 0.05 mm.

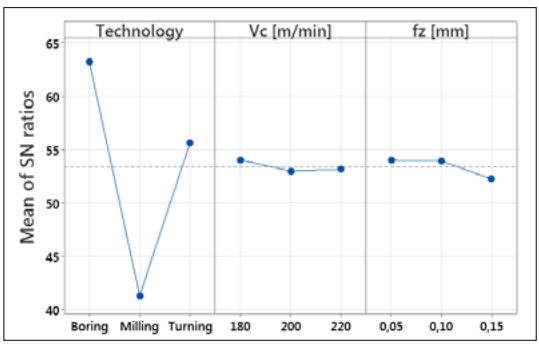

Fig. 8. *Main effects plot of the signal-to-noise ratio for the deviation from the theoretical diameter.*

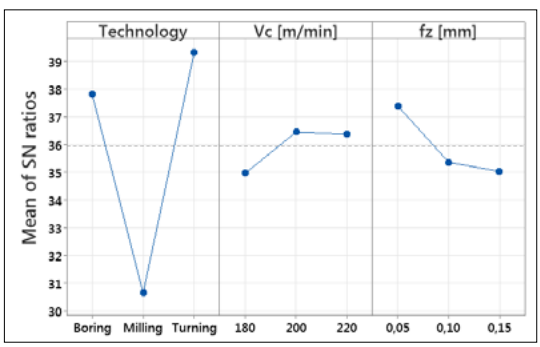

Fig. 9. *Main effects plot of the signal-to-noise ratio for roundness.*

The evaluation of cylindricity deviations was also conducted using the "Smaller is Better" type signal-to-noise ratio, since the objective was to reduce geometric errors (Eq. 3). According to Fig. 10 the greatest effect was exerted by the machining method (Δ = 9.09), while feed (Δ = 1.91) and cutting speed (Δ = 1.68) had a smaller influence on the results. Turning ensured the most stable cylindricity values, boring showed a 2% lower but still promising signal-to-noise ratio, while milling resulted in a 25% lower ratio, indicating higher scatter and instability. The best results were obtained at a cutting speed of 200 m/min and a feed of 0.05 mm.

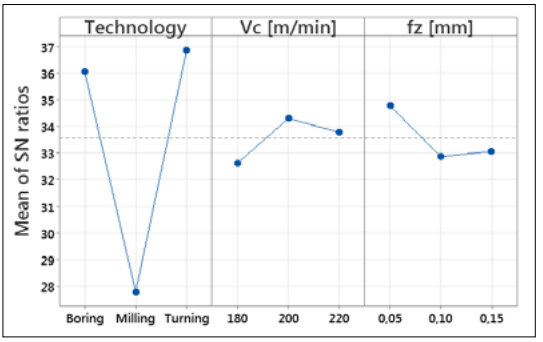

Fig. 10. *Main effects plot of the signal-to-noise ratio for cylindricity.*

4.2. Surface roughness investigations

For the evaluation of surface roughness (Ra), the "Smaller is Better" type signal-to-noise ratio was applied, in order to achieve smoother surfaces (Eq. 3). According to Fig. 11 the machining method had the most significant effect (Δ = 8.21), with milling providing the best surface quality. In the case of turning, the *Ra* value was 93% higher, representing the most unfavorable result. Feed also had a strong influence on roughness (Δ = 5.66), with the 0.05 mm value producing the smoothest surfaces. Cutting speed had a smaller effect (Δ = 3.17), with the best results obtained at 220 m/min, while 200 m/min yielded the lowest stability.

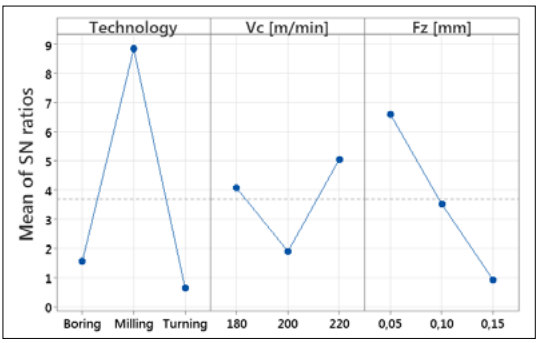

Fig. 11. *Main effects plot of the signal-to-noise ratio for arithmetic mean height (Ra).*

For the *Rz* roughness parameter, similar results were obtained as for *Ra*, therefore the evaluation was also carried out using the "Smaller is Better" type signal-to-noise ratio (Eq. 3). According to Fig. 12 s, the machining method had a decisive effect on the stability of *Rz* (Δ = 6.27), with milling providing the most favorable results. In the case of turning, the *Rz* value was 69% higher, indicating poorer surface quality. Feed also had a significant influence (Δ = 3.80), with the lower feed (0.05 mm) producing the smoothest surface. Based on the effect of cutting speed (Δ = 2.45), the best results were observed at 220 m/min, while at 200 m/min the greatest deterioration was recorded.

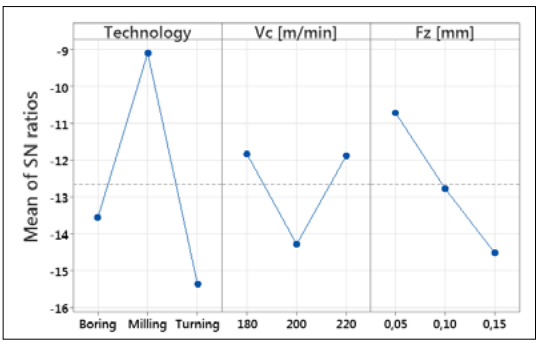

Fig. 12. *Main effects plot of the signal-to-noise ratio for peak-to-valley height (Rz).*

4.3. Evaluation of the data

Based on the results of the signal-to-noise ratios, it can be established that the machining method exerted the most significant effect on all of the investigated response parameters. According to Table 3 sthe deviation from the theoretical diameter was most strongly influenced by the applied machining process, while the effect of cutting speed and feed was considerably smaller.

Table 3. *Summary values of the signal-to-noise ratio for ΔD*

Level	Technology	V_c m/min	f_z mm
1	55.61	54.02	53.97
2	63.19	52.97	53.92
3	41.32	53.14	52.23
Delta	24.87	1.05	1.75
Rank	1	3	2

Table 4. *Summary values of the signal-to-noise ratio for RONt*

Level	Technology	V_c m/min	f_z mm
1	39.32	34.97	37.40
2	37.82	36.45	35.37
3	30.65	36.37	35.03
Delta	8.67	1.49	2.36
Rank	1	3	2

Table 5. *Summary values of the signal-to-noise ratio for CYLt*

Level	Technology	V_c m/min	f_z mm
1	36.87	32.63	34.78
2	36.06	34.31	32.87
3	27.79	33.78	33.07
Delta	9.09	1.68	1.91
Rank	1	3	2

Table 6. *Summary values of the signal-to-noise ratio for Ra*

Level	Technology	V_c m/min	f_z mm
1	0.6367	4.0839	6.5947
2	1.5678	1.8993	3.5221
3	8.8488	5.0701	0.9365
Delta	8.2121	3.1708	5.6582
Rank	1	3	2

Table 7. *Summary values of the signal-to-noise ratio for Rz*

Level	Technology	V_c m-min	f_z mm
1	-15.355	-11.830	-10.711
2	-13.544	-14.277	-12.764
3	-9.084	-11.876	-14.508
Delta	6.270	2.447	3.797
Rank	1	3	2

A similar trend can be observed in **Table 4** and **5** where the stability of roundness and cylindricity deviations was also most strongly affected by the machining method.

In terms of surface roughness characteristics (**Table 6** and **7**) milling provided the most beneficial signal-to-noise ratio. In contrast, with respect to roundness and cylindricity deviations, turning yielded the best results.

Summarizing the geometric and surface roughness outcomes, it can be concluded that boring ensured the most balanced and stable machining performance, with favorable accuracy and surface quality.

The influence of cutting speed (v_c) was of moderate magnitude, with the best values generally obtained in the range of 200–220 m/min. For feed (f_z), a clear trend was observed: the low feed value of 0.05 mm consistently produced an outstanding signal-to-noise ratio across all response parameters.

5. Conclusions

The aim of this research was to compare circular pockets produced by three different machining methods (turning, boring, and milling) based on geometric deviations (*ΔD, RONt, CYLt*) and surface roughness parameters (*Ra, Rz*). Coordinate measurement and surface roughness measurement procedures were applied, and the results were evaluated using the Taguchi method by calculating signal-to-noise ratios.

Based on simple average values, turning provided the most favorable results regarding geometric characteristics, closely followed by boring. In contrast, milling exhibited larger deviations and scatter in all geometric parameters.

According to the surface roughness data, the milling process resulted in the lowest average Ra and Rz values; however, turning and boring ensured more stable and homogeneous surface quality.

Overall, the best combined results were obtained with the boring process. Among the cutting parameters, the combination of the highest cutting speed (220 m/min) and the lowest feed rate (0.05 mm) yielded the best accuracy and surface quality.

References

[1] Varga G.: *Analysis of Cylindrical Deviations in Nonconventionally Machined Cylindrical Workpieces.* GÉP, 75/1. (2024) 47–50. https://doi.org/10.70750/GEP.2024.1.10

[2] Varga G., Puskás T., Debreceni I.: *Analysis of Cylindrical Error Deviation of Surfaces Ehen Using Reduced Amount of Coolants and Lubricants in Machining.* WSEAS Transactions on Applies Theoretical Mechanics, 13. (2018) 103–116.

[3] Varga G., Puskás T., Debreceni I.: *Examination of Shape Error of Outer Cylindrical Surfaces Machined by Environmentally Friendly Way.* International Journal of Mechanical Engineering, 3. (2018) 43–51.

[4] Sztankovics, I., Pásztor I. : *Shape Error Analysis of Tangentially Turned Outer Cylindrical Surfaces*. Acta Technica Corviniensis, 15/4. (2022) 23–28.

[5] Kundrák J., Sztankovics I., Lukács F.: *Comparative Analysis of Hard Machined Bores Based on the Roughness and Accuracy*. Cutting & Tools in Technological System, 92. (2020) 19–25. https://doi.org/10.20998/2078–7405.2020.92.03

[6] Nagypál G., Sztankovics I.: *Furatok alakhibájának vizsgálata az előtolás függvényében hónoló megmunkálásnál.* Multidiszciplináris Tudományok, 10/2. (2020) 481–486. https://doi.org/10.35925/j.multi.2020.2.53

[7] Ferencsik Varga V.: *Analysis of Shape Correctness of Surfaces of Diamond Burnished Components.* MATEC Web of Conferences, 137. (2017) 01019. https://doi.org/10.1051/matecconf/201713701019

[8] Ferencsik V.: *A vasalási eljárás felületi keménységre és hengerességre gyakorolt hatásának vizsgálata különböző anyagminőségek esetén.* Multidiszciplináris Tudományok, 12/5. (2022) 22–30. https://doi.org/10.35925/j.multi.2022.5.3

[9] Montgomery D. C.: *Design and Analysis of Experiments.* (9th ed.). John Wiley & Sons, 2017. ISBN: 978-1119113478

[10] Drégelyi-Kiss Á.: *Application of Experimental Design-Based Predictive Models and Optimization in Additive Manufacturing–a Review.* Hungarian Journal of Industry and Chemistry, 52/1. (2024) 55–70. https://doi.org/10.33927/hjic-2024-08

Acta Materialia Transylvanica 8/2. (2025) 96–104.
DOI: Hungarian: https://doi.org/10.33923/amt-2025-02-09
English: https://doi.org/10.33924/amt-2025-02-09

Compression Strength Testing of Grey Poplar

Fanni SZŐKE,[1] Sándor TÁRKÁNYI,[2] Antal KÁNNÁR[3]

[1] *University of Sopron, Faculty of Wood Engineering and Creative Industries, Institute of Creative Industries, Sopron, Hungary, Szoke.Fanni@phd.uni-sopron.hu*

[2] *University of Sopron, Faculty of Wood Engineering and Creative Industries, Institute of Creative Industries, Sopron, Hungary, tarkanyi.sandor@uni-sopron.hu*

[3] *University of Sopron, Faculty of Wood Engineering and Creative Industries, Institute of Creative Industries, Sopron, Hungary, kannar.antal @uni-sopron.hu*

Abstract

Knowledge of the strength values of Populus canescens is important for expanding the range of applications of this species. The use of wood as an orthogonally anisotropic material in structural engineering is significantly influenced by its strengths in different anatomical directions. The results obtained from tensile and compressive strength tests of test specimens in the main anatomical directions allow the determination of the strength surface, which makes it possible to determine the strength of wood in any direction. A further within-group classification is provided by the separation of sapwood and duramen, so that the strength behaviour of the individual wood sections within the wood body can be revealed in addition to the different ultimate strengths.

Keywords: *grey poplar, strength surface, anisotropy.*

1. Introduction

Research in forestry has shown that increasing average annual temperatures and decreasing precipitation has led to increased mortality of sensitive tree species [1]. Poplar (Populus canescens), which is indigenous to Hungary and has a significant native population, offers an excellent opportunity to replace declining populations due to climate change. It is a fast-growing, highly productive species, occupying 1.5 million hectares of forest area in today's Hungarian forestry, of which 1.3-1.5 million m3 of timber is traded annually. This volume represents 23-25% of the total annual timber production. Its use is to produce crates, pallets, coasters, particleboard, fibreboard [2]. Its structural use is in principle possible due to its higher-than-average density of poplar species, but further strength testing is needed for predictable design. The present research aims to determine the strength surfaces resulting from anisotropic properties in different anatomical shapes.

2. Materials and methods

The sapwood and the heartwood parts of the grey summer are clearly separated. The moisture content of the strap, present in a proportion of 30-40%, is higher than that of the gizzard, but the literature shows that there is no significant difference in their physiological characteristics. In the design of the test specimens, the separation of the two parts of the wood was taken into account to obtain more distinct strengths for each part and to avoid results that are influenced by the different moisture content. Care must be taken to ensure that the specimens are of the correct length dimensions. If the specimen is too long, the normal stresses from compression will be accompanied by buckling and stress from bending, while if the specimen is too short, the stress plateau at the transfer locations will influence the linear stress-strain state of the central part. The ideal size is defined in the literature as a length of the test specimen 2-3 times the minimum cross-sectional dimension [3, 4]. On this basis, I have defined the nominal size of my own specimens as 20 × 20 × 50

mm. In the strength tests, the consideration of anatomical directions on the specimens was given priority. As shown in the first figure, longitudinal (L), radial (R), tangential (T) directions and their planes were distinguished, on which specimens with 0°, 45° and 90° designs were prepared depending on the direction (Fig. 1). The multi-directional specimens made it possible to determine the strength surfaces later.

The 45° fibre run is used to experimentally determine the shear strength, based on Askenazi's anisotropic strength theory and practical experience [3]. The design allows the specimens to shear parallel to the principal axis of the anatomical principal planes, despite normal loading, with normal and shear stresses. Pure shear will still not occur, but the distribution of shear stress along the shear cross section will be uniform, which is not the case with other methods. The influence of normal stresses on the shear stress can be determined by a comparison between the maximum of the principal stress functions of the tensile and compressive strength tests, which are shown to have no influence on the shear strength within a certain probability level. Thus, shear strength can be indirectly determined by tensile strength measurements [4].

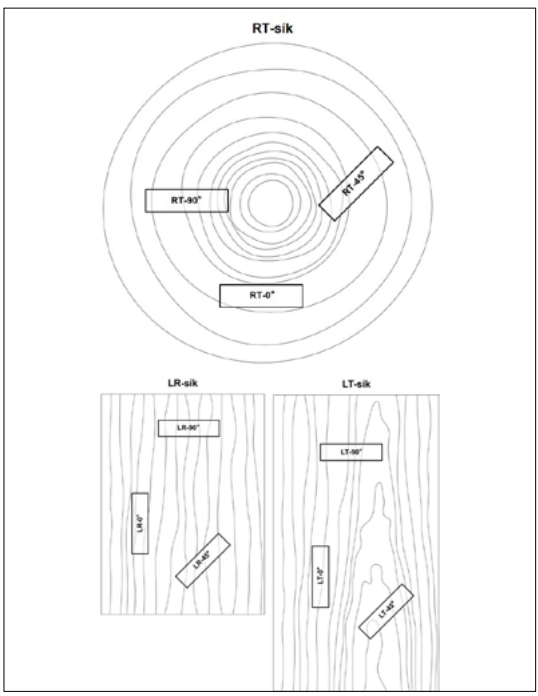

Fig. 1. *Directional design of the test specimens.*

Thus, shear strength can be indirectly determined by tensile strength measurements. During the tests, 30 straps and the same number of studs per direction - LR0°, LR45°, LR90°, LT45°, LT90°, RT45° - were measured for compressive strength in a total of about 400 test specimens, using an Instron 5985 universal material testing machine. With this number of specimens, strength values can be determined with an accuracy of about 0.2 MPa. The measurement procedure was based on the ISO 13061-17 standard, which specifies, among other things, that the tests should be conducted for a period of between 1 and 5 minutes until the specimen breaks. [5] In order to achieve the standard, the instrument test speed was calibrated to 0.6 mm/min, but due to the anatomical orientation and different strengths of the LT90 and LR45 gauge specimens, the speed had to be increased to 1.2 mm/min for the LT90 and LR45 heartwood specimens and 1.8 mm/min for the LR45 sapwood and LT45 specimens. Moisture content was determined by wet and absolute dry mass, converted to 12% air dry mass using the standard conversion formula (1). The compressive strength is represented by „σ", „u" is the moisture content, „α" is a correction factor for the variation of the Si-strength per moisture content, with a value of 0.04 [5]:

$$\sigma_{12} = \sigma_U[1 + \alpha(U - 12)] \quad (1)$$

The stress values thus corrected, calculated as the ratio of the maximum force to the head area, can be considered for the literature comparison, which also refer to air-dry strength.

In addition, the elastic modulus of the test specimens has been determined, which also influences the shape of the curves presented later. To do this, the specific length change must be expressed as the ratio of the total length change to the original length (2):

$$\varepsilon = \frac{\Delta L}{L} \quad (2)$$

The modulus of elasticity can be defined as the ratio of the compressive stress divided by the corresponding specific strain in the linear elastic range, given the data (3):

$$E = \frac{\sigma}{\varepsilon} \quad (3)$$

The calculations were performed on the results of all samples to exclude measurement errors and then evaluated, considering the minimum, maximum, mean, standard deviation.

3. Results and their evaluation

During the test, the instrument produced a force-displacement diagram for each specimen, which clearly shows the failure and its extent. The individual sections can be clearly identified in each case. The first stage was surface levelling, followed by a linear rising stage, which showed a steady absorption of the force. Its steepness was influenced by the elastic modulus. In the third phase, cracks in the specimen were not visible until the point of maximum force absorption. Fracture of the wood structure, with visible stump loss, occurred in the fourth and final phase, which the instrument continued until a 40% setback. All tests were performed up to the point of visual failure.

The force-displacement diagrams of the LR0 sapwood specimens show the different phases (Fig. 2). The linear phase is followed by a curved phase, the failure is observed in the fourth and final phase, where there is no sudden breakage, only a slight decrease in force. The strength data are shown in Table 1–6.

In the same direction, the test specimens in the heartwood showed a slightly lower force absorption (Fig. 3), while a much more significant decrease was observed in the failure section. The sudden jump was caused by specimen fracture.

According to the literature, several different basic types of fracture patterns can be distinguished in the longitudinal direction parallel to the fibres, such as collapse, wedge-shaped cleavage, shearing, splitting, collapse and splitting, and end sliding and opening [6]. The fracture pattern typical of these specimens during testing is shown in the following figure (Fig. 4). It can be clearly seen that the most typical failure mode is shearing, which is associated with small cracks in the heartwood specimen, which is the cause of the failure mode shown in the diagram.

In the LR45 direction, the typical diagrams of the sapwood patterns (Fig. 5) start with a steep linear phase, followed in all cases by an abrupt change to a steeper phase with a smaller slope in the third, unobservable failure stage. In the fourth stage, after continuous fragmentation, there was a sudden stump transition.

The heartwood specimens produced a curve with a smaller slope than the sapwood, without any prominent change (Fig. 6). After the gradual cracking in the stub-retraction section, a sudden fracture occurred, causing the specimen to separate.

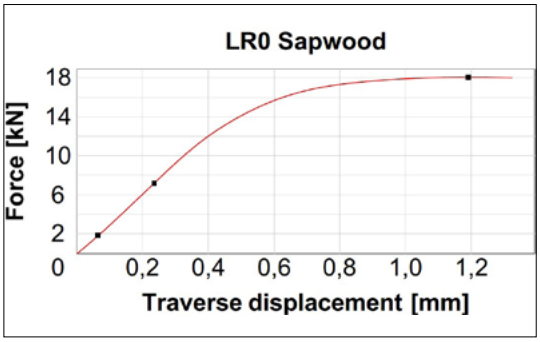

Fig. 2. *Force-displacement diagram – LR0 sapwood.*

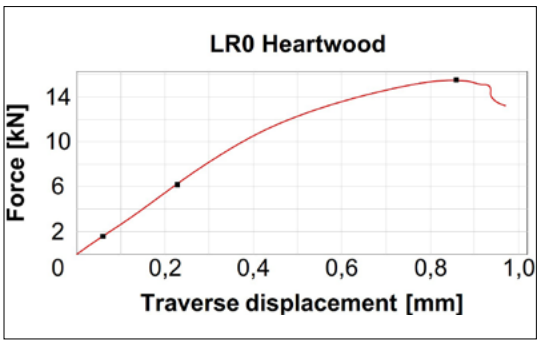

Fig. 3. *Force-displacement diagram – LR0 heartwood*

Fig. 4. *Typical fracture pattern of the test specimens – LR0.*

The fracture patterns (Fig. 7) typically showed collapse and shear along the annual rings in the case of the sapwood. The specimens remained intact with significant residual deformation. In all cases, the heartwood was brittle, and the fracture patterns were characterised by shearing, resulting in separation of the test specimen without significant permanent deformation.

The diagram of the LR90 sapwood specimens (Fig. 8) shows a steady slope, with no abrupt

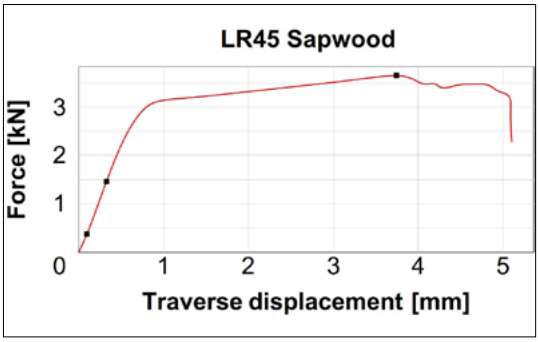

Fig. 5. *Force-displacement diagram – LR45 sapwood.*

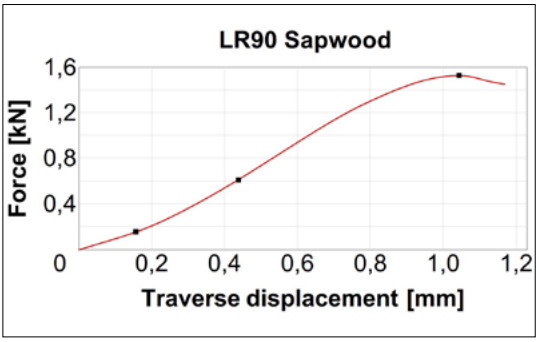

Fig. 8. *Force-displacement diagram – LR90 sapwood.*

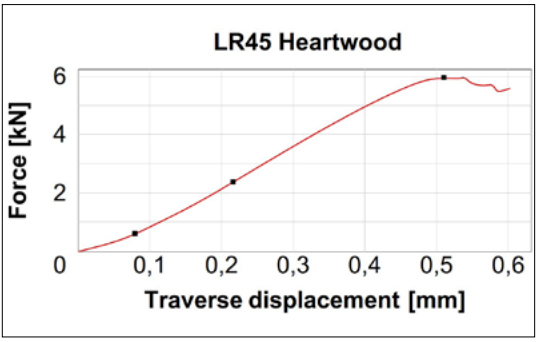

Fig. 6. *Force-displacement diagram – LR45 heartwood.*

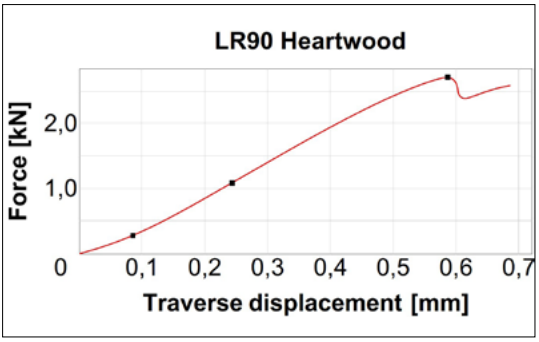

Fig. 9. *Force-displacement diagram – LR90 heartwood.*

Fig. 7. *Typical fracture pattern of the test specimens – LR45*

Fig. 10. *Typical fracture pattern of the test specimens – LR90.*

breakage even at the failure stage. The fibres compressed gradually and proportionally during the test.

The heartwood (**9. ábra**) shows a similar curve, except for the last section, where in almost all cases there was a significant drop after the point of maximum force application, indicating a sudden crack. This process was so rapid that the test specimen started to regain strength, which was observed on the minor uphill section.

According to the literature, tangential and radial stress-indicating fractures in the perpendicular to the rostra are the collapse of an area of the early pastes (shearing along a tree-ring) and the bulging of tree-rings **[6]**.] In the case of the sapwood, the early lattice was characterised by collapse, while the heartwood was also characterised by shearing, which was also reflected in the protrusion of the growth ring (**Fig. 10**).

The diagram of the LT45 sapwood specimen (Fig. 11) shows the same pattern as the LR45 sapwood, however, in the failure phase there were no sudden shift-zones, a low intensity decreasing phase was observed.

The heartwood samples also showed a similar curve with a smaller slope in the linear phase (Fig. 12). AThe rapid decrease in the scale in the last phase was caused by the complete fracture of the specimen.

The fracture patterns for the LT45 specimens (Fig. 13) were characterised by shear, associated with a kind of „S" shaped permanent deformation of the sapwood, with the tensile sides splitting. In the case of a heartwood, the specimens separated without significant deformation.

In the case of LT90 (Fig. 14) a relatively abrupt linear section occurred, but at the same time the visible failure did not occur in the form of a fracture, as can be seen in the diagram.

In contrast, the LT90 heartwood specimens showed a non-significant but more easily distinguishable loss of integrity on the curve (Fig. 15).

The typical fracture pattern of the LT90 specimens (Fig. 16) can be compared with the literature described for the LR90 specimens. In a

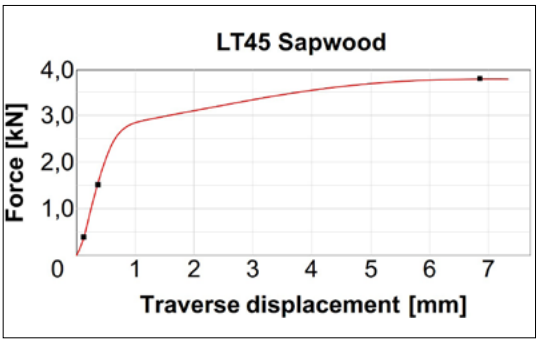

Fig. 11. *Force-displacement diagram – LT45 sapwood.*

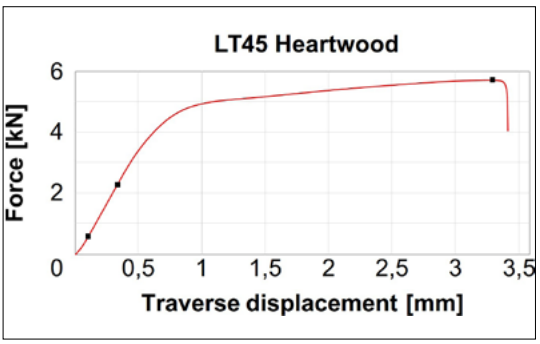

Fig. 12. *Force-displacement diagram–LT45 heartwood.*

Fig. 13. *Typical fracture pattern of the test specimens – LT45.*

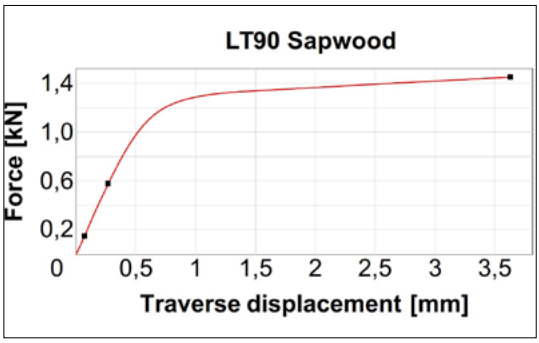

Fig. 14. *Eorce-displacement diagram – LT90 sapwood.*

Fig. 15. *Force-displacement diagram – LT90 heartwood.*

Fig. 16. *Typical fracture pattern of the test specimens – LT90.*

tangential direction, it is characterised by the protrusion of the annual rings, both in the case of the sapwood and the heartwood. Both specimen types suffered permanent deformation, which was more significant in the case of heartwood.

The RT45 sapwood specimens (Fig. 17) showed a slight decrease in the failure rate after the point of maximum force application, with no sudden fracture pattern.

The heartwood curve followed a similar pattern (Fig. 18), but in the last stage a decreasing as-case indicating a gradual destruction appeared. The small jumps indicated the breakage of the tree rings.

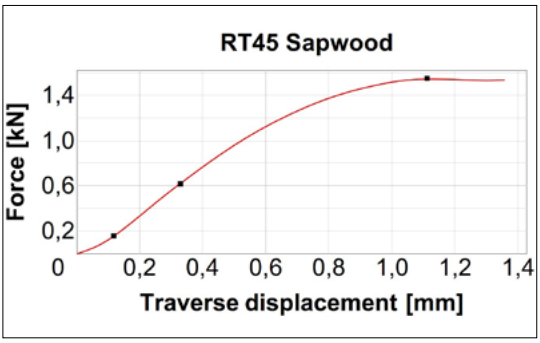

Fig. 17. *Force-displacement diagram – RT45 sapwood.*

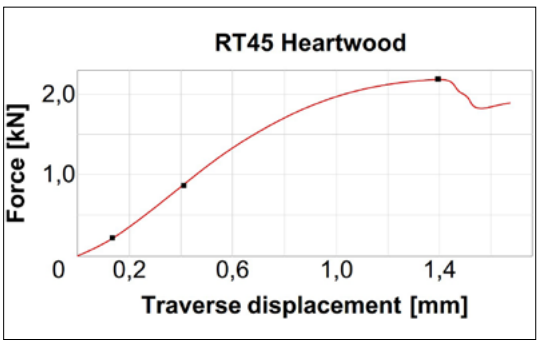

Fig. 18. *Force-displacement diagram – RT45 heartwood.*

Fig. 19. *Typical fracture pattern of the test specimens – RT45.*

A typical failure pattern in the tangential and radial directions is the buckling of the annual rings (Fig. 19). The fracture pattern in the sapwood was almost all annual rings, in the heartwood the whole specimen showed permanent buckling.

The slope of the linear section of the diagrams is determined by the elastic modulus in the linear elastic range, which can be determined from the formulas presented earlier. The following figures show the values of the elastic modulus in each direction, separately for the sapwood and the heartwood, as a function of the width of each specimen. The exact average values are presented in tabular form.

For the LR0 specimens (Fig. 20) all parts showed similar elasticity values, the heartwood having a minimally higher average, but also a higher dispersion than the sapwood, due to the more brittle behaviour.

The LR45 specimens showed much larger differences (Fig. 21). While the sapwood fitted tightly to a value, the heartwood showed not only a large variance, but also much larger results, not only on average but also considering its minimum values.

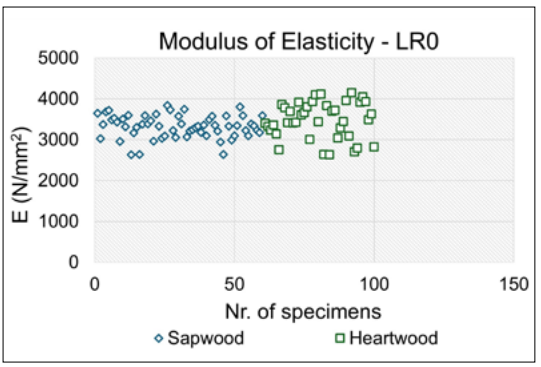

Fig. 20. *Modulus of elasticity values - LR0.*

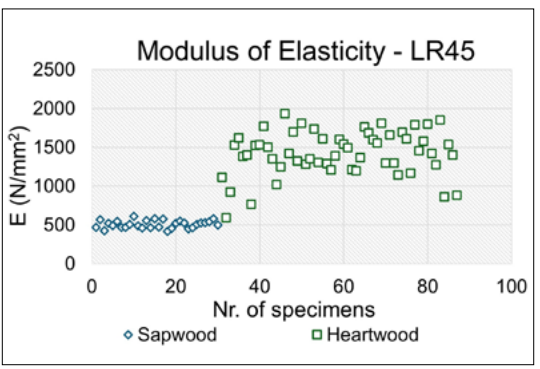

Fig. 21. *Modulus of elasticity values – LR45.*

The elastic modulus values of the LR90 specimens also show a difference between the sapwood and the heartwood (Fig. 22). This variance is significant in all cases but is also easily distinguishable relative to each other. The heartwood gave a higher average value.

The results for the LT45 specimens (Fig. 23) were distinct in terms of elastic modulus values, however, the average of the heartwood was only slightly higher than the average of the sapwood. The scatter of the heartwood was larger, with minimum values below the minimum of the sapwood. Compared to the LR45 specimens, the sapwood showed a higher scatter, but the difference between the two logs was less.

LIn the LT90 direction, the dispersion of the sapwood and heartwood values was almost equal, with the average of the sapwood values below the average of the heartwood values (Fig. 24).

The elastic modulus values of the RT45 specimens were also divided into mixed groups of sapwood and heartwood (Fig. 25). The experiment included specimens that included the sapwood - heartwood boundary along the entire length and hence the properties of both parts were characterized. The variation was large for each group, with the averages being larger for heartwood. The mixed samples represented a kind of average between the two parts.

Based on the results presented, the following tables show the averages, minimum, maximum, standard deviation, and percentage of standard deviation values for compressive strength, elastic modulus, the lower the smaller the value, the more dependable the material behaviour. The fc.k refers to the quantiles in the lower 5%, which are used to determine the strength class. The comparison is based on the strength values of the Eurocode5 series of standards, also used in structural design, which also consider the lower 5% quantile of the characteristic value [7]. 45° specimens are not covered by the standard and cannot be classified (N.C.). LR0 is for the pressure parallel to the fibre, LR90 and LT90 are for the pressure perpendicular to the fibre.

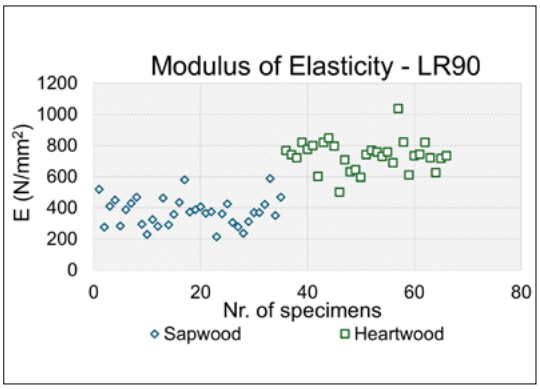

Fig. 22. *Modulus of elasticity values – LR90.*

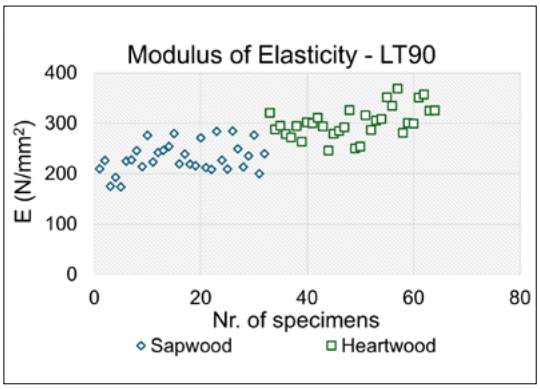

Fig. 24. *Modulus of elasticity values – LT90.*

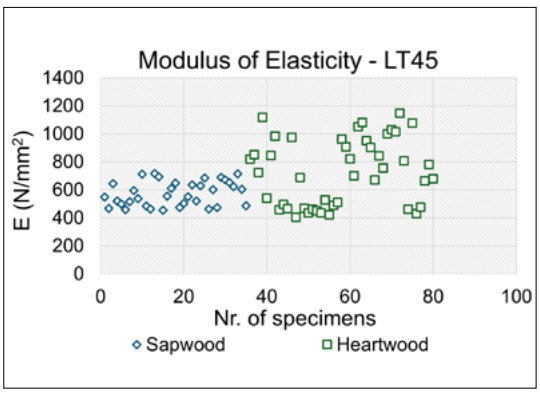

Fig. 23. *Modulus of elasticity values – LT45.*

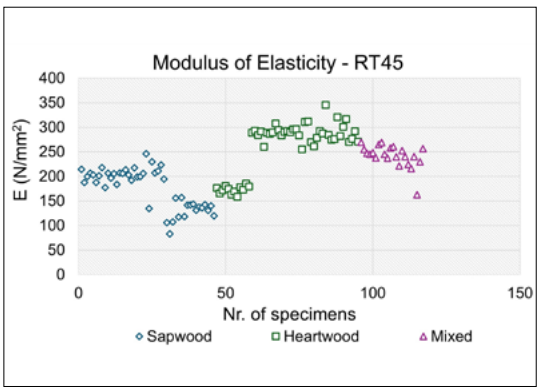

Fig. 25. *Modulus of elasticity values – RT45.*

Table1. *LR0 – pressure parallel to the fibre*

LR0 – pressure parallel to the fibre (N/mm²)			
Sapwood		Heartwood	
Average	33.72	Average	33.02
Min.	24.71	Min.	21.48
Max.	38.18	Max.	41.01
Std. dev.	2.85	Std. dev.	5.17
Std. d. %	8.46	Std. d. %	15.66
Sapwood and heartwood together			
σ_{12}	33.44	$f_{c.k}$	24.93
E_{mean}	3384	Szil. o.	C30

Table 2. *LR45 – 45° pressure to the fibre*

LR45 – 45° pressure to the fibre (N/mm²)			
Sapwood		Heartwood	
Average	7.26	Average	11.48
Min.	5.69	Min.	5.04
Max.	8.62	Max.	16.44
Std. dev.	0.64	Std. dev.	2.69
Std. d. %	8.88	Std. d. %	23.45
Sapwood and heartwood together			
σ_{12}	10.02	$f_{c.k}$	5.74
E_{mean}	1108.5	Szil. o.	N. B.

Table 3. *LR90 – pressure perpendicular to the fibre*

LR90 – pressure perpendicular to the fibre (N/mm²)			
Sapwood		Heartwood	
Average	3.74	Average	5.93
Min.	2.87	Min.	4.48
Max.	4.53	Max.	8.83
Std. dev.	0.50	Std. dev.	0.91
Std. d. %	13.44	Std. d. %	15.32
Sapwood and heartwood together			
σ_{12}	4.77	$f_{c.k}$	3.79
E_{mean}	543.6	Szil. o.	C50

Table 4. *LT45 – 45° pressure to the fibre*

LT45 – 45° pressure to the fibre (N/mm²)			
Sapwood		Heartwood	
Average	8.28	Average	9.19
Min.	6.88	Min.	6.02
Max.	9.43	Max.	14.09
Std. dev.	0.80	Std. dev.	2.80
Std. d. %	9.70	Std. d. %	30.42
Sapwood and heartwood together			
σ_{12}	8.79	$f_{c.k}$	6.50
E_{mean}	661.1	Szil. o.	N. B.

Table 5. *LT90 – pressure perpendicular to the fibre*

LT90 – pressure perpendicular to the fibre (N/mm²)			
Sapwood		Heartwood	
Average	2.62	Average	3.81
Min.	1.78	Min.	2.91
Max.	3.32	Max.	4.69
Std. dev.	0.40	Std. dev.	0.42
Std. d. %	15.20	Std. d. %	10.96
Sapwood and heartwood together			
σ_{12}	3.22	$f_{c.k}$	2.49
E_{mean}	266.7	Szil. o.	C22

Table 6. *RT45 – 45° pressure to the fibre*

RT45 – 45° pressure to the fibre (N/mm²)			
Sapwood		Heartwood	
Average	2.46	Average	3.34
Min.	1.82	Min.	0.77
Max.	3.05	Max.	4.49
Std. dev.	0.41	Std. dev.	0.81
Std. d. %	16.86	Std. d. %	24.18
Mixed		Sz + g + v	
Average	3.27	σ_{12}	2.98
Min.	2.96	E_{mean}	223.6
Max.	3.70	$f_{c.k}$	2.51
Std. dev.	0.21	Szil. o.	N. B.
Std. d. %	6.48		

4. Conclusions

From the above measurement results, it can be concluded that the wood showed significantly different behaviour between the diverse types of wood. This can be seen from the diagrams drawn during the tests, which also indicate the behaviour and the type of deterioration. Significant differences between the sapwood and the heartwood sections were observed during the measurements. The sapwood grid showed more spring-like behaviour, the fibres slid and deformed, but the specimen remained in one piece. When the heartwood was destroyed, much more brittle fracture patterns were observed, mostly with specimens separating, fibres tearing and breaking. The Modulus of elasticity values also showed significantly different behaviour as a function of the sapwood and the heartwood, with scatter values as shown in the tables. The elastic modulus and strength values were also determined for both logs together, considering their working together. To determine the strength values that can be measured in practice, the lower 5% quantiles were calculated and then classified into a strength class. The results showed that the sapwood, despite its lower strength results, showed a more reliable and elastic behaviour with low variance. On the other hand, the heartwood had higher measuring values, but its brittle behaviour gave more unpredictable results with higher scatter.

Based on the results, it can be concluded that the strength of grey poplar reaches the strength requirements of structural timber and can be recommended as a structural material, thus replacing imported pine.

References

[1] Gálos B., Führer E.: *A klíma erdészeti célú előrevetítése.* Erdészettudományi Közlemények, 8/1. (2018) 43–55. https://www.doi.org/10.17164/EK.2018.003

[2] Molnár S., Farkas P.: *Nyár (nyár fajok) – Populus spp*. In: *Földünk ipari fái* (2nd ed.), Eds. Molnár S., Farkas P., Börcsök Z., Zoltán Gy., Photog. Richter H.G., & Szeles P., Faipari Tudományos Egyesület, Sopron, ISBN 978-963-12-5239-2, 97–99.

[3] Askenazi E. K.: *Anizotropia dreveszinü i drevesznüh materialov (A fa- és faalapú anyagok anizotrópiája)*. 1. kiadás. Lesznaja Promüslennoszty, Moszkva, 1978. 97-99.

[4] Szalai J.: *A faanyag és faalapú anyagok anizotróp rugalmasság- és szilárdságtana.* 1. rész. A mechanikai tulajdonságok anizotrópiája. Erdészeti és Faipari Egyetem, Sopron, 1994. 286–293.

[5] EN ISO 13061-17: Physical and Mechanical Properties of Wood – Test Methods for Small Clear Wood Specimens-. Part 17: Determination of Ultimate Stress in Compression Parallel to Grain. 2017.

[6] Bodig J.: *The Effect of Anatomy on the Initial Stress-Strain Relationship.* Forest Products Journal, 15/5. May 1965. 197-202.

[7] Armuth M., Bodnár M.: Fa tartószerkezetek – Tervezés az Eurocode alapján. 3. aktualizált és bővített kiadás. Artifex Kiadó Kft., Budapest, 2018. 19.

Acta Materialia Transylvanica 8/2. (2025) 105–112.
DOI: Hungarian: https://doi.org/10.33923/amt-2025-02-10
English: https://doi.org/10.33924/amt-2025-02-10

Simulation Analysis of Internal Stresses in Implant Screws

Ádám VÖRÖS,[1] Csanád PESKE,[2] Klaudia TALABÉRNÉ KULCSÁR [3]

[1] *Széchenyi István University, Audi Hungaria Faculty of Automotive Engineering, Department of Materials Science and Machine Design, Győr, Hungary, voros.adam@hotmail.com*

[2] *Óbuda University Alba Regia Faculty, Institute of Engineering. Székesfehérvár, Hungary, peskecsanad@gmail.com*

[3] *Óbuda University Alba Regia Faculty, Institute of Engineering. Székesfehérvár, Hungary, kulcsar.klaudia@amk.uni-obuda.hu*

Abstract

The aim of this study was to investigate the failure of titanium alloy fixation screws (connecting the implant and the abutment) used in custom-made subperiosteal implants. Once the cause of failure was determined, our main objective was to determine the maximum tightening torque for the existing design. To achieve this, 3D CAD screw models were examined using finite element software. Based on the results obtained, we were able to recommend a tightening torque interval to the screw manufacturer that was guaranteed not to lead to failure (provided that the screws are manufactured according to the dimensional tolerances specified in the drawing). Our secondary objective was to improve the design of the screw to ensure that the failure could be fully eliminated. In this paper we will describe the failure mode, its cause, the methodology of our investigation, the results obtained, the conclusions drawn and finally, future research opportunities.

Keywords: *subperiosteal implant, screw joint, simulation, finite element analysis.*

1. Introduction

Finite Element Method is a state-of-the-art numerical method, which is widely used in the simulation and analysis of physical phenomena. This method enables the optimization of components for more efficient and cost-effective product development [1]. In the field of medicine, especially in dentistry, numerical analysis has become an indispensable tool for the study of complex biomechanical systems that are difficult or impossible to analyse in vivo or in vitro [2, 3].

In the design and evaluation of dental implants, numerical analysis allows a detailed assessment of the stability and reliability of the interface between the implant and the surrounding bone. Overloading or underloading can have a significant impact on bone loss, which highlights the importance of accurately modelling the biomechanical behaviour of implant [5]. The application of the method also includes the analysis of dynamic and fatigue loads, which are key to predicting the long-term success of implants [3, 4].

Biomechanical optimisation plays a key role in the design of dental implants. Finite element method allows us to evaluate the effects of different implant designs and to fine-tune design parameters for long-term stability [1, 2]. In addition, finite element method allows to consider the effect of friction on screw preload, which is a critical factor for the durability of prosthetic structures [4, 6].

Overall, numerical modelling enables a comprehensive understanding of the complex biomechanical behaviour of dental implants. It contributes to improved clinical outcomes and reduced prosthetic complications [7, 8].

2. The need for analysis

2.1. Subperiosteal implants

Modern dental implants used today can be divided into three main types. The most used type is endosteal implants, which are usually screw threaded implants that are placed directly into the jawbone. If the bone volume does not allow

the use of screw implants, transosteal implants (implants that are placed through and fixed to the jawbone) or subperiosteal implants (implants that are placed over and fixed to the mandible or maxilla) may be used. The main components of subperiosteal implants are shown in Fig. 1. [9, 10].

The framework base is usually created with additive manufacturing from Ti-6Al-4V powder. After manufacturing, the piece is post-processed on a 5-axis milling machine to form the threads and the surfaces that would incorporate the interfaces (sleeves). The interfaces (which will later receive the crown or denture superstructure) and the fixation screws are usually made of Ti-6Al-4V ELI based titanium alloy, machined (turning) from bar stock.

In this study, we investigated the screws used to fix the implant framework to the interface in subperiosteal implants. Fig. 2. shows a technical drawing of an implant screw with its main dimensions and tolerances.

2.2. Problem statement

As can be seen in Fig. 2. the screws used have M1.8 threads. To tighten these and similar sized screws, dentists usually use a tightening torque of 255 Ncm.

To tighten the screw, the internal keyhole slot with a 1.3 mm flat width is used. To maintain the torque interval, a calibrated torque wrench is used. A bit head provides the connection between the screwdriver and the screw. To ensure that the screws can be tightened with as high torque as possible without damaging the internal keyhole or bit head, the size of the keyhole opening must be maximised. The size of the screw head is limited due to space constraints, and the total length protruding from the upper plane of the receiving (nut) thread must not be greater than Ø2,4 × 2,2 mm as shown in the drawing.

For this reason, the design and dimensions of the internal keyway must be carefully selected to avoid leaving too small a wall thickness between the outer surface of the screw head or the undercut required by the thread runout and the internal keyway or its pilot hole. The surfaces connected by these potential fracture lines are illustrated in four different cross-sections for improved clarity and are marked in pairs using different colors, as well as with the labels a, b, and c in Fig. 3. If not properly selected, the stresses arising in the screw head may exceed the yield strength of the screw material (795 N/mm²), causing shear fail-

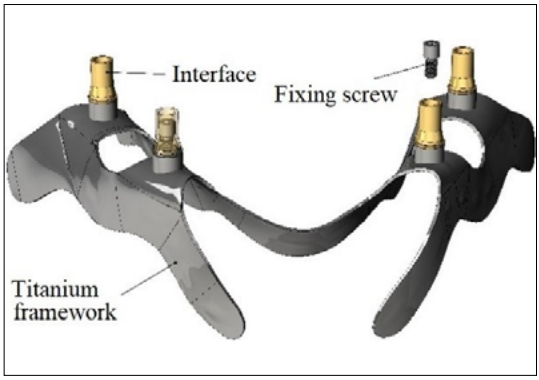

Fig. 1. *Main components of subperiosteal implants.*

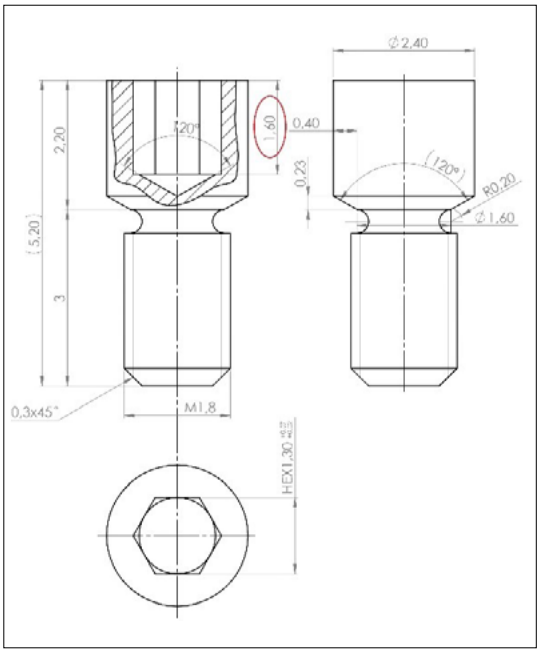

Fig. 2. *Technical drawing of interface fixing screw with its main dimensions.*

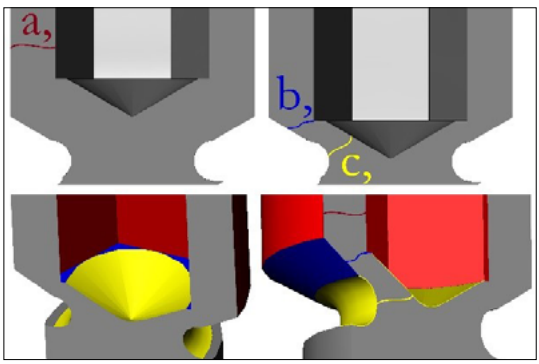

Fig. 3. *Critical cross-sections.*

ure between the screw head and the shank (screw head breaking off). [9].

Based on the location of the narrowest cross-section, three different critical cross-sections can be distinguished, the locations of which are shown in Fig. 3.

In case a, the fracture occurs between one tip of the hexagon and the side of the screw head. In this case, this is not relevant, as the size of the key is carefully selected and repeatedly checked. Moreover, it cannot be modified. In case b, the fracture occurs between the tapered part of the screw head and the gap. In case c, the fracture occurs between the tip of the technological (pilot) hole of the internal keyhole and the undercut required by the thread run-out.

The latter two are due to the choice of a keyhole opening that is too deep. Fig. 4. shows a screw after failure. In this case, the fracture occurred in cross-section c.

The reason for our research is that during the assembly of a sample prepared for load testing, some screws sheared at as little as 30 Ncm.

In this preliminary study, we examined a total of four different screws, all of which were individually machined on a lathe. Failure occurred at 30 Ncm, 32.6 Ncm, 33 Ncm, and 55 Ncm, respectively. Since the result at 55 Ncm differs by ~20 Ncm from the other torque values, we suspect a one-off manufacturing defect in the other screws.

Fig. 5. shows the torque wrench used in the mentioned study, specifically the Stahlwille Torsiotronic 1.2 model.

It is important to note, however, that due to the multiple testing prior to clinical use and the strict quality management systems in place, no production defective screw can be supplied to the end-user. At the same time, the aim is to ensure that screws that could fail under such load in the future are not produced in the first place.

Basically, for the internal keyway of the screws, the pilot hole can have 3 different vertex angles. These angles are defined by that of the selected pilot drills. Out of these three versions, we have considered the two most common cases of 180° and 120° pilot drills, but there are also 140° drills available. The vertex angles of the pilot drills and their corresponding hole patterns (in ascending order from left to right according to the size of the tip angle) can be observed in Fig. 6.

3. CAD model description

In this paper, a simulation study of the internal stresses within implant screws was performed. The model is shown in Fig. 7.

Fig. 4. *Ccrew after failure, two broken-off screw heads and one threaded shaft.*

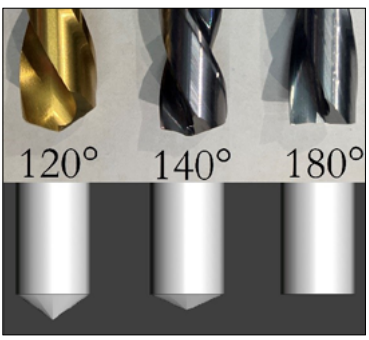

Fig.6. *Vertex angle options for pilot drills and their respective pilot hole geometries.*

Fig. 5. *Utilized torque wrench*

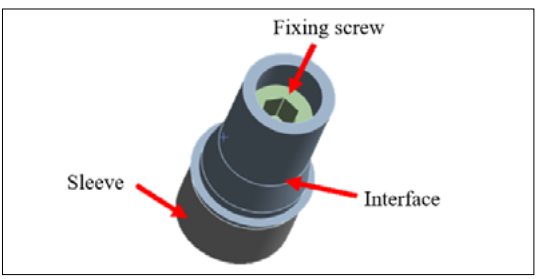

Fig. 7. *The CAD modell.*

The model was made up of 3 parts: the sleeve material was Ti-6Al-4V (Grade 5), which was manufactured using additive manufacturing together with the subperiosteal implant. The model also included the interface and the screw, which were both made of Ti-6Al-4V ELI (Grade 23) titanium alloy. The screw and the sleeve did not contain threads, they were created by post-geometric transformation in the simulation software. Ansys (engineering simulation software) considers all contact surfaces as „bonded" after importing them. It means that no displacement is allowed between the components. The bonds between the parts had to be manually adjusted: the connection between the sleeve and the interface remained „bonded", the connection between the sleeve and the screw was „frictional", and the connection between the interface and the screw was selected to be „rough", which allows the elements to separate. As the sleeve and the implant are created together, fixed connection was considered between them. The implant osseointegrates and can therefore move together with the jaw. The load was defined as the screw tightening torque, with values between 10 Ncm and 80 Ncm. The selected boundary conditions are shown in **Fig. 8** .

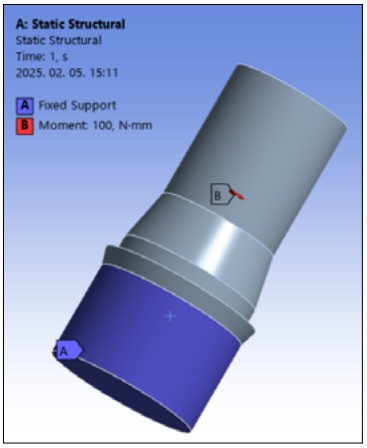

Fig. 8. *CAD-model and boundary conditions.*

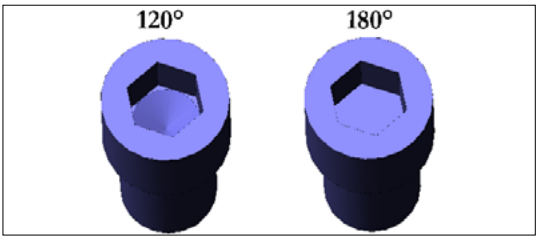

Fig. 9. *Designs of different vertex angles.*

4. Analyses

Our tests were carried out on two types of fixing screws: one with a 120-degree and one with a 180-degree tip angle. These are shown in **Fig. 9**.

Tetrahedral meshing technique was selected. In the case of the 120° vertex angle, the number of nodes ranged from 51 260 to 53 194. The element numbers were between 33 289 – 34 776. For the 180° vertex angle, these values were as follows: the number of nodes ranged from 51 447 – 52 566 and the element numbers ranged from 33 455 – 34 325. Denser meshing was applied for the study area.

5. Results of numerical analyses

In this paper, the stresses arising in the screw at the thread runout groove and at the thread were analysed. Based on the results, it can be stated that the maximum stress values are generated at the thread runout, as shown in **Fig. 10.**

The location of the maximum stress in the shaft of the fixing screw is shown in **Fig. 11.**

Fig. 12 shows the stress distribution, where the maximum stress at the above-mentioned location is very clearly visible.

Fig. 13 shows the measured stress distribution

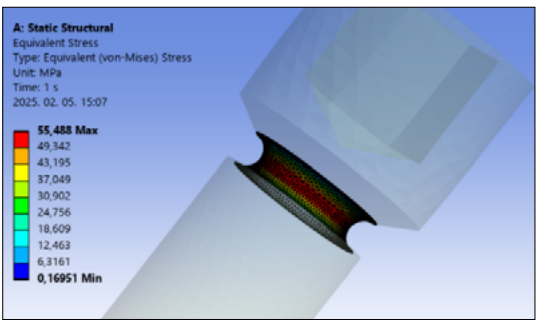

Fig. 10. *Occurring stress at the neck of the screw.*

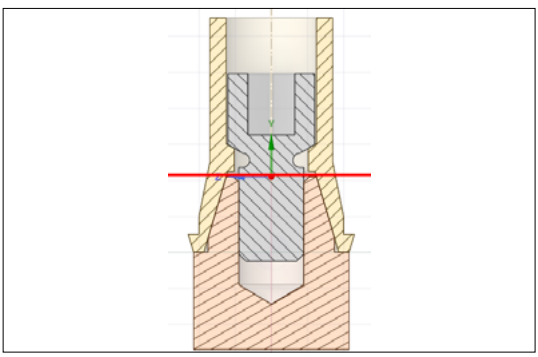

Fig. 11. *Location of the maximum stress within the shaft of the screw.*

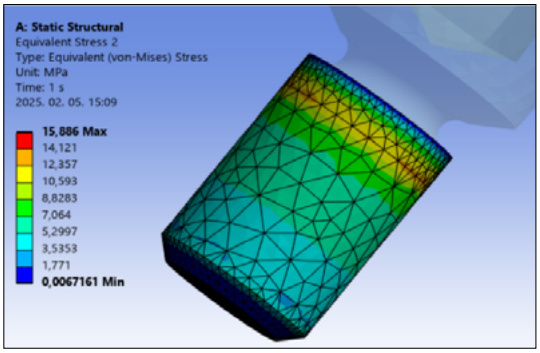

Fig. 12. *Stress distribution in the screw shaft.*

at the screw neck for the fixing screw with 120° vertex angle. In the following diagrams, the horizontal axis of the diagrams shows the different screw tightening torques and the vertical axis shows the maximum stress values in the screw. Each different coloured value (function) corresponds to a different keyhole depth (red dimension in **Fig. 2**).

Fig. 14. shows the stress distribution in the screw shank, measured for a fixing screw with a 120° tip angle.

Fig. 15. shows the measured stress distribution at the screw neck for the fixing screw with 180° vertex angle.

Fig. 16. shows the stress distribution in the screw shank, measured for the fixing screw with a 180° tip angle.

5. Conclusion

As already mentioned in the first chapter, the yield strength of the Ti-6Al-4V ELI material used for the screws is 795 N/mm², based on the manufacturer's catalogue datasheet and the ASTM F136-13 standard, considering the material diameter applied in this study. This means that if the internal stresses arising in the screw reach this value, plastic deformation of the screw will begin. In engineering practice, factors of safety are applied during the design process to reliably prevent such failure.

The chemical composition of the raw material is presented in **Table 1**, while its main mechanical properties are summarized in **Table 2**. These values are taken from the ASTM F136-13 standard, which applies to medical-grade, low-impurity titanium alloys, specifically the wrought and annealed Ti-6Al-4V ELI (Grade 23) titanium alloy. This standard ensures that the material meets the stringent requirements imposed by medical applications **[10]**.

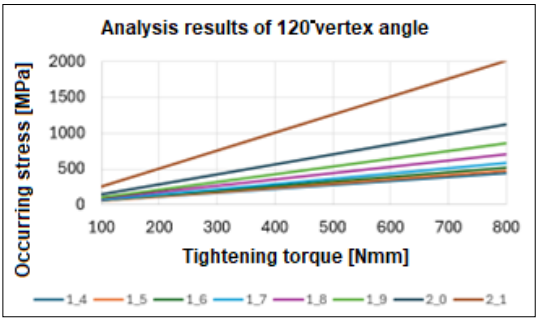

Fig. 13. *Analysis results of 120° vertex angle (at the screw neck).*

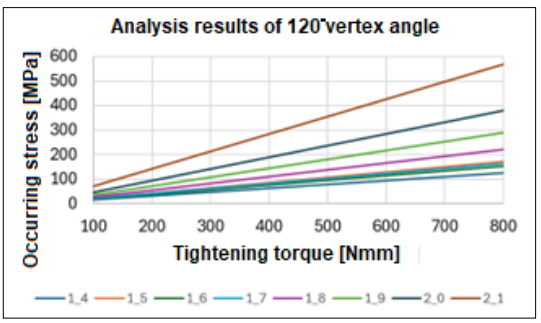

Fig. 14. *Analysis results of 120° vertex angle (within the screw shaft).*

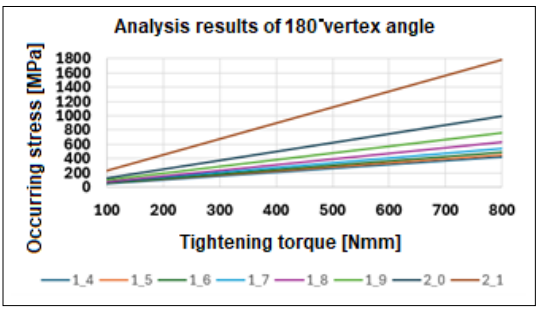

Fig. 15. *Analysis results of 180° vertex angle (at the screw neck).*

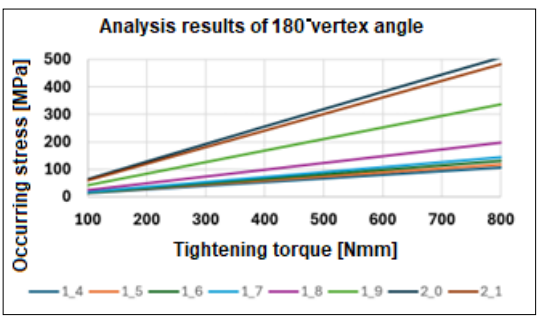

Fig. 16. *Analysis results of 180° vertex angle (within the screw shaft).*

Table 1. *Chemical composition of Ti-6AL-4V-ELI alloy*

Ti-6AL-4V-ELI (ASTM F136) mass %	
Al	5.5–6.5
V	3.5–4.5
Fe	max 0.25
O	max 0.13
C	max 0.08
Ti	rest

Table 2. *Mechanical properties of Ti-6AL-4V-ELI alloy*

Ti-6Al-4V-ELI | (ASTM F136) Mechanical properties	
Density	4.47 g/cm^3
Melting point	1649 °C
Beta transition temperature	977 ± 4 °C
Thermal conductivity (at 20°C)	6.6 W/m°C
Yield strength (at 20°C)	min 795 N/mm^2
Tensile strength (at 20°C)	min 860 N/mm^2
Elongation (at 20°C)	10%

Table 3. *Maximum stress values in the screw in the case of a 120° pilot hole*

Results are shown in N/mm^2 ($\sigma_{120°}$)						
Drill hole length (mm)	Tightening torque (Ncm)					
	25	30	40	50	65	80
1.4	137	165	220	275	357	440
1.5	148	177	236	295	384	472
1.6	163	196	261	326	424	522
1.7	183	220	294	367	477	587
1.8	220	264	352	440	572	704
1.9	269	323	430	538	699	861
2	352	423	564	705	916	1128
2.1	631	757	1009	1261	1639	2018

Table 4. *Maximum stress values in the screw in the case of a 180° pilot hole*

Results are shown in N/mm^2 ($\sigma_{180°}$)						
Drill hole length (mm)	Tightening torque (Ncm)					
	25	30	40	50	65	80
1.4	133	159	212	265	345	424
1.5	141	169	225	282	366	451
1.6	152	182	243	304	395	486
1.7	169	202	270	337	438	540
1.8	198	237	316	396	514	633
1.9	239	287	382	478	621	765
2	310	372	497	621	807	993
2.1	558	670	893	1117	1452	1787

Low impurity content is of paramount importance to achieve good biocompatibility.

When evaluating the results, three different cases and three safety factors are shown. In the first case the factor of safety n = 1. Thus, the maximum allowable internal stress is 795 N/mm^2. Values exceeding this are shown in **Table 3** and **4** on a red background. In the second case the factor of safety is n = 1.5. Thus, the maximum allowable internal stress is 530 N/mm^2 (values exceeding this are shown on an orange background). In the last case, the factor of safety is n = 2,5, in which case the maximum allowed stress value is 318 N/mm^2 (values exceeding this value are marked with a yellow background). In cases where the tables do not show any other colour (white background) for the stress value obtained, there is certainly no failure (calculated with a factor of safety of n = 2,5).

Table 3 shows the maximum stress values for the 120° and **Table 4** for the 180° holes as a function of the inner-wrench-hole depths (**Fig. 1**, size in red) and tightening torques (25-80 Ncm).

The upper limit of the tightening torque range of 25±5 Ncm for screws is 30 Ncm. Based on the simulation results obtained, different maximum pilot hole depth could be determined depending on whether the pilot hole for the internal keyway had a 120° or 180° vertex angle. Based on the maximum stresses, the maximum hole length for the 120° case was 1.8 mm and for the 180° case was 1.9 mm. Both cases considered a safety factor of n = 2.5.

Based on our results and experience, we recommend the use of 180° vertex angle pilot drills in the future, as simulation results show that in this case, by an average of 8.44% lower stress values can be expected. This, in turn, allows longer internal keyhole openings to be produced. The big advantage of a deeper keyhole opening is that a higher tightening torque can be safely achieved when tightening the screws without damaging either the key or the screw.

Table 5. *Percent differences of maximum internal stresses within the screw*

Pilot hole length	Maximum torque difference (Dif)
1.4 mm	3.42%
1.5 mm	4.46%
1.6 mm	6.87%
1.7 mm	8.11%
1.8 mm	10.08%
1.9 mm	11.17%
2 mm	11.93%
2.1 mm	11.45%

Table 5 shows the percentage difference in internal stresses for given hole lengths for the 120° and 180° vertex angle holes. It can be observed that the magnitude of the differenced shows a continuous increase with increasing hole depths. For holes with a depth of 1.9 mm, the deviation is as high as 11.17%.

Formula (1) was used to calculate the values in the table.

$$Dif = 1 - (\sigma_{180°}/\sigma_{120°}) \quad (1)$$

6. Future research opportunities

Avoiding screw breakage when tightening screws during surgery is of paramount importance. If screw failure is clearly detected during surgery (head break-off), the screw must be removed and a new screw must be inserted. Removal of the screw(s) may mean increased surgery time, which may increase anaesthetic complications and thus lead to consequential additional costs. An even more significant problem is when deformation or failure of the screw is not detected and there is no clear external sign of it. This can be the case, for example, when the internal head stresses due to tightening reach the yield point, causing the head of the screw to twist relative to the shank, but no full fracture occurs because the stresses do not reach the tensile strength of the material. In this case, the quality of the connection is inadequate due to damaged screws, which can lead to early implant failure.

For these reasons, we would like to continue our research in the following directions:

- investigation of the stress concentration effects of different thread runout geometries,
- production of physical screws and testing of their failure modes. This would validate our simulation results,
- design and testing of new screw designs (optimisation of head height, internal hole length, head diameter, investigation of the possibility of using self-locking tapered designs to eliminate possible loosening),
- examination of screw materials and their post-processing (heat treatments),
- determination of the optimum tightening torque range for M1.8 and M2 bolts, using both simulation and physical tests.

Acknowledgement

We would like to thank Dent-Art Ltd. for the test pieces (interfaces, screws) provided, and the company's employees, especially Dr. János Kónya, the company's manager, for the consultation opportunities and professional assistance. Their experience and help greatly accelerated the progress of our research.

In addition, special thanks to Abricad Ltd. for temporarily providing us with access to their SolidWorks design software. This allowed us to create 3D models of the screw and the interface.

Additionally, we would like to thank the Ministry of Culture and Innovation and the National Research, Development and Innovation Fund for their support under the University Research Fellowship Program (EKÖP-KDP), which has been awarded to Ádám Vörös. This was a great help both during the research and during the writing of the article.

References

[1] Stein E.: *History of the Finite Element Method – Mathematics Meets Mechanics – Part I: Engineering Developments.* In: The History of Theoretical, Material and Computational Mechanics – Mathematics Meets Mechanics and Engineering. (Editor: Stein E.). Springer Berlin, Heidelberg, 2013. 399–442.

[2] Dolgov V. Y., Klyshnikov K. Y., Ovcharenko E. A., Glushkova T. V., Batranin A. V., Agienko A. S., et al.: *Finite Element Analysis-Based Approach for Prediction of Aneurysm-Prone Arterial Segments*. Journal of Medical and Biological Engineering, 39/1. (2019) 102–108. https://doi.org/10.1007/s40846-018-0422-x

[3] Gizzi A., De Bellis M. L., Vasta M., Pandolfi A.: *Diffusion-Based Degeneration of the Collagen Reinforcement in the Pathologic Human Cornea.* Journal of Engineering Mathematics, 127/3. (2021) 1–27. https://doi.org/10.1007/s10665-020-10088-x

[4] Heller M. O.: *Finite Element Analysis in Orthopedic Biomechanics.* In: Human Orthopaedic Biomechanics. (Innocenti B. and Galbusera F.) Academic Press, Southampton, 2022. 637–658.

[5] Geng J., Tan K. B. C., Liu G.: *Application of Finite Element Analysis in Implant Dentistry: a Review of*

the Literature. The Journal of Prosthetic Dentistry, 85/6. (2001) 585–598. https://doi.org/10.1067/mpr.2001.115251

[6] Alkan I., Sertgöz A., Ekici B.: *Influence of Occlusal Forces on Stress Distribution in Preloaded Dental Implant Screws*. The Journal of Prosthet Dentistry, 91/4. (2004) 319–325. https://doi.org/10.1016/j.prosdent.2004.01.016

[7] Assenza B., Scarano A., Leghissa G., Carusi G., Thams U., Roman F.S., Piattelli A.: *Screw- Vs Cement-Implant-Retained Restorations: an Experimental Study in the Beagle. Part 1. Screw and Abutment Loosening*. Journal of Oral Implantology, 31/5. (2005) 242–246. https://doi.org/10.1563/1548-1336(2005)31[242:SVCRAE]2.0.CO;2

[8] Pjetursson B. E., Thoma D., Jung R., Zwahlen M., Zembic A.: *A Systematic Review of the Survival and Complication Rates of Implant-Supported Fixed Dental Prostheses (FDPs) After a Mean Observation Period of at Least 5 Years*. Clinical Oral Implants Research, 23/6. (2012) 22–38. https://doi.org/10.1111/j.1600-0501.2012.02546.x

[9] Jaber H., Kónya J., Kulcsár K., Kovács T.: *Effects of Annealing and Solution Treatments on the Microstructure and Mechanical Properties of Ti6Al4V Manufactured by Selective Laser Melting*. Materials, 15/5. (2022) https://doi.org/10.3390/ma15051978

[10] ASTM F136: Titanium Alloys. Standard Specification for Wrought Titanium-6Aluminum-4Vanadium ELI (Extra Low Interstitial) Alloy for Surgical Implant